Università degli Studi di Genova

Department of Earth, Environment and Life Sciences - DISTAV

Water-Loaded Depth and Terrestrial Heat Flow of the Eastern Mediterranean Sea

Doctoral Thesis by

ELIE EL JBEILY

Doctoral Research in Science and Technology

for Environment and Territory

Curriculum: ***Earth Science***

XXXIV Cycle

Supervisor: ***Prof. Massimo Verdoya*** (University of Genova, DISTAV)

Co-supervisors: ***Dr. Paolo Chiozzi*** (University of Genova, DISTAV)
Prof. Roberta Ivaldi (Istituto Idrografico della Marina, IIM)

Acknowledgements

Several people participated directly and indirectly in the achievement of this PhD thesis. Firstly, I would like to mention that it was not possible to carry out this study without the assistance and continuous support of my supervisors to whom I express my sincere gratitude. They gave me the great opportunity to reach a higher academic level of studies. Prof. Massimo Verdoya (UniGe) for his brilliant contribution in this work and immense knowledge in the geothermal field. Dr. Paolo Chiozzi (UniGe) for his trust, significant advice and interesting ideas. Prof. Roberta Ivaldi (Italian Hydrographic Institute) for her incomparable motivation and enthusiasm even before starting the research project. They are thanked for making this project possible and for accepting me as a part of their team over the last three years.

Secondly, I am feeling so lucky and honoured to have conducted my PhD course at the University of Genoa acknowledged for the guidance through the whole process.

I am indebted to the Lebanese Navy Hydrographic Service for all the great opportunities that had offered me during the first year of the PhD especially to Dr. Afif Ghaith for his valuable input and indications.

The Lebanese Council of National Research (CNRS-L) and the Lebanese Petroleum Administration (LPA) are thanked for providing scientific data and information.

Dr. Lama Inati and Dr. Angelo Camerlenghi are thanked for their constructive critical comments that led to the significant improvement of the work.

Last but not least infinite thanks and gratefulness are to my family, my wife Alice Apigalli who sustained and encouraged the realization of this project, my parents and parent in-law and especially to my best brother Georges El Jbeily for his continuous support, care and encouragement.

At last, all thanks are to my Lord for reasons too numerous to be mentioned.

Summary

I investigated the nature of the lithosphere of the Mediterranean Sea from the Ionian to the Levantine basins. My approach relies on a geophysical methodology that combines the analysis of terrestrial heat flow information with data of bathymetry, sediment and crustal thickness derived from both global models and high-resolution local measurements. Correction for sedimentation and climatic changes were applied to infer the purely conductive steady-state geothermal flow. Bathymetric data were processed by removing subsidence caused by sediment deposition to obtain the water-loaded seafloor depth (WLD) also known as total tectonic subsidence. To remove the sediment-load effect, I used porosity and density data corrected for the rebound effect and available from offshore drillings. For deeper, highly compacted sediment layers, density was obtained by converting seismic velocities. For each of the main sedimentary basins, a bulk-density variation curve as a function of depth was determined. Subsequently, sediment correction curves were generated and used to infer the water-loaded depth of each basin. An additional crustal correction was applied to the basins of likely oceanic nature. The resulting thermal data and water-loaded seafloor depths were then compared to reference models of continental stretching and ocean plate cooling to investigate the nature of the lithosphere and to understand seabed features that do not simply derive from cooling but can account for mantle dynamics. Such an approach is applicable where large wavelength free-air gravity anomalies occur, i.e., differently from zones of subduction, flexural moats and seamounts deriving from local tectonic events unrelated to lithosphere stretching and cooling. The results argue that the Levantine Basin is floored by a continental crust that stretched by a factor of 2.5. This basin could have reached thermal equilibrium, and thus the surface heat flow does not show any enhancement caused by extension. WLD of 6 km in the Ionian Basin and 7.2 km in the Herodotus Basin support an old lithosphere of oceanic type. By adopting as reference the plate cooling model, the residual bathymetry, i.e., the difference between the bathymetry predicted by the model and the estimated WLD, is negative, namely -0.4 km in the Ionian Basin and -1.6 km in the Herodotus Basin. However, the observed heat flow does not match that predicted by the plate model. The half-space cooling model seems in better agreement with the heat flow data but fails in predicting WLD and the corresponding residual bathymetry is positive. The residual bathymetry estimated with the plate model is consistent with free-air gravity data and could be evidence of the presence of a colder and thick lithosphere in the Ionian and Herodotus basins sinking in the asthenosphere. This is consistent with the low heat flow observed in the whole Eastern Mediterranean Sea.

Riassunto

In questa ricerca ho studiato la natura della litosfera del Mediterraneo orientale tra i bacini Ionico e Levantino. L'approccio che ho utilizzato è basato su una metodologia geofisica che combina l'analisi del flusso termico terrestre con dati batimetrici, di spessore crostale e sedimentario, derivanti da modelli globali e misurazioni locali ad alta risoluzione. Una correzione per gli effetti dovuti ai cambiamenti climatici e alla sedimentazione è stata applicata per dedurre il flusso geotermico stazionario e puramente conduttivo. I dati batimetrici sono stati elaborati rimuovendo la subsidenza causata dalla deposizione dei sedimenti per ottenere la profondità del fondale per il solo effetto di carico dell'acqua (WLD) anche detta subsidenza tettonica totale. Per rimuovere l'effetto del carico sedimentario, ho impiegato dati di porosità e di densità provenienti da perforazioni marine e corretti per l'effetto "rebound". Per gli strati sedimentari posti più in profondità, la densità dei sedimenti è stata ottenuta tramite la conversione delle velocità sismiche. Per ognuno dei principali bacini sedimentari è stata determinata la curva di variazione della densità apparente in funzione della profondità. Successivamente sono state prodotte le curve di correzione sedimentaria ed usate per trovare la WLD caratteristica di ogni bacino. Un'ulteriore correzione crostale è stata applicata ai bacini di probabile natura oceanica. I dati termici e la WLD sono stati comparati a modelli di riferimento di stiramento continentale e di raffreddamento di placca oceanica con l'obiettivo di analizzare la natura della litosfera e di capire le caratteristiche del fondale marino che non sono semplicemente derivanti dal raffreddamento e subsidenza della litosfera, ma da processi dinamici del mantello. Tale approccio è applicabile in aree dove le anomalie di gravità di aria libera sono di grande lunghezza, cioè diversamente dalle zone di subduzione, di fossa causate da piegamento elastico e da montagne sottomarine derivanti da eventi tettonici locali diversi dallo stiramento e dal raffreddamento della litosfera. I risultati ottenuti indicano che il fondale del bacino Levantino è costituito da una crosta continentale che si è stirata di un fattore di 2,5. Questo bacino potrebbe aver ormai raggiunto l'equilibrio termico, e quindi il flusso di calore superficiale non mostra alcun effetto causato dall'estensione. WLD di 6 km nello Ionio e 7.2 km nell'Erodoto sono a favore di una litosfera vecchia, di tipo oceanico. Adottando come riferimento il modello di raffreddamento della placca, la batimetria residua, cioè la differenza tra la batimetria prevista dal modello e il WLD stimato, è negativa, ovvero - 0.4 km nello Ionio e - 1.6 km nell'Erodoto. Tuttavia, il flusso di calore osservato non corrisponde a quello previsto dal modello della placca. Il modello di raffreddamento di un semi-spazio sembra in migliore accordo con i dati sul flusso di calore, ma non riesce a prevedere WLD e la corrispondente batimetria residua è positiva. La batimetria residua stimata con il modello di raffreddamento della placca oceanica è coerente con i dati di gravità e potrebbe essere la prova della presenza di una litosfera più fredda e spessa nello Ionio e nel bacino di Erodoto che affonda nell'astenosfera. Ciò è coerente con il basso flusso di calore osservato in tutto il Mar Mediterraneo orientale.

Contents

List of figures

List of tables

1. INTRODUCTION

In the Eastern Mediterranean Sea, many geological events which started in the Permian, by the end of the Paleozoic era, have led to the formation of a number of sedimentary basins. It is not easy to reconstruct the evolution of this part of the Mediterranean Sea that results from complex geodynamical processes and movements of plates (Eurasian-African-Arabian) and microplates. The nature of the underlying lithosphere (continental or oceanic) of the basins cannot be well understood without a detailed study of the origin and structure of the crust.

The last five decades had witnessed an increased knowledge either of thermomechanical properties of sedimentary basins or of the isostatic response of the lithosphere to applied loads. This scientific progress was not only limited to new geodynamical theories and models (Parsons and Sclater, 1977; McKenzie, 1978; Royden, 1986) but also included high-quality geophysical data acquisition. Different local, regional and international research institutes have been continuously participating in offshore data acquisition surveys to enhance the knowledge of the Eastern Mediterranean Sea lithosphere structure and composition. The elaboration of existing data using new techniques of interpretation together with the acquisition and processing of new geophysical data are the best methods of investigation. A difficulty exists and is related to the fact that new sources of scientifically interesting data from deep boreholes and cores remain exclusively belonging to petroleum agencies.

Temperature and pressure control the deep chemical and physical processes of the Earth. Such processes, regulating large- and small-scale internal phenomena (plate movements, seismicity, volcanism, etc.), are usually attributed to its internal thermal energy. Therefore, the knowledge of thermal regime and mechanisms controlling heat transfer is fundamental to allow the understanding of geological and dynamical processes. On the other hand, the thermal structure and the terrestrial heat flow are related to tectonic history of the lithosphere.

For example, in a continental, rift-breaking event and consequent formation of an oceanic crust thermal processes of the upper mantle are involved. Some geodynamic models envisage these processes which had already started in the lithosphere when stresses deriving from the horizontal movements of lithospheric plates have induced a thinning till reaching the breaking point. Accordingly, the asthenosphere will passively rise to fill up the space created by the thinning of the lithosphere. Other models consider a rift as derived from a thermal anomaly in the asthenosphere. Being anomalously hot, mantle rocks will rise and increase in volume causing the stretching of the overlying continental lithosphere which, due to heating, becomes also mechanically weak. Finally, the weakened upper part of the lithosphere cracks along tensional faults and blocks of the crust may subside creating a series of depressions or tectonic trenches. The principal tectonic processes which contribute to the formation of an extensional sedimentary basin (thinning, crustal breakup, subsidence, volcanism, partial melting) are related to thermal anomalies. Therefore, a detailed

study of the thermal regime and subsidence story of the stretched lithosphere would provide interesting qualitative and quantitative characterization.

This PhD study relates the geothermal frame to the geological and geodynamical context of the Eastern Mediterranean Sea from the Ionian Basin, to the west, to the Levantine Basin, to the east. A major debatable question of this area is related to the geological nature and age of the various composing basins. Many studies showed opposite results and conclusions. The lack of high-resolution geophysical information and its uneven distribution is a reason for such disagreements.

The main objective of this research is to enhance the knowledge of the nature of the lithosphere underlying the main sedimentary basins by reviewing and integrating various available geophysical and geological data. It also aims to demonstrate that the Mediterranean Sea cannot be simply analysed by using global scale models of heat flow and subsidence. The lithosphere composition and nature, together with heat flow and age, have an important interest for the understanding of mantle dynamics.

Due to the inter-dependence of the parameters adopted for my analyses and models, a particular flowline was chosen. A detailed presentation of the state of the art about the geological and tectonic evolution of the area of interest (Chapter 1) was followed by sections dedicated to bathymetry and heat flow data collection and correction (Chapters 2-4). Data were selected from global and local surveys scattered in the literature.

Based on sediment physical properties and crustal composition, bulk-sediment density and sediment correction curves as a function of sediment thickness were inferred (Chapter 5). This was used to estimate the water-loaded depth of the various sedimentary basins. The latter, together with the purely conductive heat flow, constitute the main parameter to be compared to continental stretching and oceanic cooling models. In the last sections of the study (Chapters 6 and 7) the results are discussed and interpreted.

Such an approach led to identify the distribution of the different lithospere types, to estimate geological ages of the latter and to recognizing perturbations of the thermal regime associated with the principal tectonic processes. The better knowledge of the distribution of the different types of lithosphere forms a valuable basis to develop geodynamical models for the formation and evolution of the basins in the region.

2. GEOLOGICAL AND GEODYNAMICAL SETTINGS

The Mediterranean Sea is an area of complex and debatable geological and geodynamical settings. It is widely accepted that the eastern part of the Mediterranean Sea (EMS) represents the remains of the northern Neo-Tethys Ocean margin. This area is bounded by active convergent major plates and micro-plates, which complicate the tectono-geodynamic and stratigraphic history. From a geomorphological and structural point of view, the study area contains from east to west the Levantine Basin, the Eratosthenes Seamount and Hecateus Rise in the Cyprus domain, the Nile Delta Cone, the Herodotus Basin, the Mediterranean Ridge, the Sirte and Ionian Basins with their bordering European (Hellenic Arc, Apulian and Calabrian) and North African (Cyrenaica, Libyan) margins. In addition, many seamounts, troughs and mud fields occur. Offshore drilling sites for geophysical exploration were selected based on special geomorphological, dynamical and tectonic settings and their distribution is related to the previously mentioned structures and basins (Fig. 1). A geological and geodynamical framing of the area of interest is necessary to understand its history and tectonostratigraphic evolution. Several geodynamical interpretations have been so far proposed for the EMS. In this section, I will review the main tectonic and geodynamic reconstructions which can be found in literature.

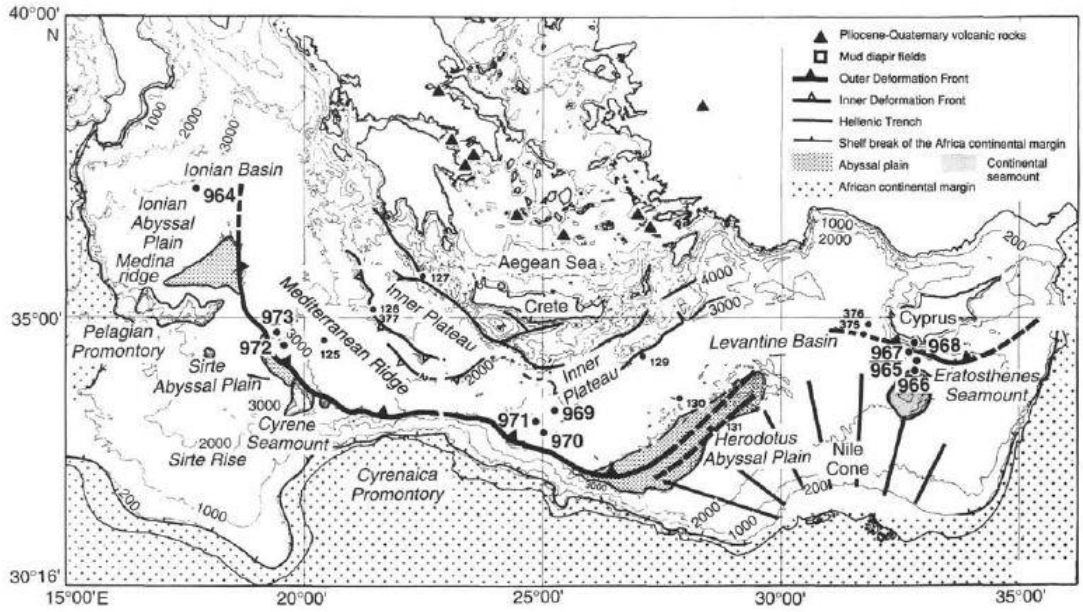

Fig. 1 Tectonic map of the Eastern Mediterranean Sea presenting the location of ODP-Leg 160 and DSDP drilling sites (after Robertson et al., 1996).

2.1 Tectonic and geodynamic hypothesis

Before the development of plate tectonics theory, the formation of the Mediterranean sedimentary basins was explained through processes of “oceanisation” with simple

rift and subsidence of the continental crust (Ritsema, 1970). With the advent of global tectonics, some authors noticed a strong analogy between the Mediterranean basins and foreland basins of the Pacific, while others tried to explain their formation through a classical mechanism of oceanic opening. The principal condition to verify the foreland basin model is the existence of a subduction plane of neogenic age. Another hypothesized mechanism for the formation of the Mediterranean basins is microplates movement. Horizontal movements within a compressive domain are huge to create spaces that will be occupied by Neogenic basins (Andrieux et al,. 1971, Auzende et al., 1973; Balannya and Garcia Duenas 1987 and 1988). In addition, peripheral thrusts can be easily explained by large translations and rotations of blocks.
After the Pangea breakup during the Permian, the Tethys Ocean was created with a N-S opening (Stampfli and Borel, 2002; Robertson et al., 2012). Continents were divided into a northern part Gondwana and a southern part Laurasia (Ricou, 1994). Following this period, in the Permian, Neo-Tethys opened when the Cimmerian block underwent ocean spreading and detached from Gondwana. Later, Tethys witnessed an evolution at its southernmost domain giving birth to "Alpine Tethys" and "Neo-Tethys" (Favre and Stampfli, 1992; Stöcklin, 1974). The Eastern Mediterranean Sea (EMS) remained a relic of the Neo-Tethys (Fig. 2) but it is not yet solved whether it is a remain of the main ocean, a secondary connected branch (Dercourt et al., 1986) or a stretched continental domain (Roure et al., 2013).
An East-West spreading in the Eastern Mediterranean occurred during the Early Triassic (Schattner and Ben-Avraham, 2007) creating the Levantine passive margin. Cooling and subsidence followed this last extension phase (Bein and Gvirtzman, 1977; Bar et al., 2013). In the Late Triassic, Gondwana carried on with a northward migration. By the end of the Jurassic, Alpine Tethys and Neo-Tethys oceans merged east of Sicily determining the northern African plate boundary (Frizon de Lamotte et al., 2011). Between the Early Triassic and Early Jurassic, continental blocks (such as Eratosthenes Seamount) detached from the Afro-Arabian continent together with seafloor spreading in the Herodotus and Cyprus Basins (Robertson, 2007; Gardosh et al., 2010). The convergence between Afro-Arabia and Eurasia caused the Tethys closure during the Late Cretaceous period and was accompanied by the beginning of collision in northern Arabia during the Late Eocene (Agard et al., 2007) with uplifting and tilting of the eastern Levantine Basin margin (Walley, 2001). The separation between Arabia and Africa along the Levantine Fracture System was enhanced by the collision of the Indian Plate with the Eurasian Plate creating left-lateral movements between Eurasia and Africa and block faulting in the Red Sea (Hempton, 1987). Rifting in the Red Sea was furtherly initiated especially after that the Afar Mantle Plume reached the surface (Zeyen et al., 1997; George et al., 1998; Segev and Rybakov, 2010).

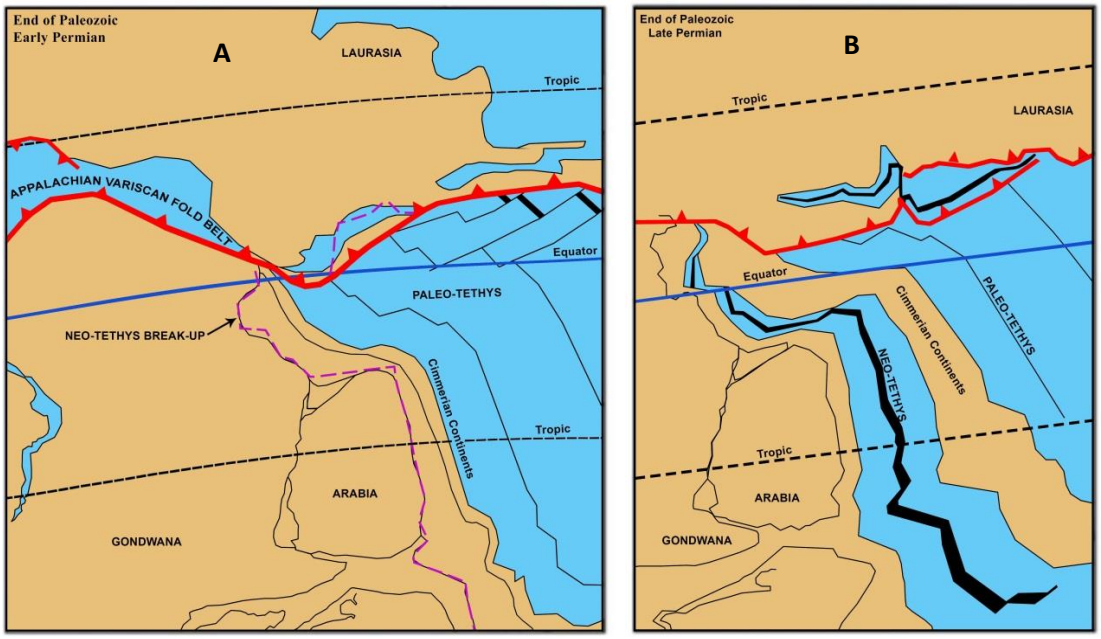

Fig. 2 A- Pangea Breakup: Laurasia-Gondwana separation and Tethys formation. B- Neo-Tethys formation + Cimmerian continent separation from Gondwana. N-S opening of the EMS (after Stampfli et al., 2001).

2.1.1 Levantine and Herodotus basins

The easternmost part of the EMS is delimited to the north by Cyprus Island which is uplifted on the southern border of the Eurasian Plate and the southern margin of the Anatolian plate, to the east by the Levantine margin and the Arabian plate, and to the south by the Nile Delta deep-sea fan (Fig. 1). Eratosthenes seamount separates the Levantine Basin from the Herodotus Basin and the Eastern Mediterranean Ridge. In this part of the EMS, three major plates interact (African, Eurasian and Arabian) with different tectonic processes such as rifting, convergence, passive margin and ophiolite formations (Fig. 3).

The Paleozoic-Carboniferous period noted the Palmyride depositional trough development. Permian, Triassic and Early Jurassic rifting pulses participated in shaping Gondwana passive margin and consequently the Levantine Basin of the Afro-Arabia plate (Freund et al., 1975; Robertson and Dixon, 1984). The Levantine Basin passive margin was particularly influenced by the Palmyra Basin tectonism consisting in a rifting phase followed by a passive margin and finally a convergence phase (Gardosh et al., 2008). Proterozoic accretion of island arcs and microplates against Africa formed the southern Arabian Plate (Beydoun, 1991).

A second extensional phase of rifting along the northern African margin occurred between the Permian and Early Mesozoic (Stampfli et al., 2001) after which two other extensional phases occurred in the Middle Mesozoic (Gardosh et al., 2008). These extensions participated directly in the development of the Palmyra Trough and seafloor spreading in the Eastern Mediterranean (Dercourt et al., 2000). Different studies state that the different rifting phases in the eastern part of the EMS evolved into a seafloor spreading and that the crust below the Levantine Basin is oceanic.

Others sustain that Neo-Tethys rifting did not reach spreading and that the area regards only a stretched continental crust. The Levantine Basin structure shows signs of compressional and extensional events. NS faulting running semi-parallel to the Dead Sea Transform can be found along its eastern Lebanese margin (Aksu et al., 2005; Roberts et al., 2007). Contemporaneously with the Levantine Basin formation, the Herodotus oceanic crust was created to the west after the Neo-Tethys opening (Grafunkel, 1998; Stampfli et al., 1991). Segev et al. (2018) suggested that the Levantine Basin is a back-arc basin that formed during the Cretaceous following events of volcanism, uplift, stretching and break-up of the Levantine landmass Troodos and Syrian ophiolites are pieces of evidence of seafloor spreading (Dewey et al., 1973; Papadimitriou, 2017). Stretching was compensated by subduction of the Herodotus Basin eastward under the Eratosthenes Seamount causing drift of the Seamount. This compressional regime limited the extension of the Levantine and avoided reaching lithosphere breaking and the creation of a spreading centre.

The Palmyra Basin rift stopped by the end of the Early Triassic, but the Eastern Mediterranean spreading continued. After that rifting ceased during the Middle Jurassic, a cooling and subsidence phase started (Gardosh et al., 2010; Hawie et al., 2013; Montadert et al., 2014) with a development of a sort of platform roughly parallel to the actual Afro-Arabian coastline (Tassy et al., 2015a) and the creation of a shelf and slope system along the Levantine margins (Garfunkel, 2004; Gardosh et al., 2010). The southern Tethyan margins (Levantine and Egyptian) are characterised by rift and transform fault structures and marked by platforms of carbonate-siliciclastic composition while deeper water was characterized by dolomite and limestone facies variations with additional carbonate content. More than 1000 m of synrift Permian-Triassic siliciclastic sediments were deposited in the Eastern Mediterranean and Palmyra Basins (Beydoun, 1981). During the Levantine passive margin development additional 1600 m of Triassic-Jurassic sediments were deposited along the actual coastline.

During the Upper Triassic, the Gondwana continent carried on with a northward movement. A transgression was observed on a global scale (Dercourt et al., 1993). Then a regression started in the middle Jurassic causing erosional events from the late Jurassic till Early Cretaceous. During the Early Cretaceous Dercourt et al., (1993) described Gondwana as divided into Afro-Arabia, South America, India and Australia. The Levantine region found itself in between the equator and Tropics. Since the Late Cretaceous period (Cenomanian age) Afro-Arabia began drifting northward and is continuing this motion. Many transgression events occurred during those periods and resulted in covering the northern Arabian platform with hundreds of meters of shallow-marine sands, clays and chalky pelagic carbonates (Le Nindre et al., 1990; Dubertret, 1955). Tectonically, during this Late Cretaceous (Cenomanian), the African and Eurasian plates started their convergence (Garfunkel, 2004; Robertson et al., 2007; Le Pichon et al., 2019). This tectonism gave birth to the Syrian Arc Fold Belt (Hensen, 1951; Freund et al., 1975; Garfunkel, 1998; Nader, 2014) and folds generation in the Levantine Basin (Guiraud and Bosworth, 1997). A sea-level rise of ~ 250m was recorded (Haq, 2014) accompanied by the drowning of the

Tethyan margins carbonate platforms from Santonian to early Maastrichtian and the deposition of chalk and chalky limestones (Hawie et al., 2013; Papadimitriou, 2017). In the Late Campanian Neo-Tethys started its closure after an abrupt increase of velocity of Africa relatively to Europe.

The collision between Indian-Arabian and Eurasian plates initiated in the middle to Late Eocene and witnessed geological events such as the deformation of the Syrian Arc. The Late Eocene (Fig. 3) was characterized by the separation of Arabian and African plates together with the initiation of the Dead Sea Transform Fault (DSTF) and the decrease of Afro-Eurasian collision (El-Motaal and Kusky, 2003). The DSTF is connected to the Levantine Fracture System (LFS) and has been established in two phases from the Early to Late Miocene (Brew et al., 2001; Kempler and Garfunkel, 1994).

Afro-Arabia proceeded with northward drifting in the Early Oligocene until the collision along the Zagros (Neo-Tethys Asian margin) in the Early Miocene causing a major uplift of Arabia-Africa (Bar, 2009). During the Oligocene, Red Sea Basin rifting initiated in the southern Gulf of Suez (Stanton, 2017). By the Late Oligocene, Levantine passive margins were reactivated due to the breakoff of Africa-Arabia (Gvirtzman et al., 2008). Such reactivation was evidenced through a faulted basement across the continental margin with a tilted-block structure not extending above Jurassic strata (Garfunkel, 1998). Reverse faults reaching Cretaceous and Early tertiary strata were found by Gardosh et al (2010). Arabian and African plates became completely separated in the Late Miocene through seafloor spreading in the Red Sea (Steckler and Brink, 1986).

During the Miocene, the subduction of the African plate under Eurasia south of Cyprus and the Dead Sea Transform progressed (Freund et al., 1970; Garfunkel, 1998). The Nile drainage system completed its formation in the Early to Middle Miocene. Late Miocene witnessed the Messinian Salinity Crisis in the Levantine basin and the ceasing of Gulf of Suez rifting together with the Dead Sea Transform establishment. Following this marine regression, a transgression during the Early Pliocene built up the Nile Cone. Pliocene fault activities created salt diapirs and Pliocene clastic ponds in between (Stanton, 2017). During the Quaternary, Cyprus island uplifted and the Eratosthenes Seamount subsided due to the continuous movement of African and Eurasian plates (Robertson, 1998). The compressional deformation of the Quaternary sequence especially in the Herodotus Basin is a clear sign of this subduction extending westerly towards the Florence Rise (Zitter et al., 2000; Montadert et al., 2014).

The Global Navigation Satellites System (GNSS) indicate that a circular counterclockwise rotation (20 to 35 mm/year) occurs in the EMS between Arabia, Eurasia and the Anatolian micro-plate (Fig. 3) with a general trend towards the Hellenic trench (McClusky et al., 2000; Reilinger et al., 2006; Le Pichon and Kreemer, 2010; Inati, 2017). The Eastern Mediterranean Sea is a slowly converging landlocked oceanic basin (Le Pichon, 1982) that has been sinking under the Hellenic and Cyprus subduction zones (Chamot-Rooke et al., 2005).

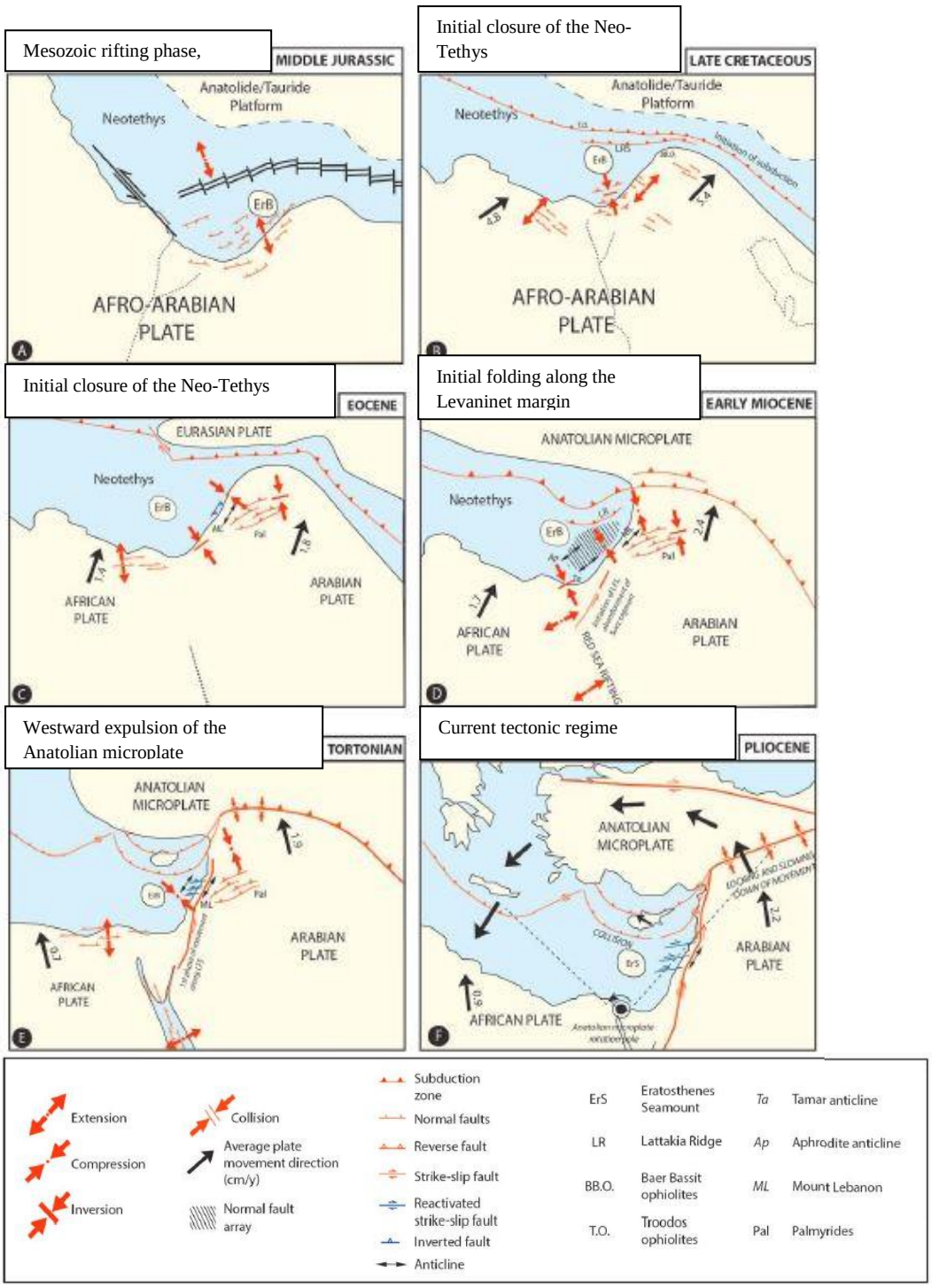

Fig. 3 Six paleogeographic maps showing the tectonic evolution of the Levantine region, (from Ghalayini et al., 2017)

2.1.2 Cyprus Arc, Eratosthenes Seamount and Hecateus Rise

Cyprus island is delimited by Turkey (Cilicia Basin) to the North and by the Cyprus Arc to the South. The margin of southern Cyprus is positioned on the upper plate of a downgoing slab. Cyprus geologic history was influenced by various tectonic events (Fig. 4). The beginning could be related to the Late Cretaceous compressional regime between Africa and Eurasia and the subsequent obduction of Troodos and Syrian

ophiolites and the formation of the Cyprus thrust-fold belt (Robertson et al., 2009; Hawie et al., 2013). Complex tectonism followed due to the juxtaposition and collision of the Troodos Ophiolites and the Mamonia Complex; deep-sea sediments may have been deposited in this phase (Clube and Robertson, 1986; Papadimitriou, 2017). From the Late Cretaceous till the Middle Eocene deep water chalks covered a remnant oceanic floor. This period was a relatively quiet from the tectonic point of view compared to the Late Pliocene – Middle Quaternary, when Cyprus has lived a strong uplift in opposition to the subsidence in the southern area (Emeis et al., 1996). Marine sedimentations onshore Cyprus and bathymetry showing sets of ridges and ponds were the clear direct proof. One of the most important features affected by the subduction slab and the final Pliocene uplift of Cyprus is the Eratosthenes seamount. This continental crust fragment seamount (Sage and Letouzey, 1990) is subject to subsidence and breaking-up since it is in an area of collision with the Cyprus active margin between the African and Eurasian plates (Robertson et al., 1994a). It is thicker in the middle and thinner to the northeast (Makris et al., 1983; Welford et al., 2015). Some authors (Montadert et al., 2014; Papadimitriou, 2017) consider the Eratosthenes Seamount as a large carbonate platform (with an evolution like that of the Egyptian margins) that evolved over a continental fragment. Other authors (Nur and Ben-avraham, 1978; Krasheninnikov et al., 1994; Kempler, 1998) sustain the theory of an Eratosthenes Seamount which rifted from the Precambrian Afro-Arabian margin during the breaking phases between Late Triassic and Middle-Jurassic. Accelerated subduction of the African plate underneath Cyprus favoured Eratosthenes subsidence and the deepening of the seafloor towards the Cyprus arc (Robertson, 1998, Sagy, 2016). Instability and strong tectonic subsidence in the northern margin of the seamount were evidenced from sediment sequences in the Miocene and till the Pliocene-Quaternary. Seismic profiles show that Eratosthenes seamount is covered by northward-southward normal faults some of which were recently active. Those normal faults are found together with extensional stress in the upper slope and summit of Eratosthenes. Another proof of the compression which affected Eratosthenes seamount is the presence of folds (anticlines and synclines) in the Pliocene-Quaternary sequences as well as the presence of the Akrotiri High formed by crustal compression and folding in the Miocene (McCallum et al., 1993).

Subsidence results were faulting of carbonate sequences and formation of a typical topography with talus fans. On the other hand, the southern margin of Eratosthenes seamount is mainly passive, and it is relative to a carbonate buildup structure. However, a hypothesis exists considering the Eratosthenes seamount as the seaward limit of extended continental crust from the Levantine margin.

Subduction has almost ceased below the Cyprus Arc (Papazachos & Papaioannou 1999) due to the docking in the subduction zone of isolated microcontinental blocks on the northern edge of the African Plate with the Eratosthenes Seamount and the Hecataeus Rise (Robertson, 1998; Welford et al., 2015). Eratosthenes Seamount reached its final vertical position in the Pliocene (Schattner, 2010).

Hecataeus Rise is considered as a faulted structural high that has acted as a buffer between the Levantine Basin and the collision front of the Cyprus Arc (Welford et al.,

2015). Different hypotheses regarding its origin exist. It was not yet resolved whether the Hecataeus Rise is a micro-continental block (Robertson, 1998) or an extension of Cyprus floored by an ophiolitic basement (Kempler et al.,1996).

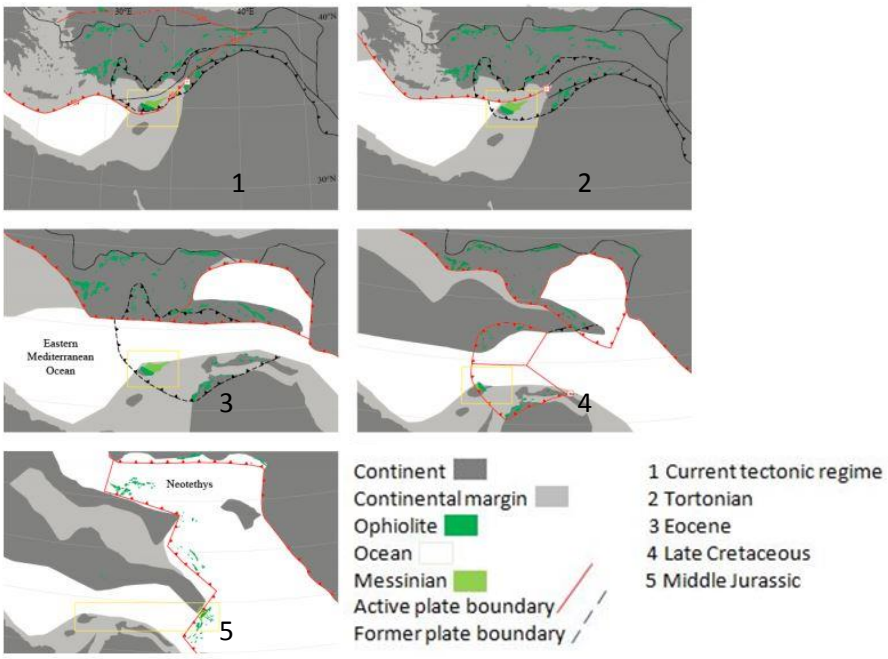

Fig. 4 Paleotectonic evolution of Cyprus Arc (yellow box) within the Eastern Mediterranean tectonic development (after McPhee et al., 2018)

2.1.3 Mediterranean Ridge

The complex structure of the Mediterranean Ridge covers a large geographic area extending from the Eastern Ionian (western Greek islands) to southern Turkey and western Cyprus. The Mediterranean Ridge was originally considered as a Miocene part of the Alpine Mountain system (Giermann, 1969). Then it was related to a plate boundary between the African and Eurasian plates. Consequently, it was assumed that the Mediterranean Ridge derives from lithospheric downwarping south of the downgoing slab (Hsü et al., 1973) and scraping of sediment off the downgoing slab (Dewey et al., 1973). Le Pichon (1982) argued that only the lower part of the sediment mass has been subducted while the upper part was detached and incorporated into an accretionary wedge. The southern side of the Mediterranean Ridge being higher than the northern side is an unusual feature of the Mediterranean Ridge explained by the accretion of thick sediments of the North African continental margin to the wedge in contrast to an earlier phase when thinner more distal sediments were incorporated into the wedge (Emeis et al., 1996). However, the simplest interpretations consider this Ridge as the subduction zone from the convergence of the Afro-Arabian and Eurasian plates (Fig. 5, Huhuen et al., 2001). Subduction continues and is still active in the eastern Ionian Basin while the geodynamical situation is more complicated in the easternmost part of the Ridge (Papadimitriou, 2017). Two interpretations for the Mediterranean Ridge nature were

invoked. The first one related the Mediterranean Ridge formation to thrust sheets resulting from crustal shortening (Finetti, 1976). The second one describes the Ridge as an accretionary prism related to the Hellenic subduction zone (Le Pichon, 1982; Cita and Camerlenghi, 1992; Hughen et al., 2006) being active up to this day below the Hellenic Arc (Papazachos & Papaioannou, 1999). To the west, it is thrust over the Ionian and to the north, the Hellenic trenches are interpreted as fore-arc basins (de Voogd et al,.1992). Towards the north African continental margin and because of the collision between this margin and the Mediterranean Ridge, the abyssal plain transforms into a narrow trough (Fig. 5). The Ridge consists of an outer domain bounded to the south by the ridge toe, an axial or ridge domain, with mud volcano and diapirs activity, bounded to the north by backthrust, and an inner ridge domain neighbouring the Hellenic trench (Mascle et al., 1999; Cita and Camerlenghi, 1992; Cita et al., 1995). The area of the Mediterranean Ridge shows complexity from a structural point of view. This Ridge has diverse morpho-structural characteristics than the rest of accretionary prisms deriving from specific geodynamic settings. For example, frontal convergence is found south of Crete while in the Ionian and Levantine domains, oblique subduction with opposite direction of shear for the free borders is found (Hughuen et al., 2006). To the west, the ridge is in contact with its backstop forming a dextral compressive flower structure and a site of mud eruption. To the East, the shearing contact exists between the Mediterranean ridge inner domain (Strabo Trench) and the Strabo Mountains.

The lower westernmost part of the deformation front of the Mediterranean Ridge accretionary complex borders with the Ionian and Sirte Abyssal Plains. Features of 1 to 8 km length and 1 to 2 km width together with elongated ridge and trough topography parallel to the deformation front are found. Those features are the products from folding and reverse faulting. The Ionian Abyssal Plain, laying beyond the active deformation front, results in much smoother slopes than the upslope of the toe of the Mediterranean Ridge or Hellenic accretionary wedge. The deformation front has an irregular bathymetry explained by the subduction of a past irregular slab.

The Nathalie (entirely beneath the seafloor) and Victor Hensen structures resulting from extensional tectonism are among the main features of this area (Hirschleber et al., 1994).

The Bannock structure was best interpreted as a sinking seamount piercing the accretionary cover resulting from the African subduction beneath Eurasia (Hieke et al., 2009). To the northeast, the rigid mass Aegean crust constitutes a “backstop” for the accretion and the limit of the deformation (Le Pichon et al., 2019).

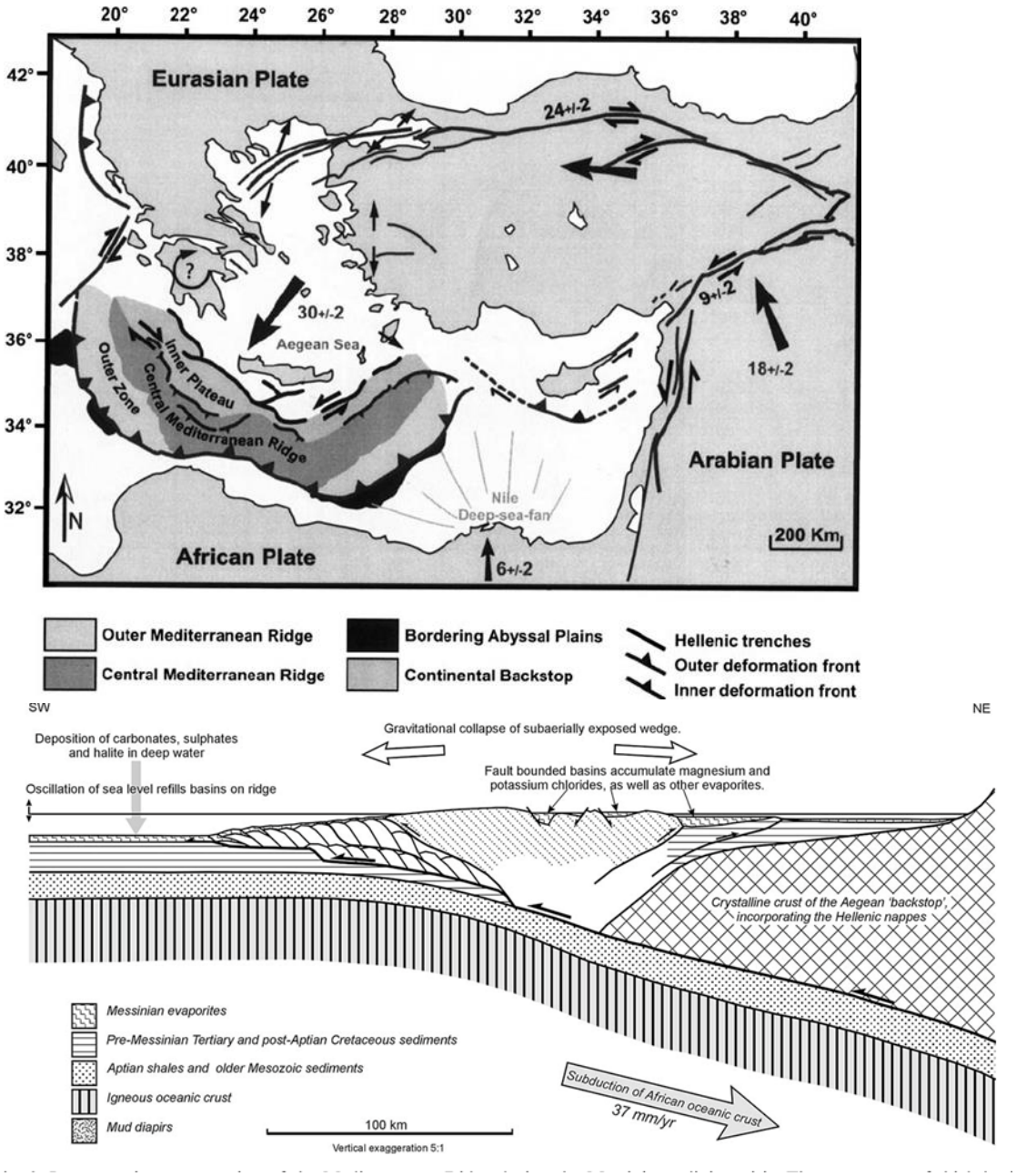

Fig. 5. The different morphostructural domains of the Mediterranean Ridge (Top) resulting from the accretionary complex due to the interaction between the Afro-Arabian and Europian micro plates (Bottom) (Huguen et al., 2006 and Westbrook and Reston, 2002).

2.1.4 Hellenic Arc

The convergence between the African and the Aegean plates take place south of Crete making the Hellenic subduction zone a highly seismic area. This island arc was uplifted after the African-Eurasian collision (Fig. 6). The Hellenic trench subject to suction force is retreating due to roll back and approaching the northern Africa passive continental margin (McKenzie, 1970; Le Pichon et al., 1995).

This subduction created in front of the Libyan Sea between the Hellenic active and African passive continental margins an accretionary wedge where sedimentary thickness reaches up to 15 km (Cita and Camerlenghi, 1992; Bohnhoff et al., 2005).

Rests of an oceanic crust were determined in the eastern and central parts of the Hellenic fore-arc zone and the eastern Libyan Sea (Bohnhoff et al., 2001; Brönner, 2003).

Bohnhoff (2005) described the Western Crete tectonic regime as an EW arc-parallel extension resulting from a normal faulting regime and the Central and Eastern Crete as an ENE sinistral transpressional fault zone. Bohnhoff (2001) considers the Ptolemaeus, Pliny and Strabo structures as deep-sea depressions with 4 km thickness wedge-shaped sedimentary basins. He neglects their classifications as subduction trenches like the ones observed at various fore-arcs zones. Crete has a heterogeneous stress field with highly scattered fault trends. The seismicity analysis indicated a uniform N-NNE relative plate motion between the Aegean and African plates along the Hellenic arc between the Ionian Sea and Rhodes (Bohnhoff et al., 2005).

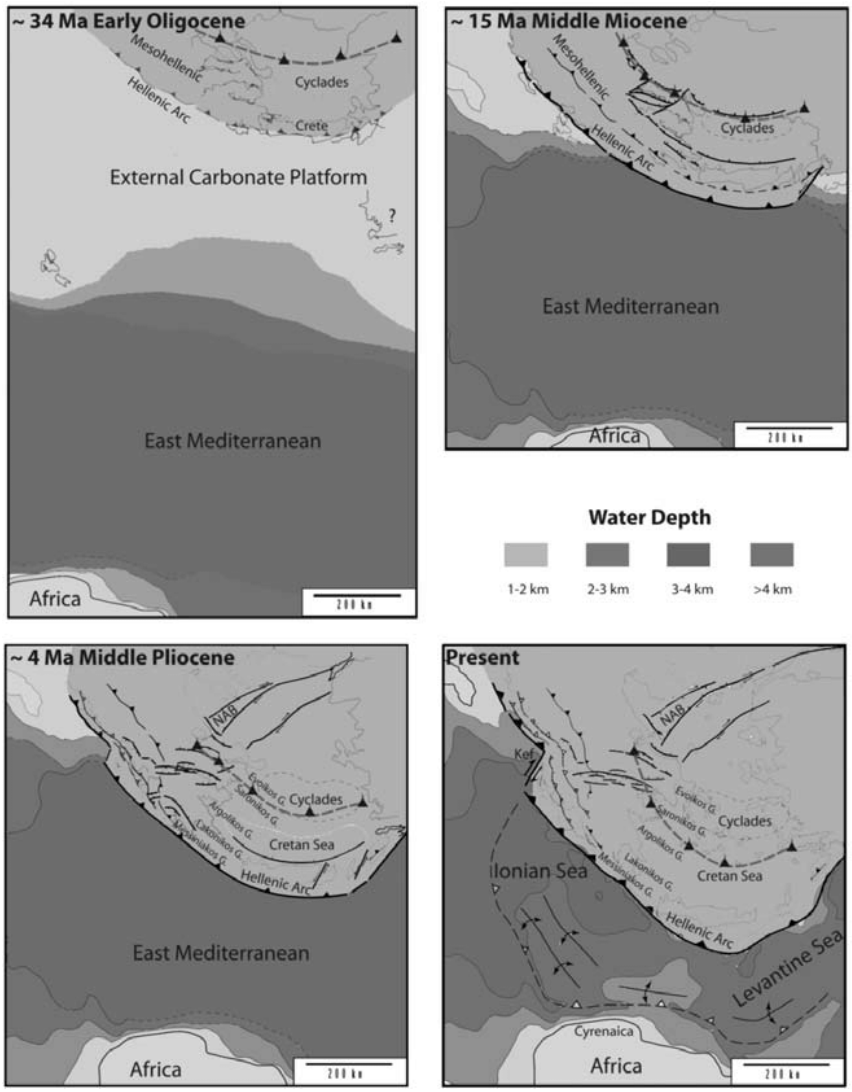

Fig. 6 Hellenic arc and trench system tectonic evolution (after Papanikolaou, 2017).

2.1.5 Mud fields

The abundance of solid (mud) and fluid (methane) sources combined with a favorable tectonic regime may result in Mud volcanism. A good example of such tectonism is the existence of active faults along the Mediterranean Ridge accretionary prism transforming it into a 500 km long mud belt site (Chamot-Rooke et al., 2005). Underwater mud domes are typical of accretionary wedge settings areas. Mud, fluid and gas will reach the surface through expulsion conduits.
To the east, near the Strabo Trench, a concentration of mud domes is found. At about 150 km south of Crete, in the northern part of the Mediterranean Ridge, the Olimpi mud dome field and mud dome-like features exist. Mud fields can be classified either as active (fluid, sediment or gas venting) or inactive and they can be set into three categories of mud diapirs, mud volcanoes and mud ridges. Those domes follow a set of phases of formation that can be compared to land volcanic domes. Among the possible hypotheses of their formation, it is generally accepted that they are firm and vertical features positioned after an upward movement or features originated by the vertical accumulation of debris flows from an existing outlet. In any case, volcanism (eruption and/or intrusion), disturbed sediments, structures collapsing (depressions from degassing) are all phenomena that participate in mud diapirs formation. The inactive Milano diapir (drilling site ODP 970) is a seabed structure of some kilometres of diameter that rises about 80 m from the seafloor.
The Napoli dome, differing from the rest of the domes by being flat-topped rather than conical, is considered as the true and active mud volcano while the rest of the structures are either mud cones or mud ridges (Camerlenghi et al., 1995).

2.1.6 Ionian Basin

Similarly to the Levantine Basin, the Ionian Basin has been observed as a landlocked basin (Le Pichon, 1982) that still have an enigmatic evolutional story and a still debatable crustal nature, whether oceanic (Finetti 1982; Rosenbaum et al., 2004; Tugend et al., 2019) or dense continental crust (Farrugia & Panza 1981). For some authors, the thin crust is oceanic in origin (Catalano et al., 2001; Gallais et al., 2011; Makris et al., 1986) especially that high-velocity gradients typical of the oceanic domain together with very low heat-flux values (30-40 mWm^{-2}) related to an early Mesozoic age (Della Vedova et al., 1989). Alternative assumptions (Hieke et al., 1998; Roure et al., 2012) mention a thinned continental crust that belongs to the distal North African continental margin. This landlocked basin is surrounded by several passive margins: Apulia to the NE, Eastern Sicily and Malta to the West and SW and Sirte and Cyrenaica to the South and SE. It is found in a key position between the European, African and Apulian plates and is essential to understand the evolution and relation between the Neo-Tethys, Alpine-Tethys and Central Atlantic oceans (Tugend et al., 2019). The age, period and direction of rifting, opening/spreading in the EMS basins are still uncertain. After the Pangea breakup (end of the Paleozoic – Early Mesozoic) the Ionian Basin was created when rifting formed the Tethys oceanic

domain (Dellong et al., 2018; Agard et al., 2011). Tugend et al., (2019) suggested the existence of a Late Triassic-Early Jurassic rifting which preceded the late Early Jurassic to Middle Jurassic formation of the basin. Other authors (Basilone et al., 2010; Raulin et al., 2011; Arsenikos et al., 2013) state similarity between rifting and palaeogeography of the Levantine-Egyptian margins and the Libyan, Tunisian and Sicilian margins which suggests a synchronous onset of opening/spreading in the Herodotus and Ionian Basins in the Middle Jurassic (Barrier et al., 2008; Frizon de Lamotte et al., 2011). However, Robertson (2007) maintains the theory of diachronous continental separation between the Herodotus and the Ionian. Regarding the opening direction, different suggestions were presented: NE-SW opening as the southern branch of the Neo- Tethys Ocean (Stampfli et al., 1991, 2001) and based on the undulating strike of the margins (Catalano et al., 2001) or NW-SE associated with the Central Atlantic opening (Barrier et al., 2008; Rangin et al., 2005). For Cernobori et al., (1996) the Ionian crust is a very thinned continental one with upper mantle rocks intrusion. On the other hand, the Ionian Basin crust is suggested to be an old Mesozoic Tethyan oceanic crust in the south becoming in the north a relic of the Apulian continental margin (Finetti, 1982, Mueller and Kahle, 1993). The transition from continental to deep water oceanic crust is clearer to the northeast than to the southwest. A low spreading rate is noticed in the basin between southeast Sicily and southwest Puglia (Catalano et al., 2001). It is assumed that the related oceanic ridge should have been flattened by thermal cooling and then buried by thick pelagic sediments of Jurassic to Tertiary age (Catalano et al., 2001; Dellong et al., 2018). Some interpretations consider the Apulian and Hyblean plateau as being originally connected. The continental rifting is assumed to have started in Late Permian-Triassic. However, the low heat flow values indicate an old 180-200 Myr oceanic lithosphere supported by a lithosphere thickness of 90 km (Calcagnile and Panza, 1981). Sicily may be considered as a remain of the Permian Tethyan Ocean or to a Permian rift with thinned continental crust, a continuation of Paleo-Tethys to the east (Catalano et al., 1991, 2001).

The magmatic anomaly of the Hyblean or Ragusa plateau may be related to magmatic intrusions which have been found along the passive continental margin of the Malta escarpment (Acocella, 2000; Henriquet et al., 2019). The age of tectonism in the Malta escarpment date back to the Triassic when dredging revealed Mesozoic-Tertiary rocks. The transition between Sicilia and the deep Ionian Basin is noted by a strong change in crustal thickness and composition and by the high bathymetric gradient. Despite the lack of data and the complex geological settings, the Ionian Sea seems to be deriving from Late Permian and Triassic continental rifting that evolved into an oceanic spreading. The Mesozoic bathymetric steps of the two conjugate passive Malta and Apulian continental margins are inherited from the Ionian Ocean rifting (Catalano et al., 2001; Dellong et al., 2018). Many subduction zones and back-arc basins were born after that the ancient Early Mesozoic Tethys lithosphere was consumed due to the convergence between Africa and Eurasia (Faccenna et al., 2001). Deep crusts have been subject to consumption in the Hellenic and Calabrian subduction zones (Caputo et al., 1970, 1972; Mele, 1998). The floor of the Ionian

Abyssal Plain is subducted eastward beneath the toe of the Mediterranean Ridge accretionary complex (subduction-accretionary tectonism) and Greece (Le Pichon & Angelier 1979; Biju-Duval et al., 1978; Le Pichon, 1982; Christova & Nikolova, 1993). The Tethys Ocean continued to the northwest and the seismicity of the Apennines slab underneath the southern Tyrrhenian Sea proofs the occurrence of a downgoing oceanic lithosphere (opening of the Ligurian-Provencal and Tyrrhenian basins). Late Cretaceous convergence between Africa and Europe was noted by inversion episodes between Santonian and Middle-Late Eocene such as those recorded on the Cyrenaica margin (Arsenikos et al., 2013).

The Calabrian prism is described as a large accretionary complex resulting from the subduction of Africa beneath Eurasia (Fig. 7). Subductions and accretionary wedges would allow considering the deep Ionian Abyssal Plain as the foreland of the Calabrian prism and the western Mediterranean Ridge to the NW and NE respectively (Gallais et al., 2011, 2012). Since the Early Oligocene (~35 Ma), the Peloritan and Calabria terranes were produced by the roll-back of the NW dipping slab of the Tethyan oceanic lithosphere which fragmented the Variscan basement blocks of the SW European margin (Bouillin, 1986; Wildi, 1983). The Ionian Basin was reached by this roll-back since the late Miocene with the opening of the Tyrrhenian back-arc basin (Stampfli and Borel, 2002; Jolivet et al., 2015). On the opposite side the front of the Hellenic Arc or Western Mediterranean Ridge is well advanced towards the deep Ionian Basin (Catalano et al., 2001). Tertiary and Quaternary shortening of the Apennines and Hellenic subduction zones did not affect the southern and southwestern margins of the Ionian Sea (Catalano et al., 2001).

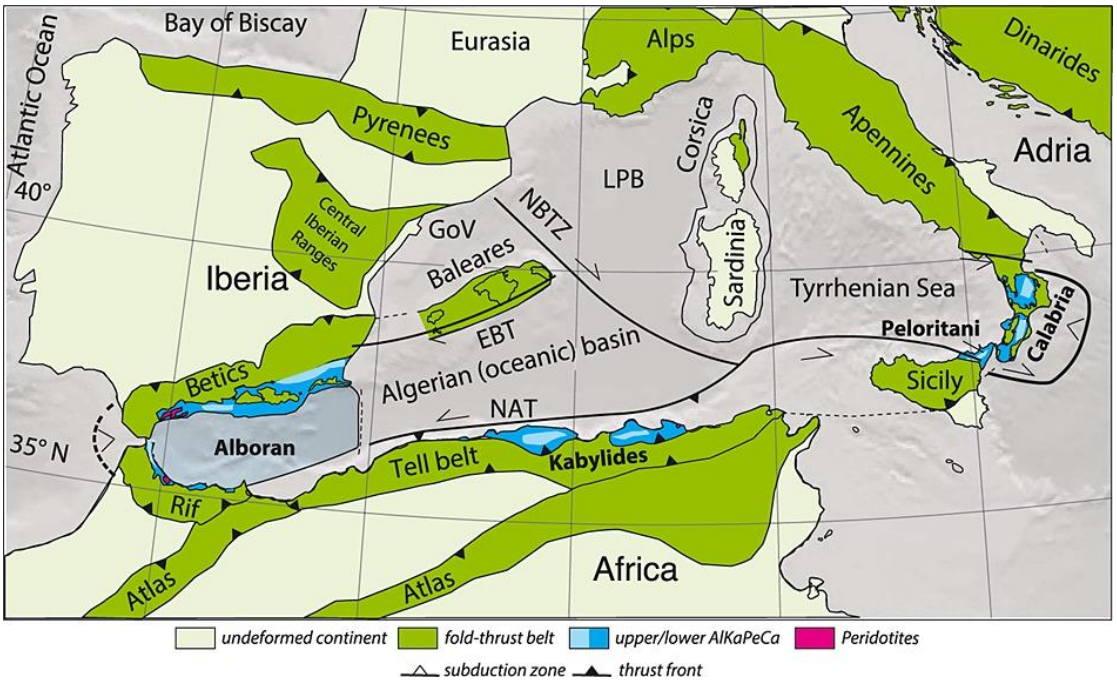

Fig. 7 The Ionian Basin evolution (after van Hinsbergen et al., 2014).

Active tectonics such as uplift and faulting (normal, reverse or strike-slip) occur at the toe of the Calabrian accretionary wedge (Hieke et al., 2006; Polonia et al., 2011) and were observed in holes of ODP 964. Such effects are typical of a compressional regime in an arc-parallel relief. Tectonic uplift followed by faulting formed the northeast-southwest sets of ridges and basins. To the south and southwest the Ionian margins are typically passive.

2.1.7 North African Margin

The African offshore margin has been continuously affected by the complex geodynamics of the neighbouring basins. Rifting during the Mesozoic led to the establishment of a series of graben, half-graben and carbonate platforms along the northern African margins. By the end of the Cretaceous (Santonian), the change in tectonism created folds and inversion of Mesozoic rift structures through the propagation of the far-field compressional regime towards the margins. This northward rifting of varying extension continued up to the Paleocene and was identified in the Sirte Basin (Stanton, 2017). During the Eocene, the Sirte Basin witnessed another rifting phase while during the Oligocene the North African margin did not mention any major tectonic events. The Late Miocene was an epoch of compression along the western African margin (Stanton, 2017). This same epoch witnessed Gibraltar closure and sea-level drop. NS compression, with consequent EW folding and reverse faulting and rifting continued till the Plio-Quaternary.
Due to the width of the area of study extending between the Ionian Basin and the Levantine Basin together with the complexity of tectonic and geologic events, I tried to summarize in Table 1 the several tectonic events following a chronological order.

Table 1 Historical sequence of tectonic and geologic events that participated in the creation of the EMS.

Era/Period/Epoch	**Main tectonic and geologic events**
Precambrian-Proterozoic	Formation of the Southern Arabian Plate.
	Accretion of island arcs and microplates against Africa.
Carboniferous	Development of the Palmyride Trough.
	Extension phase along the Northern African margin.
End of Palaeozoic	Formation of Tethys Ocean.
	Breakup of Pangea and separation of Laurasia-Gondwana.

Late Permian	Formation of Alpine Tethys and Neo Tethys.
	Separation of Cimmerian Continent from Gondwana.
	North-South opening of the EMS.
	Creation of the Ionian Basin.
	Detachment of Eratosthenes from Afro-Arabia.
Early Triassic	Formation of the West Levantine Passive Margin.
	Active Spreading in the Eastern Mediterranean.
	Cease of the rift in Palmyra.
	Seafloor spreading in Herodotus and Cyprus Basins.
Late Triassic	Northward Migration of Gondwana.
	Global Transgression and Volcanism in the Eastern Mediterranean.
	E-W opening episode of EMS.
	Rifting/Oceanic spreading of the Ionian Basin.
Early Jurassic	Last rifting phase: detachment of the Tauride and rifting of other small continental blocks.
	Numerous rifting episodes with graben and carbonate platforms affecting the North African margins.
Middle Jurassic	Start of rifting cessation in the Eastern Mediterranean with the beginning of post-rift thermal subsidence.
	Regression in EMS causing erosional events.
Late Jurassic	Determination of Northern African Plate Boundary.
	Alpine Tethys and Neo-Tethys merged east of Sicily.
	Start of erosional events.

Early Cretaceous	Gondwana division into Afro-Arabia – South America India and Australia.
	Positioning of the Levantine region in between the Equatorial and Tropical zones.
	Levantine Basin formation after the "Levant-Nubia" mantle plume volcanism and breakup of the Levantine landmass together with Herodotus floor subduction under the Eratosthenes.
	End of erosional events.
Late Cenomanian	South America breaking away from Afro-Arabia. Beginning of Afro-Arabia northward drift away from Equator and conversion towards Eurasia
	Sea-level rise (~250m) and drowning of the Tethyan margins.
Late Cretaceous	Beginning of Tethys realm (Neo-Tethys) closure.
	Troodos and Syrian Ophiolite material obduction onto Eurasia and Arabia.
	Initiation of Cyprus Arc and Latakia thrust zone.
	Convergence between Afro-Arabia and Eurasia (Transition from extensional to compressional regime).
	Inversion episodes on the Ionian margins (Cyrenaica, Sirte).
	Suspension of extension due to compression, preventing possible spreading centre formation in the Levantine.
Santonian-Campanian	Abrupt increase of velocity of Africa relatively to Europe.
	Folds and faults production after intraplate compressional deformation (till Middle Cenozoic). Formation of Syrian Arc fold belt.
Santonian-Maastrichtian	Drowning of the Eastern Tethyan carbonate platforms.
	Deposition of chalk and chalky limestone.
Early Eocene	New rifting phase in the Sirte and Pelagian basins.

Mid to Late Eocene	Continental collision between Indian-Arabian and Eurasian plates.
	Syrian Arc deformation.
	NE-SW folds development.
	Left lateral movements between Eurasia and Africa. Block faulting in the Red Sea.
Late Eocene	Onset of collision in the Northern part of Arabia and decrease of Afro-Eurasian collision.
	Initiation of Dead Sea Transform Fault (DSTF).
	Eustatic sea-level fall and marginal uplift.
Early Oligocene	Continuation of northward drift of Afro-Arabia.
	Production of Peloritan and Calabria terranes.
Mid-Oligocene	Beginning of Red Sea rifting in the southern Gulf of Suez.
	Red Sea rift shoulders uplift and Nile River initiation.
	Major sea-level fall and beginning of North African margin tectonic inversion.
	Start of separation of Arabia from Africa by seafloor spreading.
Late Oligocene	Reactivation of the Levantine passive margins due to Arabia-Africa separation.
	NNW Propagation: Gulf of Suez.
	NE Propagation: Gulf of Aqaba.
Early Miocene	Collision of the Arabian block with Neo-Tethyan Asian margin along Zagros (subduction and uplift of Arabia-Africa) + Rifting along Southern Red Sea.
	Start of Ionian Sea Deformation.
Miocene	Subduction of African Plate under Eurasia south of Cyprus.
	Development of Cyprus accretionary wedge.
	Roll-back of Hellenic Trench.
	Establishment of the Nile drainage system.

	Cessation of rifting of Gulf of Suez.
Late Miocene	Breaking of Arabia from Africa – Seafloor spreading in Red Sea + Northward drifting.
	Messinian Salinity Crisis in the Levantine (regression).
	Second Phase of DSTF.
	Roll-back of the NW dipping slab of Tethyan oceanic lithosphere reaching the Ionian Basin.
	Major period of compression along western African margin: deformation in northern Atlas, accretion and rifting in the Pelagian Basin.
Early Pliocene	Transgression and Nile Cone building-up
	SW expulsion of the Eastern Anatolian microplate.
	East Anatolian fault and Levantine Fault System (LFS) meeting NW of Syria
	Reactivation of the offshore Syrian Arc folds in the Levantine.
	Salt diapirs and Pliocene ponds offshore Nile and Levantine.
Pleistocene	Major sea-level rise.
	NS compression along the African margin with EW trending folding and reverse faulting.
Quaternary	Cyprus island uplift and Eratosthenes seamount subduction after continuous movement of Africa and Eurasia.
	Deformation reaching Florence Rise.
Present-Day	EMS continuing subduction under Hellenic and Cyprus zones.
	Eurasia and Africa slowly converging (1-2 cm/yr).
	SE movement of the SW European continental blocks.
	Counter-clockwise rotation (2-3 cm/yr) between Arabia, Eurasia and Anatolian.

3. BATHYMETRY

Oceans and seas of the world are not completely surveyed due to many limitations and difficulties which also add accuracy problems. However, global bathymetric datasets are made available through the collection of soundings derived from navigational, scientific surveys.
The Eastern Mediterranean Sea is not very well investigated from this point of view. However, it is a point of interest especially for petroleum exploration and safety of navigation. The increasing number of hydrographic surveys and offshore activities provided new data. For the EMS basin analysis carried out in this study, bathymetry is a crucial information to understand tectonics and to estimate the water-loaded depth which will be discussed in section 6. I used free public scientific data available on the world wide web. Each type of data was downloaded from specific websites as explained in the following paragraphs. In a few cases, accurate and high-resolution datasets were used to estimate errors and standard deviations of used data. Three sources of global depth data (EMODnet, NOAA-ETOPO1 and TOPEX) with different resolutions and precisions were processed, examined and compared to confirm their accuracy and correctness and to select correct depth values to be used in specific spots measurements. Then, the main morphological characteristics and variabilities of the study area are presented and briefly discussed in this section.
Bathymetry is strongly related to the history of basins formation and to geodynamical interactions between tectonic plates and microplates. It can provide quantitative information that help to understand not only the tectonics but also the crustal structure. Considering isostatic compensation, topographic or bathymetric changes are related to vertical adjustments of the lithosphere. On this regard, the density variations with depth are a fundamental piece of information. This issue will be addressed in section 5.

3.1 Global bathymetry datasets

3.1.1 EMODnet

The European Marine Observation and Data Network (EMODnet) is a 0.125x0.125 arc minutes (about 330x330 meters) Digital Terrain Model (DTM) resulting from grouping high-resolution Single and Multibeam Echo Sounders bathymetric survey datasets (SBES and MBES), composite DTMs and Satellite-Derived Bathymetry (SDB) data products. It is integrated by GEBCO (General Bathymetric Chart of the Oceans) Digital Bathymetry. EMODnet datasets can be automatically queried, and the nature of both vertical and horizontal frames can be assessed by having information concerning depth values and their corresponding geographic positions.
The bathymetric maps of the Eastern Mediterranean Sea (Fig. 8) were obtained after processing EMODnet “C4 and D4” Blocks XYZ file (the higher resolution among the

different available global datasets) in Caris Base Editor 4.2 software with a sounding selection each 10 km radius range and with Fledermaus software generating contour lines every 500 m interval. Contour lines will help in better detecting slope steepness variations in the continental margin area and the deeper parts of the abyssal plains.
To better visualize and analyze this bathymetric data, 15 to 20 times exaggerated 3D maps were created processing the available SD file of the C4 and D4 areas using Fledermaus software (Fig. 9). The 3D view was checked from different angles to enhance the detection of seabed features and the understanding of geomorphological behaviour.

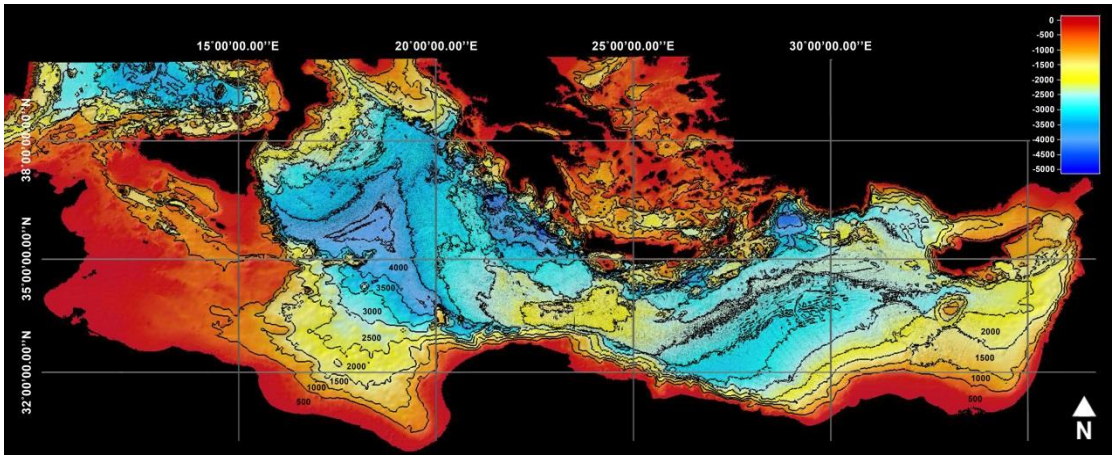

Fig. 8 Emodnet bathymetric map of the Eastern Mediterranean Sea with contour lines each 500 m interval.

The analysed area covers the Eastern Mediterranean Sea and is delimited with the following geographical coordinates (15°00' E – 36°00' E) and (030°00' N – 037°00' N). Different basins and seabed features can be distinguished from the bathymetric surfaces (Fig. 9). Due to the large extent of the area of study and for better visualization and interpretation it was convenient to divide it into a central one (15° 00' E – 24°00' E) and (030°00' N – 037°00' N) and an eastern one (24°00' E – 36°00' E) and (031°00' N – 037°00' N).

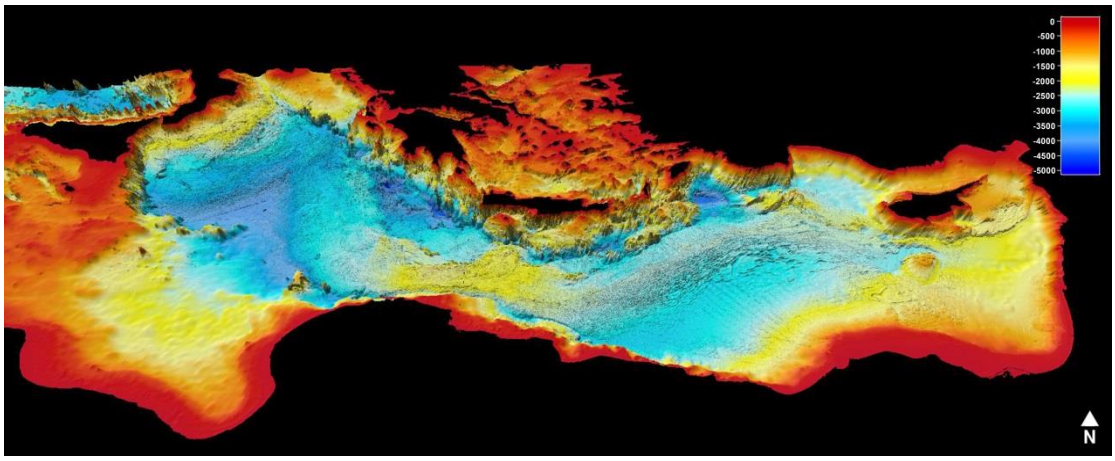

Fig. 9 Emodnet 3D bathymetric map of the Eastern Mediterranean Sea highlighting different seabed features and geological domains.

3.1.2 NOAA - ETOPO 1

The National Oceanic and Atmospheric Administration (NOAA) ETOPO 1, compared to EMODnet, is a lower resolution (1 arc minute) global digital elevation model (DEM) of the Earth topography and bathymetry.
It results from global and regional datasets of which the origin can be directly determined by controlling an interactive bathymetric map available on the link https://maps.ngdc.noaa.gov/viewers/bathymetry/.

3.1.3 TOPEX

The globally measured and estimated seafloor topography database V19.1 by Smith, & Sandwell (1997), derived from satellite altimetry and ship depth soundings (https://topex.ucsd.edu/cgi-bin/get_data.cgi), was also used to examine bathymetric data. ASCII XYZ grid (1 arc minute) of the area of interest was downloaded. In this grid, odd depths values can be considered as true soundings since they were obtained from bathymetric surveys (single beam echo sounders SBES) while even values are deduced from gravity.

3.2 Adopted bathymetry

Satellite-derived bathymetry can be biased and can lack precision. On the other hand, ship's soundings coordinates using old positioning systems are subject to meters of horizontal error. Newly high resolution and accurately positioned SBES and MBES data are not available everywhere and are limited to coastal areas or along ship tracks. Depth values, over precise geographic positions corresponding to the sediment thickness distribution grid (spot measurements) and used in this study, were selected after comparing data of the previously presented sources of bathymetry and investigating them. It was noted that depth values from the different bathymetry sources were quite similar and the difference was observed due to different adopted grids resolution. Some large differences were present over rough morphological structures.
Furthermore, high-resolution and accurately processed MBES "Simrad EM300" grid data acquired during the Shalimar 2003 marine survey were introduced into Fledermaus software. The result was a high-resolution bathymetric map of the Lebanese offshore (Fig. 10). A comparison of depth values, in 56 geographical locations, from the large Eastern Mediterranean Sea area grids (EMODNET, ETOPO 1 and TOPEX) and the Lebanese offshore surface (SHALIMAR) was made to assess the precision and accuracy level of using global bathymetry datasets. In general, this test was a piece of evidence that errors in bathymetry can reach hundreds of meters (from -928 m to 835 m) in positions where no accurate surveys are available. In this case, TOPEX data had the most plausible values of bathymetry. For the 56 selected

sites, the mean difference in bathymetry using the global dataset ranged between 29 and 94 m and the standard deviation between 75 and 102 m. For a total estimate of depth error, we proceeded with a calculation of the surface difference between the EMODnet Global bathymetry and the SHALIMAR bathymetry using Fledermaus software. Figure 11 shows the resulting surface difference with positive or negative remaining values while figure 12 shows a graphical representation of the depth difference. A mean depth difference of 37 m and a standard deviation of 181 m were calculated.

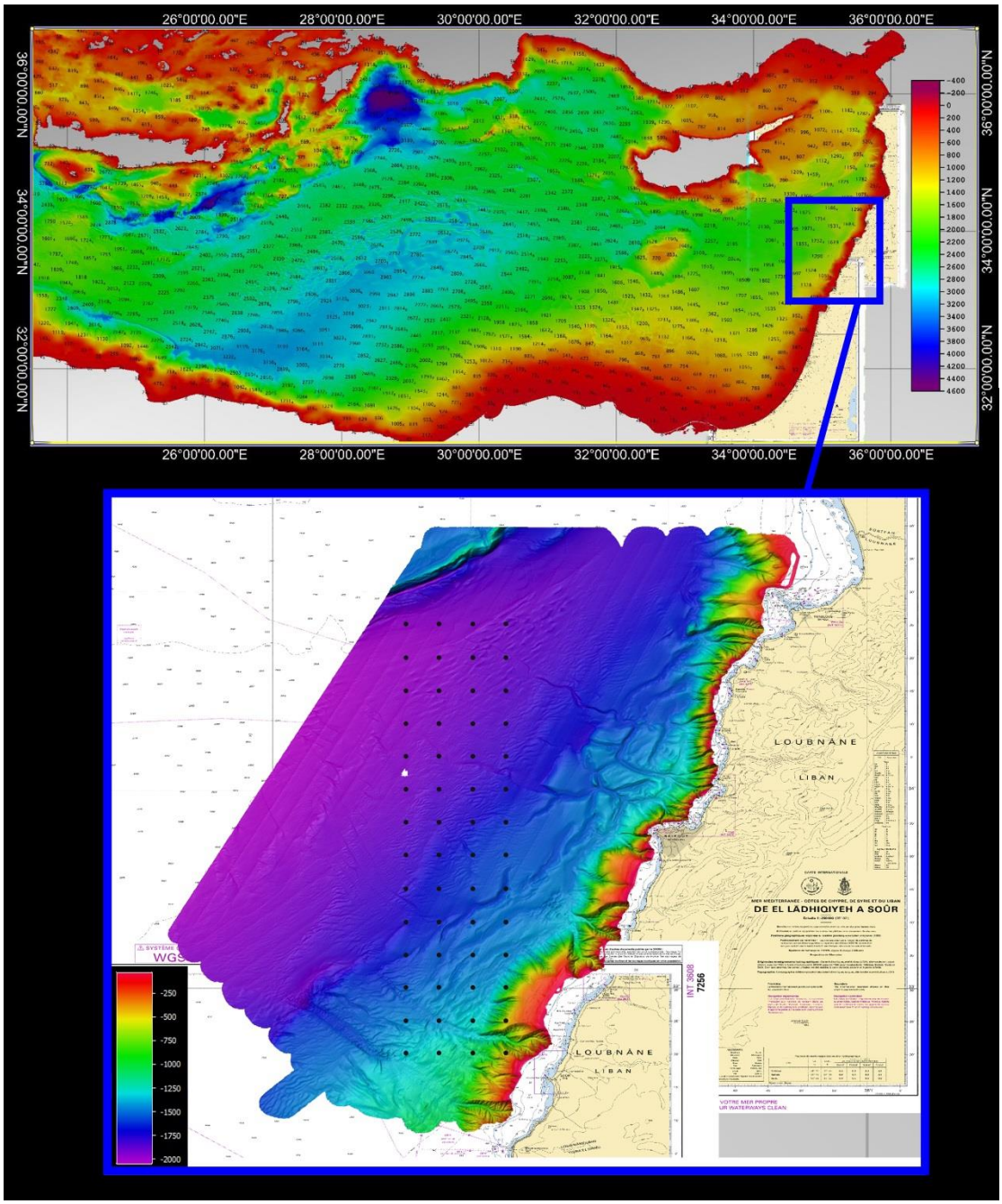

Fig. 10 Top: Bathymetric map of the Eastern Mediterranean Sea with sounding selection every 10 km. Bottom: SHALIMAR High-resolution bathymetric map of the Lebanese offshore. Black dots represent the 56 selected locations for bathymetric values comparison.

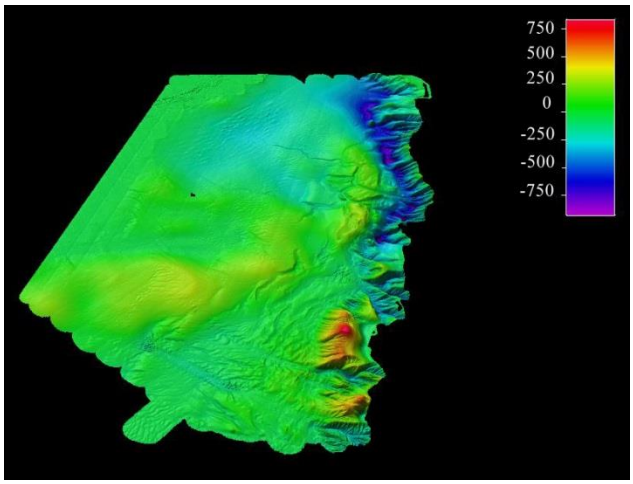

Fig. 11 Surface difference between EMODnet and SHALIMAR bathymetric surfaces.

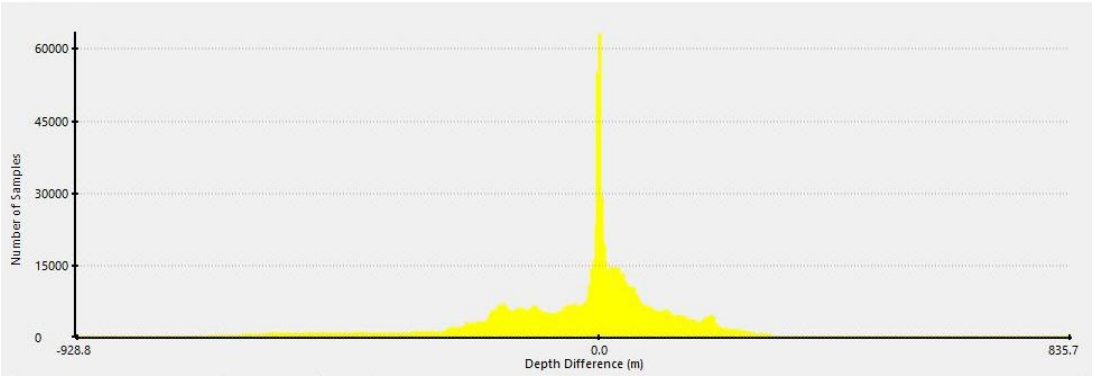

Fig. 12 Graphical representation of the depth difference between EMODnet and SHALIMAR bathymetric surfaces.

3.2.1 The Eastern Mediterranean Sea – Easternmost part

The Eastern Mediterranean Sea is a complex region with remarkable structural features that have been formed through a long tectonic history since the Early Permian (Fig. 13). These features include the Cyprus Arc, the Eastern Mediterranean Ridge, the Eratosthenes Continental Block (ECB), the Nile delta cone, the Herodotus Basin and the Levantine Basin (Inati et al., 2017).

The northwestern sector of the Eastern Mediterranean Sea includes the Rhodes, Finike and Antalya basins to the north and the Anaximander Ridge to the south. This sector is the junction between the northwest-southeast trending Florence Rise and the northeast-southwest trending Pliny-Strabo Trenches (Aksu et al., 2017). Depths in this northwestern sector reach a maximum of ~ 4500 m in the Rhodes deep marine basin. It is a deep trough between Rhodes Island to the west and southwestern Turkey to the east where the Finike basin deepens up to ~ 3000 m. Antalya basin has depths up to 2800 m in some locations. South of the Cretan Island arc, many depressions may be found and they consist of long and narrow trenches exceeding 3000 m depth.

Aksu et al., 2017, describe the Anaximander Seamounts as three prominent bathymetric highs, the Anaximander Seamount being an open V-shaped narrow and

arcuate ridge with its crest at ~ 1100 m depth, the Anaximenes Mountain a northeast-southwest trending broadly arcuate ridge with its crest at ~ 700 m depth, and the Anaxagoras Mountain a northwest-southeast trending broad bathymetric high with several prominent peaks at ~ 1200-950 m water depth. The Sırrı Erinç Plateau is a prominent arcuate zone characterized by corrugated seafloor located between the Anaximander Mountain and the combined Anaximenes and Anaxagoras Mountains with water depths ranging between 2100 m in the northeast (Finike Basin) and 3300 m in the west (Rhodes Basin) and the southwest (Aksu et al., 2009).
Antalya basin to the southwest of Turkey is situated in a forearc setting between the Florence Rise and the Cyprus Arc (Işler, F.I., et al. 2005) whereas the Adana basin (~1000 m water depth) occupies the southeast of Turkey. The Hecataeus Seamount or Rise to the south of Cyprus is characterized by a shallow seabed reaching minimum depths of ~ 230 m below sea level.

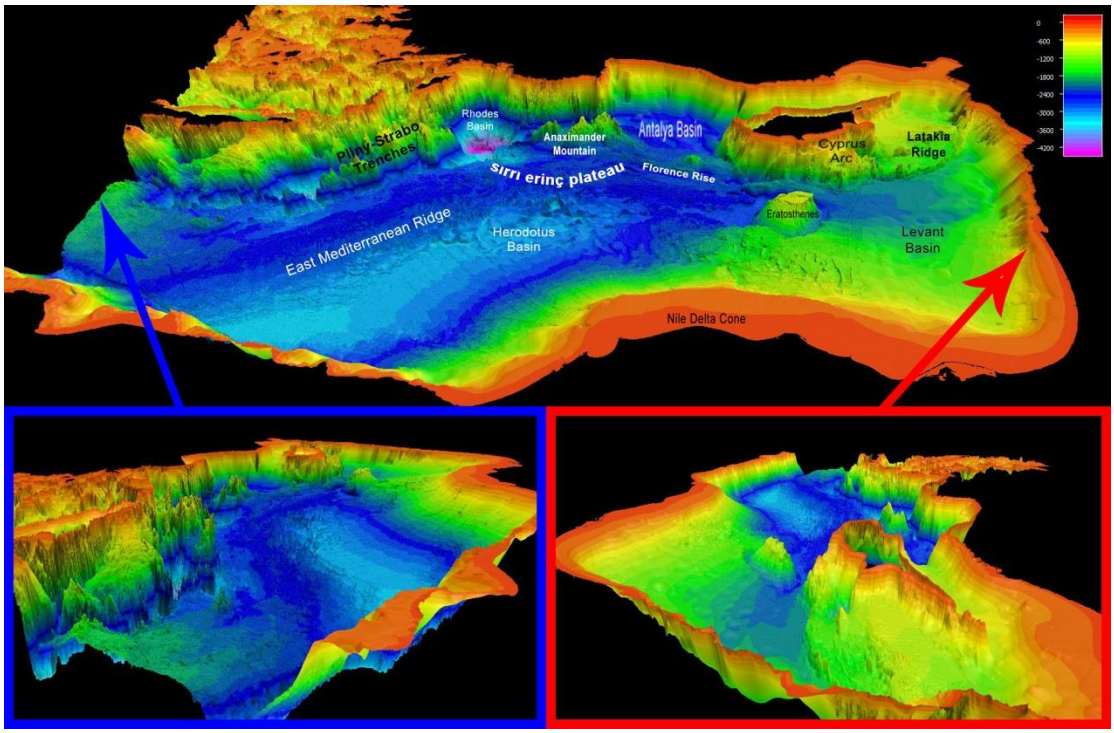

Fig. 13 Exaggerated 3D views of the Eastern Mediterranean Sea (Top: total area, blue arrow: view from West, red arrow: view from East) over which some important tectonic seabed features and basins are shown.

Hecataeus Rise has a southeast extension from the southern coast of Cyprus and then gradually merges with the Latakia Ridge. It constitutes the southern deformation front of the Cyprus Arc separating the Levantine Basin in the south from the Cyprus basin in the north. Cyprus has an EW elongated shape of about 230 km length and 100 km width in the NS direction. Latakia ridge is a steep narrow high with an east to northeastward trend that extends to the northern Levantine coast in Syria. This Ridge deepens gradually from the Syrian shelf till reaching 1700 m at the connection zone with the Hecataeus Rise. In the east, the expression of the ridge changes to several

narrow, northeast-trending ridges and basins (Hall *et al.* 2005b, Welford et al., 2015). Latakia ridge separates the Latakia basin from the northern Levantine Basin.
The southern margin of Cyprus is composed of ridges separated by small sediment ponds and depressions. Bathymetry clearly shows that the seafloor depth rises from ~2750 m till reaching the shelf break at about 400 m after following an irregular slope. The southern Cyprus shelf has a wider width ranging between 6 and 10 km in comparison with the narrower northern shelf.
The Levantine Basin to the easternmost sector of the Mediterranean displays two domains as shown in the present bathymetry. A shallow bathymetry reaching ~ 2100 m in the central part ("abyssal plain") and a maximum value of ~ 2600 m western of the Eratosthenes Seamount which constitutes its western boundary with the Herodotus. It has a narrow shelf to the East (Lebanon – Northern Israel coast) gets slightly larger in the southeast (Southern Israel – Sinai). The southern limit of the basin shows instead a relatively wider shelf (up to 70 km width due to sediment disposal from the Nile delta). In front of Lebanon and southern Syria, the slope toe is cut by fault scarps, deeply indented by sea valleys, a submarine promontory and submarine flat-floored canyons (Inati et al. 2017).
The Eratosthenes flat-topped seamount to the south of Cyprus and west of the Levantine Basin is an extremely elevated seabed feature (~ 1900 m) and a shallowest depth of ~ 700 m; It has been described as an NNE-SSW edifice (Papadimitriou, 2017). The Nile delta basin is located southwest of the Levantine Basin. Its sea fan characterized by depths ranging between 500 and 1600 m followed by the Herodotus basin to the West (depths reaching 3100 m in the centre of the basin). Herodotus basin has an elongated SW-NE shape (420 km length and 140 km width).

3.2.2 The Eastern Mediterranean Sea – Westernmost part

The second part of our area of interest, also considered a complex geological region, encompasses the Ionian, Libyan, Western Mediterranean Ridge and part of the Aegean Seas (Fig. 14). The marginal basin of the Aegean Sea which does not form a part of this study has particular hydrographic and topographic characteristics. The southern part of the Aegean Sea as shown by the bathymetric map views is connected and open to the Libyan and Ionian basins through the western Cretan Arc strait while from the eastern side of this strait the communication is established with the Herodotus and Levantine basins. Similar to the depressions found south of the Cretan arc, the Sirte abyssal plain south of the Mediterranean Ridge have deeper depressions reaching about 3100 m. Water depth in the Libyan Sea deepens gradually from the shelf till reaching 3000 m. The Libyan shelf width ranges between 30 and 60 km from the eastern to the western coast. A very narrow shelf is found in front of Cyrenaica. Due to its extension between the Central and Eastern Mediterranean Sea, the Mediterranean Ridge will be studied in this paragraph. This ridge which takes the form of an elongated arc-shaped bathymetric feature extends from the Ionian where water depth is 3200 m to the Western Levantine with depths of about 2500 m. The shallowest part, its summit in its central part north of Cyrenaica reaches 1300 m water

depth. This arc shape follows the Hellenic arc islands starting from the Peloponnesus peninsula and arriving south of Rhodes.

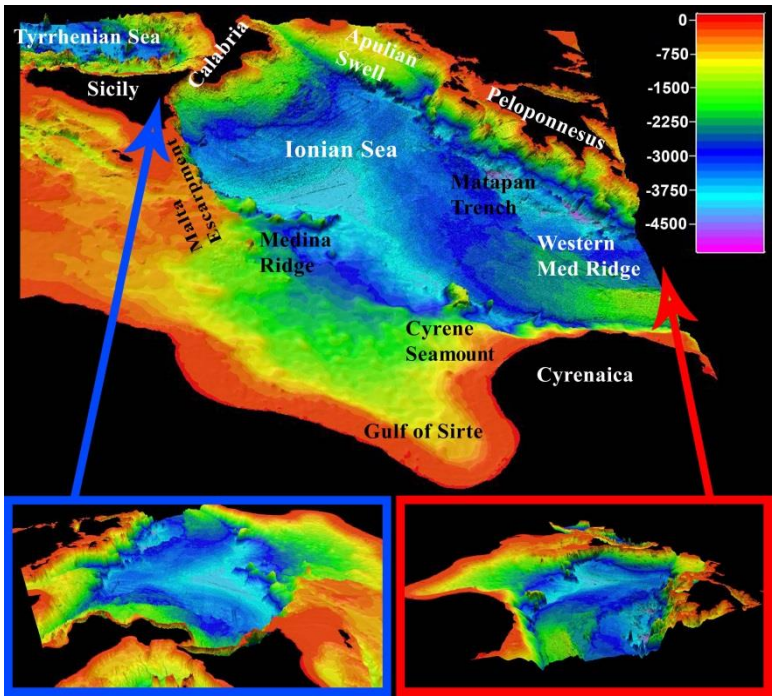

Fig. 14 Exaggerated 3D views of the Central Mediterranean (Top: total area. Blue arrow: view from West, Red arrow: view from East) and the main tectonic seabed features and basins are shown.

The Mediterranean Ridge is about 1500 km long and 100-200 km wide. This variable width starts with about 200 km in front of the Ionian deep abyssal plain and gets narrower with 135 km between Crete and Libya and about 110 km in the southeast of Crete. The change from western to the eastern ridge can be morphologically noticed by an inflexion modifying the ridge trending from NW-SE in the Ionian Sea to WSW-ENE towards the eastern part. The Western Mediterranean Ridge extends from offshore Libya (Antaeus High) to the transition with the Calabrian prism offshore the Ionian Islands. On the other hand, the centre ridge passes south of Crete and continues till the southwest of Turkey and south of Cyprus as an Eastern ridge.

The Mediterranean Ridge is limited to the north by the Hellenic Trench and to the south it is bounded from west to east by the oceanic Ionian abyssal plain, the Libyan continental margin and the Herodotus abyssal plain (Mascle et al., 1999).

The Mediterranean Ridge is bathymetrically bounded by the Pliny and Strabo trenches and the Rhodes trough in the eastern part and by the Matapan trench (~5100 m) in the northwest. These trenches are deep and disconnected series of trough. Small depressions and ridges characterize the bathymetry of the Mediterranean Ridge. Short wavelength folding is observed at the seafloor of the Mediterranean ridge giving it a "cobblestone topography" at the seafloor ridges and troughs (Kastens, Breen and Cita, 1992; Von Huene et al., 1997) North of Cyrenaica, the axial Mediterranean ridge is an almost flat area where the average water depth is 2000 m rising locally up to 1300 m.

The Ionian basin is positioned in the central Mediterranean Sea and bounded to the northwest by southern Italy (~430 km) including Calabria, Sicily (Sicily strait) and Salento peninsula, to the south by the Libyan Sea, to the northeast by southern

Albania and the east by Western Greek coast including the Peloponnese peninsula (~450 km). To the south, between Sicily and Greece, the largest opening occurs that reaches about 500 km, while the narrowest opening occurs to the north, with the Adriatic Sea, and is about 50 km wide. Water depth in the Ionian Abyssal Plain reaches 4100 m. The Ionian small and principal islands (Corfu, Kefalonia, Zakynthos, Lefkada and Ithaca) located east of the Ionian are Greek islands, and WSW of Pilos-Greece is located the Calypso Deep known to be the deepest position of the Mediterranean Sea with a depth of ~5200 m. Immediately outside the Ionian region, in the Attica region is found Kythira Island southern of Peloponnese. The Medina Ridge bounds the Ionian Basin to the south. Several seamounts (Victor Hensen Seahill 2 and the Victor Hensen Seahill) and structures are found North-East of the Ridge in the South-East Central Ionian. The Victor Hensen Seahill is described as a 10 km long and 2 km wide SW-NE elongated tectonic structure and rises about 340 m above the seafloor (Emeis et al., 1996). NW of the Victor Hensen Seahill, three subbottom structures were found: the Nathalie and the Valvidia structures and the Victor Hensen Seahill interpreted as the SW-NE oriented sub-bottom continuation of the Victor Hensen Seahill (Gallais et al., 2011).

3.3 Sea-bottom profiles

Figure 15 shows nine bathymetric profiles which were created from the bathymetric map to highlight details concerning the morphology and structure of the study area.. They will help in selecting zones free of tectonic deformations and where subsidence is most probably related to cooling and stretching.

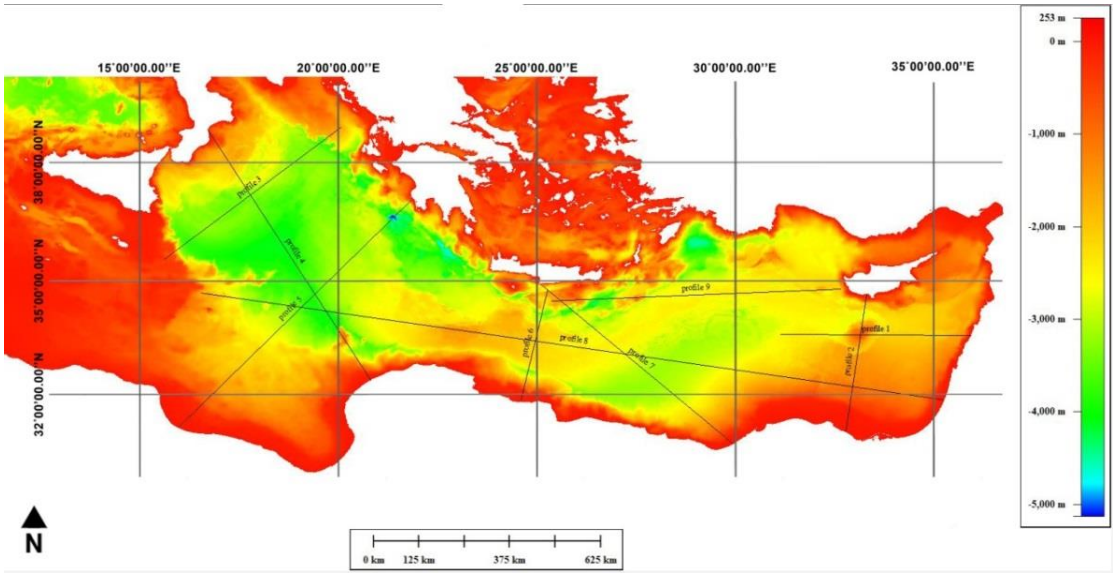

Fig. 15 Bathymetric vertical profiles along 9 paths of the study area.

The first 438 km EW profile (Fig. 16) runs from the eastern Levantine coast of Lebanon, over the Eratosthenes Seamount till the Herodotus Basin. The profile clearly shows the narrow shelf of the Easternmost Mediterranean margin followed by a rapid

slope till reaching the deeper parts in the Levantine Basin. The Eratosthenes Seamount, surrounded by a scour (trough) of hundred meters, has an elevated topography and is followed directly to the west by the Herodotus Basin where water depth is larger (2600 m) than in the Levantine. A maximum slope value of ~ 18 ˚ is observed near the top eastern side of the seamount, at a distance of 240 km along the path.

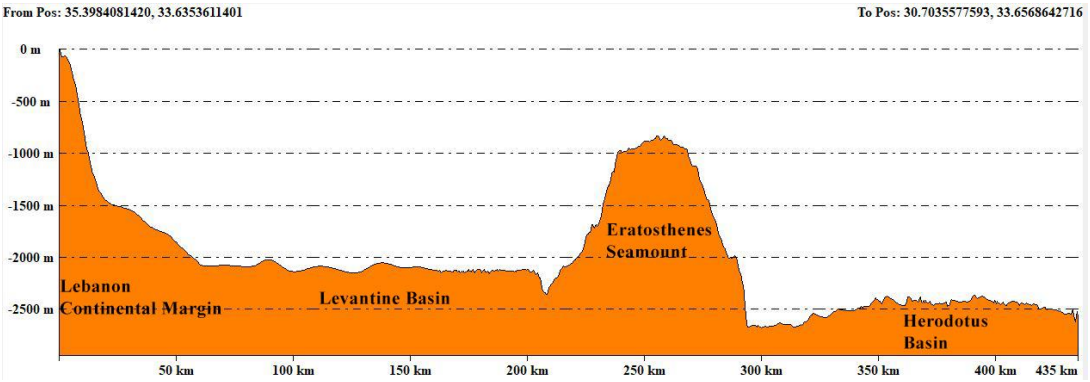

Fig. 16 Bathymetric vertical profile 1 (see location in figure 15).

The second profile, 377 km long (Fig. 17), in the easternmost part of the Mediterranean, runs from south to north starting from the northern Egyptian continental margin characterized by a wider shelf than the eastern margin observed in profile 1. It was selected since it runs parallel to an existing seismic profile and cuts through heat flow measurements spots, drilling locations and general sediment thickness data. Passing through the Nile Delta Cone, depths get higher when reaching the deeper part of the Levantine Basin but with a slower trend than profile 1. The erosional channel surrounding the Eratosthenes Seamount is also observed in that direction being deeper and sharper in its southern margin and more extended in its northern margin. Between Eratosthenes Seamount and Cyprus, a trough of hundred meters is also noted and making the boundary with the steep slope (16˚) connecting to the relatively short shelf of Cyprus southern margin.

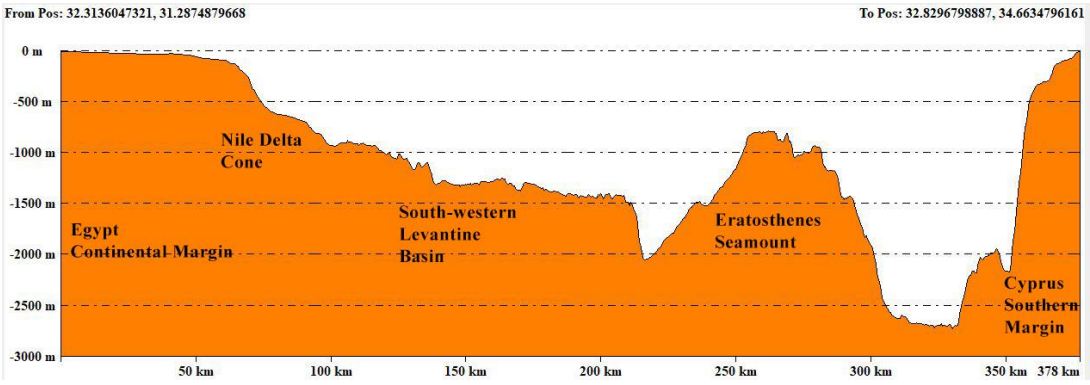

Fig. 17 Bathymetric vertical profile 2 (see location in figure 15).

The third profile of 525 km (Fig. 18) is in the Central Mediterranean and connects the Malta escarpment zone with the Apulian one, where a maximum path slope of 26 ˚ is observed, through the abyssal plain of the Ionian Basin. Maximum depths are noted at both escarpment toes reaching the higher value of 3776 m at the Malta escarpment trough.

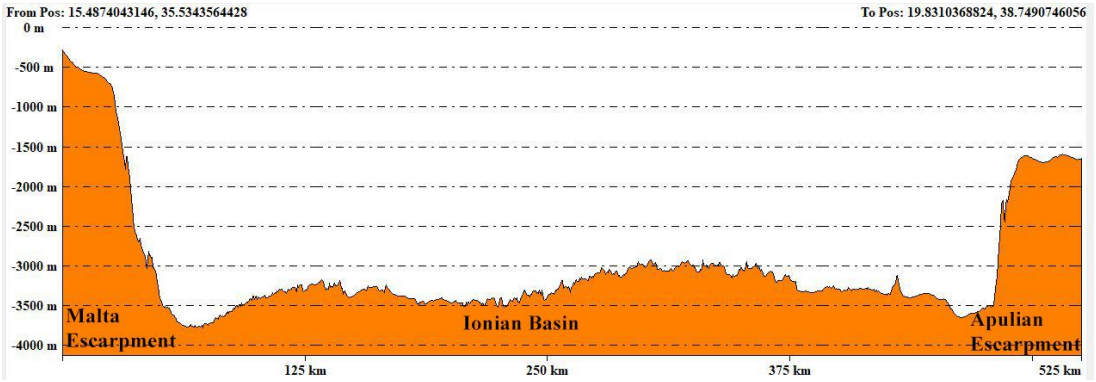

Fig. 18 Bathymetric vertical profile 3 (see location in figure 15).

Profile number 4 of 769 km length (Fig. 19) orthogonal to profile number 3 starts from Calabria (Italian southern margin) and arrives at the Libyan margin (Cyrenaica) through the Ionian Basin abyssal plain. The profile shows some irregularities of the Calabrian continental margin (deformation zone?) which then gradually deepens into the central Ionian reaching a water depth of 4100 m. At about 600 km is found the Cyrene Seamount rising over the seabed with 1000 m depth and characterized by a high slope of 25˚ then followed by a depression and the slope of the Sirte continental margin.

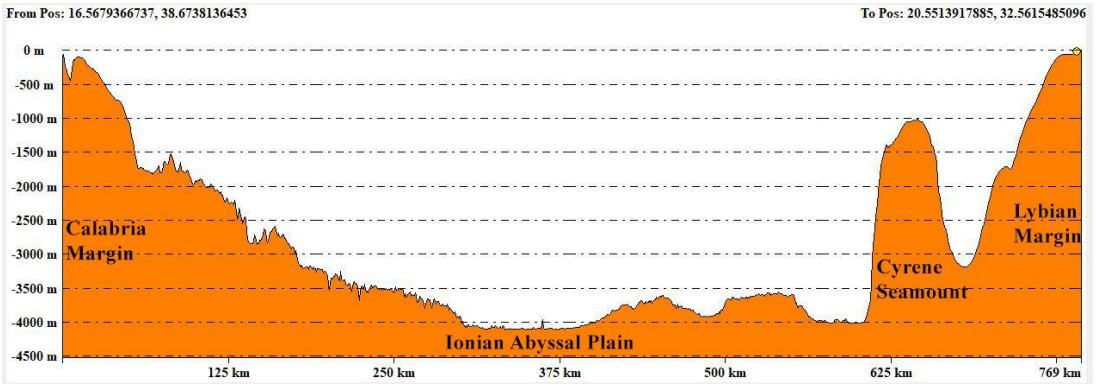

Fig. 19 Bathymetric vertical profile 4 (see location in figure 15).

The SW-NE 815 km length profile 5 (Fig. 20) diagonally cuts the southern limit of the Ionian Basin and the westernmost part of the western Mediterranean Ridge departing from the Sirte continental margin and arriving at Peloponnesus coasts. The profile is characterized by a gentle depth increase till the ~ 3900 m of the southern Ionian Basin. Water depth decrease to 3000 m due to the Mediterranean Ridge. This profile then crosses the Matapan trench (~5000 m) before climbing up steeply (38 ˚) a very narrow shelf at the southwestern Peloponnesus peninsula.

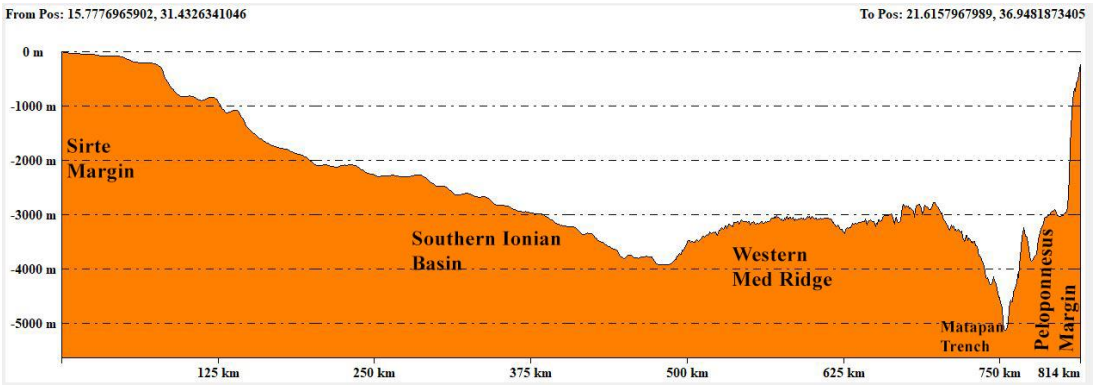

Fig. 20 Bathymetric vertical profile 5 (see location in figure 15).

In the middle of the study area at the limit between the Central and Eastern Mediterranean Sea, a 335 km nearly SN profile number 6 (Fig. 21) joins the northern Libyan coast with the southern Crete one in an area characterized by some of depressions. The Libyan shelf at this position is wide and followed by a relatively gradual descending slope which leads to a first depression (3400 m) south of the Mediterranean Ridge followed to its north by a second slightly deeper depression of 3610 m. The following bathymetric behaviour is irregular in a compressional area where a third depression immediately before the narrow Cretan shelf is found. The slope after the Cretan shelf is very steep reaching up to 34˚at 330 km along the path.

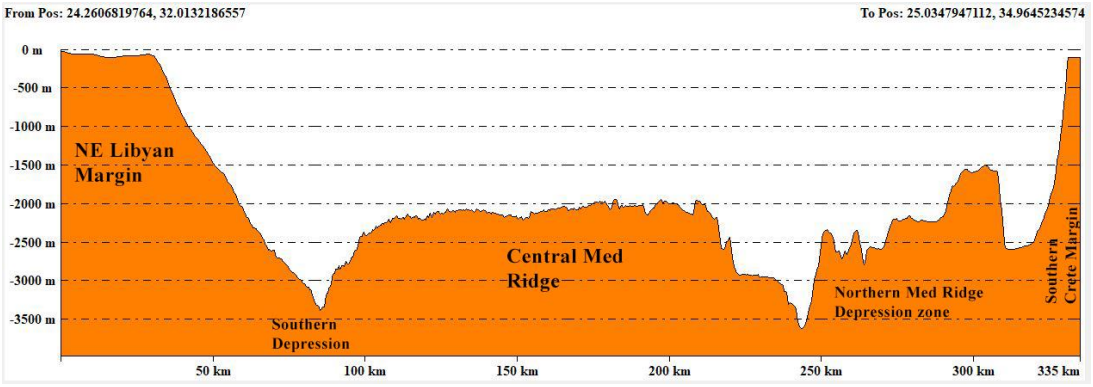

Fig. 21 Bathymetric vertical profile 6 (see location in figure 15).

The Eastern Mediterranean Ridge was vertically investigated by the SE-NW 7th profile of 620 km (Fig. 22) running from the north-western Egyptian coast to the southern part of Crete Island. The shelf of the Egyptian margin at this location is of average width and depth afterwards gently increases till reaching ~ 3200 m in the Herodotus abyssal plains. Water depth re-increase over the Mediterranean Ridge up to 2500 m before passing through the Pliny trench having a steep slope (~ 36˚).

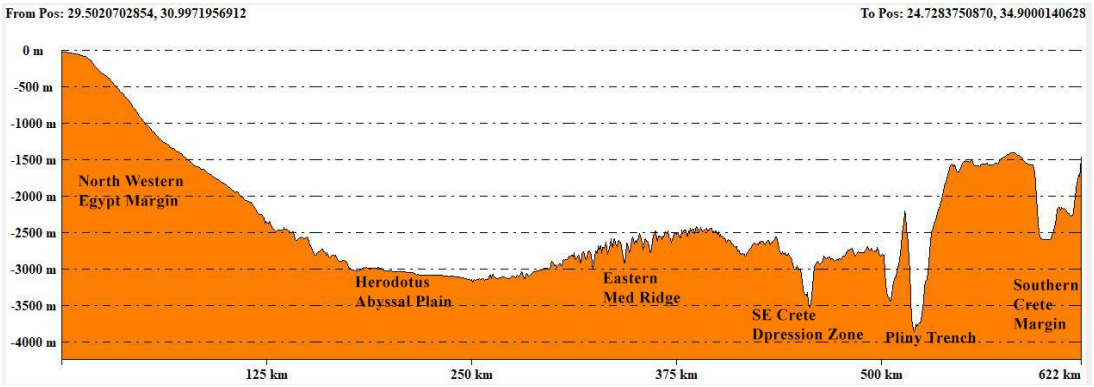

Fig. 22 Bathymetric vertical profile 7 (see location in figure 15).

The longest of the profiles with a length of 1750 km is profile 8 (Fig. 23) cutting through the study area from its western part at the southern Malta escarpment zone till the south-eastern Levantine coast through the Sirte abyssal plain, the Mediterranean Ridge, Herodotus and Levantine basins. Bathymetry follows a gradual descending pattern along the deformation front from 1000 m depth till reaching ~ 3900 m in the Sirte abyssal plain. Water depth decreases over the Mediterranean Ridge up to ~ 1800 m followed by increasing depths in the Herodotus ~ 3100 m. Towards the ESE end of the profile, water depth continues increasing in the southern Levantine Basin before ending at the narrow shelf of the easternmost Mediterranean continental margin.

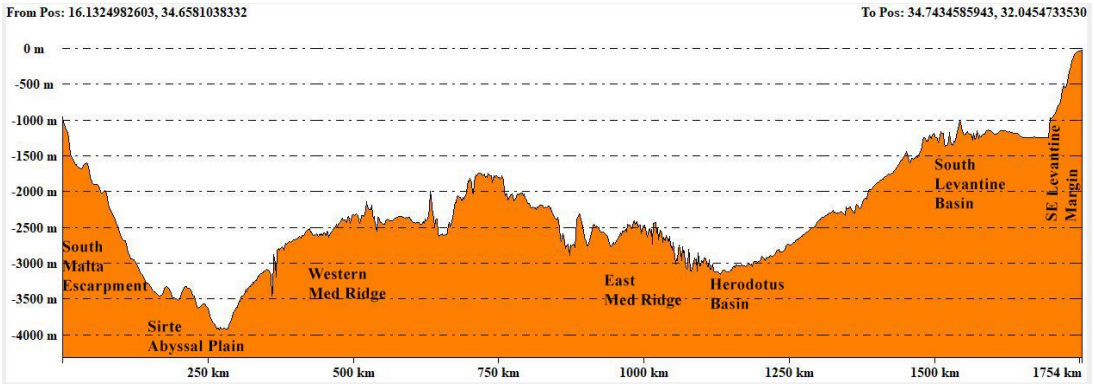

Fig. 23 Bathymetric vertical profile 8 (see location in figure 15).

Profile number 9 (Fig. 24) was chosen as it runs through global sediment thickness data, drilling site and heat flow measurement spots. It is a 657 km length profile. A maximum slope value of 16˚is observed at 214 km from the starting of the profile in a zone of compressional tectonics. It starts westerly from southern Crete elevated seafloor than gets deeper in the depressions zone and trenches. After which it passes through the Eastern Mediterranean Ridge (~2500 m depth) and then reaches the deep part of the western Cyprus continental margin.

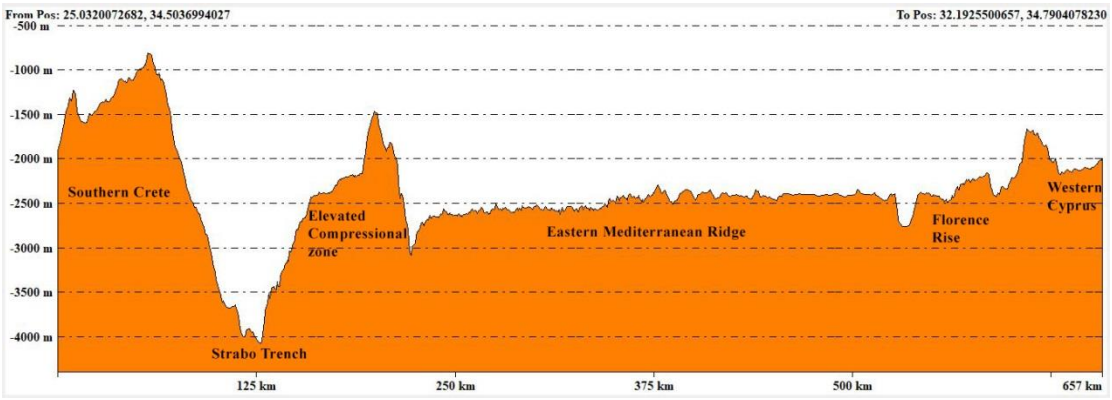

Fig. 24 Bathymetric vertical profile 9 (see location in figure 15).

3.4 Slope computation

The two asci grid files for the blocks C4 and D4 of the Central and Eastern Mediterranean Sea downloaded from the EMODnet portal were loaded into Fledermaus software. A slope computation was conducted and a slope values distribution surface for the study area was generated (Fig. 25).

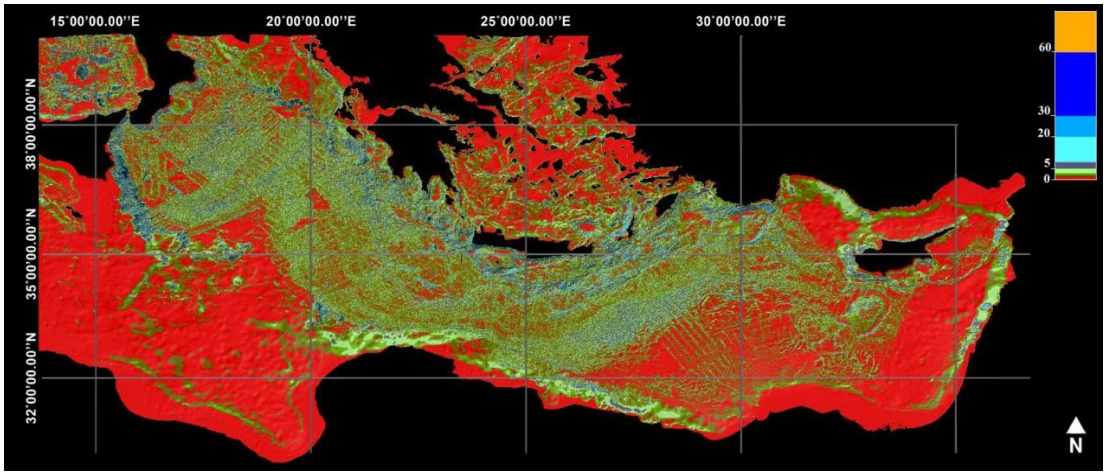

Fig. 25 Map of the slope values in degrees in the study area. Red color is relative to relatively flat bottoms. Increasing slopes are represented by colors passing from green to blue.

A personalized colour interval colour map was created to better discriminate the slope changes especially for detecting the smallest changes. The Central and Eastern Mediterranean basins plains are surrounded by slopes that range between 3° and in some specific locations reach 40 to 50°. In general, the Levantine Basin is characterized by a steep slope where water can suddenly increase from 100 – 200 m to 1000 – 1500 m offshore northern Syria, Lebanon and Israel. The abyssal plain of the Levantine is a nearly flat zone. In the same way, the southeast margin of Cyprus and northern deformation front of Eratosthenes seamount present interesting slope values. Sharp troughs along main trenches northern of Cyrenaica-Libya, southern Crete and depressions western of Peloponnesus are areas of typical high slope values.
The Ionian Basin in Central Mediterranean is bounded by higher slope values than the Eastern Levantine Basin especially at the Malta escarpment zone. The Mediterranean Ridge slope has low values and weakly varies along the Ridge differently from other

accretionary systems. It starts at 2° across the front of the accretionary wedge (sediment cover from the African plate subducting beneath Eurasia at the Mediterranean Ridge) and gets flatter in the middle of the ridge. Von Huene (1997) describes this topography of ridges and troughs by "cobblestone topography". Moatlike basins, such as the Bannock structure, surrounded by a central steep-sided hill, and small sea hill features in the study area are characterized by relatively steep slopes (up to 25°). Southwest of Crete, the almost flat Mediterranean Ridge is bounded by steep slopes of ~10° interpreted as back thrust or transpressive fault zones between the axial and inner Mediterranean Ridge domains (Mascle et al., 1999). In the Central Libyan zone of the Mediterranean Ridge, some sloping may be observed and correlated to doming as mud diapiric field (Toronto volcano).

4. GEOTHERMAL FLOW

Surface heat flow is fundamental for understanding the internal processes and mantle dynamics. The thermal energy from the asthenosphere plays an important role in the uplift and subsidence of the lithosphere. Thus, the study of the thermal state of the Eastern Mediterranean basins has particular importance. In this section, a revision of heat-flow data available in the Eastern Mediterranean Sea was conducted.

The marine heat-flow (HF) determinations in the Eastern Mediterranean Sea, collected during several surveys since the 1970s were extracted from the Global Heat Flow Database (GHFD) Release 2021 (https://doi.org/10.5880/fidgeo.2021.014). Data were mostly obtained with the classical Ewing probe penetrating the seafloor sediments, and part of them were derived from temperature logging in deep-sea boreholes and from bottom hole temperatures (BHTs) recorded in oil wells (Fig. 26).

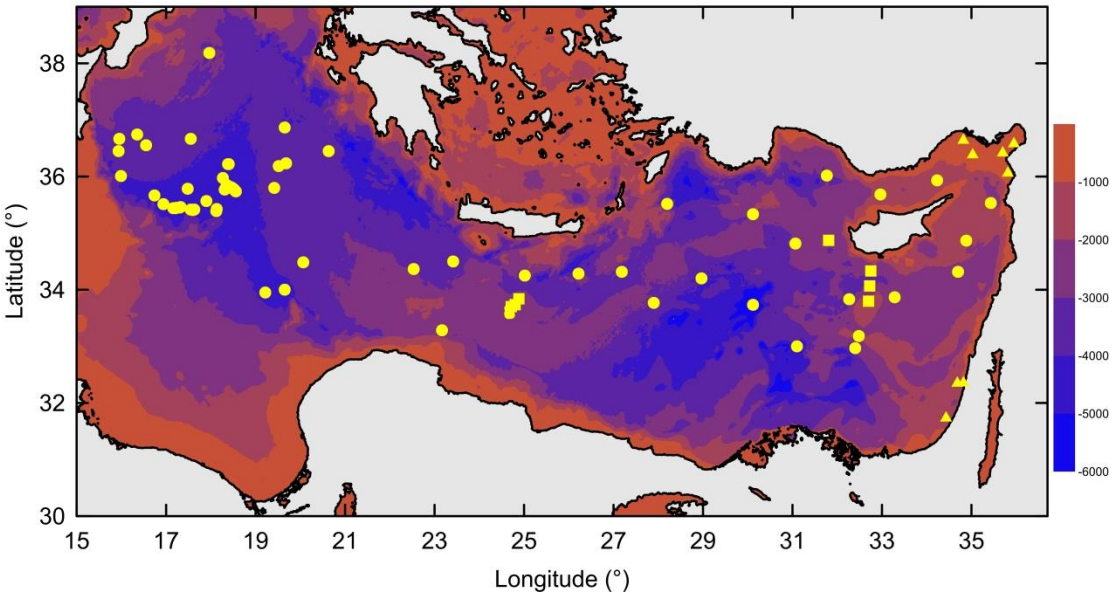

Fig. 26 Location of heat flow data in the Eastern Mediterranean Sea available from the Global Heat Flow Database (GHFD), Release 2021 (Fuchs et al., 2021) and depth of the bottom of the Plio-Quaternary sediments, and bathymetry obtained by interpolating data on a regular grid with a spatial resolution of 1 arc-minute (sediment thicknesses after Capponi et al., 2020; bathymetry from the ETOPO1 model by Amante and Eakins, 2009). Yellow dots = data obtained with the classical Ewing probe penetrating the seafloor sediments; yellow squares = data from temperature logging in deep-sea boreholes (ODP and DSDP); yellow full triangles = data from bottom hole temperatures (BHTs) recorded in oil wells.

4.1 Heat flow data correction

Several effects, such as thermal refraction, sedimentation, climatic changes, topography and uplift/erosion, are in principle capable of biasing the true, purely conductive, steady-state heat flow.

Thermal refraction, i.e., the preferential flow of heat through high-thermal conductivity structures, such as salt domes, may be one cause of strong local variability in the heat-flow measurements. This disturbance does not appear to be relevant, as the salt layer (Messinian evaporites) seems rather uniform in thickness and ubiquitous in the investigated area (Erickson and Von Herzen, 1978).
Sedimentation and long-term changes in the sea-floor temperature can instead have major effects on the observed heat flow. In the light of the stratigraphic and climatic data achieved to date, we revised the observed heat flow dataset to remove such effects.

4.1.1 Sedimentation

I evaluated the blanketing effect only due to the most recent sedimentation (Plio-Quaternary) through the simplified approach by Von Herzen and Uyeda (1963), which assumes a constant sedimentation rate and no compaction or associated fluid expulsion. Thermal diffusivity of 9.5 m^2 a^{-1} was assumed in the calculation of the sedimentary correction (Verdoya and Chiozzi, 2018). The Plio-Quaternary deposition cycle was assumed as a single event, which took place on the Miocene deposits acting as a basement. Values of sediment thickness were extracted from the map of the Plio-Quaternary sediment depths in the Mediterranean Sea, proposed by Capponi et al. (2020). This map is based on the IBCM-PQ thickness map, expressed in two-way travel times by Genesseaux et al. (1998).

4.1.2 Paleoclimatic changes

The correction for the temperature variation in response to paleoclimatic changes was also evaluated. The marine data correction was based on the paleoclimate model proposed by Pasquale et al. (2005), which allows for the climatic history of the Mediterranean Sea.

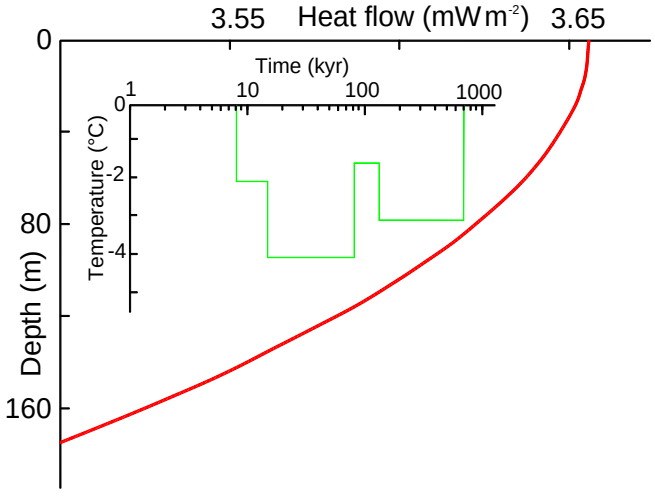

Fig. 27 Heat flow variation with depth (red curve) due to the bottom water temperature history in the Eastern Mediterranean Sea over the past 0.7 Ma (green curve).

Jemsek (1988) reported several pieces of evidence for the climatic history in the entire Mediterranean Sea and concluded that the temperature history of the bottom water in the Central-Eastern Mediterranean shows smaller changes than in the western part of the basin.

Based on these data, it seems that during the last 8 ka no change in the sea bottom temperature has occurred, whereas a decrease of 3 °C, i.e., half of that of the Western Mediterranean Sea can be assumed from 700 to 135 ka ago (Fig. 27).

Cooling was followed by three other cold periods. The lowest temperature occurred from 82 to 18 ka ago. By considering a thermal diffusivity of 9.5 m^2 a^{-1} and the average conductivity of the Plio-Quaternary sediment of 1.0 W m^{-1} K^{-1}, the climatic correction near the surface is, in terms of heat flow, of 3.7 mW m^{-2}.

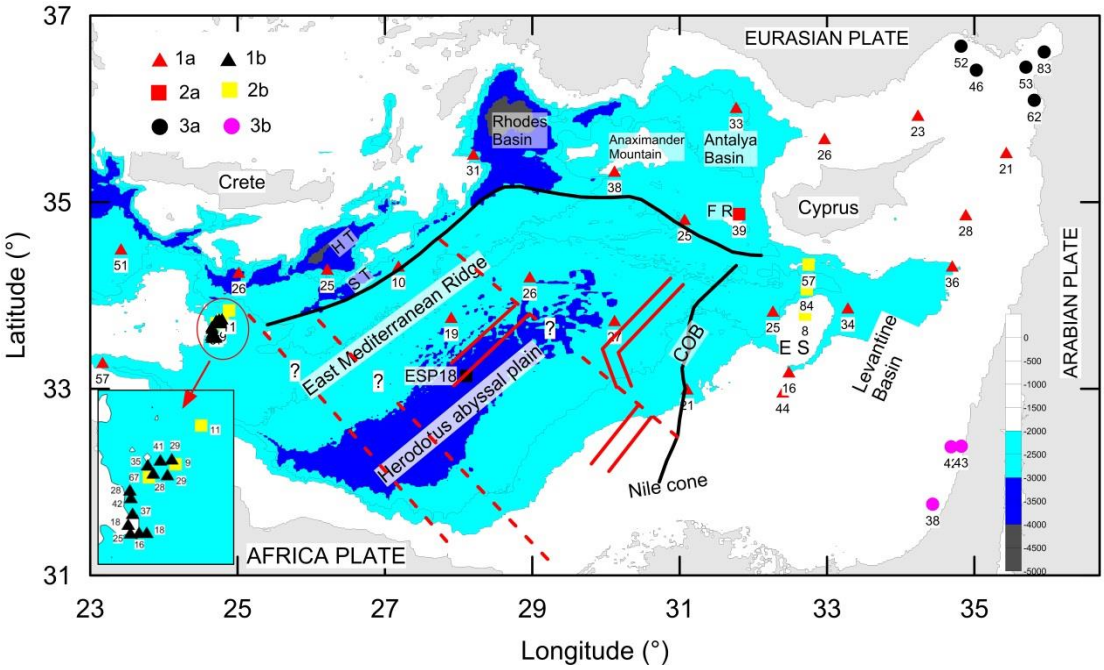

Fig. 28 Location of observed (uncorrected) heat-flow data (in mW m^{-2}) of the Easternmost Mediterranean Sea available from the Global Heat Flow Database (GHFD), Release 2021 (Fuchs et al., 2021): 1a = Erickson (1970); 1b = Camerlenghi at al. (1995); 2a = Erickson and Von Herzen (1978); 2b = Pribnow et al. (2000); 3a = Tezcan and Turgay (1991); 3b = Shalev et al. (2013). Bathymetry (in m) is derived from the global seafloor database V18.1 (Smith and Sandwell, 1997), from satellite altimetry and ship depth soundings (http://topex. ucsd.edu/cgi-bin/get_data.cgi). ES = Eratosthenes seamount, ST = Strabo Trench; HT = Hellenic Trench; FR = Florence Rise. Structural data after Granot (2016): red lines denote magnetic isochrones; the dashed red lines delineate the location of suspected fracture zones based on magnetic anomaly offsets and the gravity; COB is the continent-ocean boundary.

4.2 Heat flow in the eastern sector of the EMS

The marine heat-flow (HF) sites are shown in figure 28 (Chiozzi et al., 2021). The database was also cross-checked with that by Lucazeau (2019). We revised data by checking the original publications to identify misplaced or forgotten data (see Fuchs et al., 2021a) and followed the new standard for reporting and storing heat-flow data in the Global Heat Flow Database (Fuchs et al., 2021b). All HF data were considered

reliable except for one HF value (CH61-67) by Erickson (1970), as the author himself considered it of poorer quality.

A total number of 49 heat flow data is available for the investigated area (Table 1). Marine data were mostly obtained with the classical Ewing probe penetrating the seafloor sediments: 22 values from Erickson (1970) and 12 values from Camerlenghi et al. (1995). Seven values were obtained from temperature logging in deep-sea boreholes (one value by Erickson and Von Herzen, 1978; 6 values by Pribnow et al., 2000). Eight values were derived from bottom hole temperatures (BHTs) recorded in oil wells by Tezcan and Turgay (1991) and by Shalev et al. (2013).

The dataset contains heat flow values (uncorrected for terrain effects) ranging from 8 to 84 mW m^{-2}, and the average is 34±17 mW m^{-2}. Table 2 shows a summary of the heat flow data obtained with the different methods. Since means and standard deviations may be inflated by outliers, we preferred to rely on median values (Q2) and interquartile ranges (Q1 and Q3)). The median is 29 mW m^{-2} while the interquartile range is 25-42 mW m^{-2}. They indicate that the HF is rather low in the investigated area. The largest heat flow was measured close to the continental areas and in particular in the BHT sites, in which the median value increases to 49 mW m^{-2}.

Concerning the HF sites investigated with the penetrating thermal probe, most of them (28 out of 34) exceeds 2000 m depths. In the Herodotus Basin, wherein oceanic lithosphere is likely to occur, three HF data are available (Fig. 29 and Table 2 for details).

Table 2 Median values (Q2) and interquartile ranges (first Q1 and third Q3 quartiles) of the heat flow (in $mW.m^{-2}$) data recorded with different methods (location in Fig 26). n = Heat flow site number, Max = maximum value; Min = minimum value.

Exploration method	***n***	***Q1***	***Q2***	***Q3***	***Min***	***Max***	**Reference**
Probing	34	28	25	35	10	57	Erickson (1970); Camerlenghi et al. (1995)
DSDP-ODP (drilling)	7	10	39	62	8	84	Erickson and Von Herzen (1978); Pribnow et al. (2000)
BHT (drilling)	8	43	49	55	38	83	Tezcan and Turgay (1991); Shalev et al. (2013)
All data	49	25	29	42	8	84	

The Herodotus Basin data were obtained from measurements with an Ewing type probe at a seafloor depth ranging from 2600 e 2800 m. Site C9-117 and CH61-53 are consistent with the median of data obtained with the Ewing type probe whereas site C9-118 shows a remarkable deviation (Table 3). This may be due to localized

environmental disturbances (fluid flow?) rather than to thermal disturbances in the crust or upper mantle. By combining the sediment and paleoclimate correction, the unbiased heat flow values of the Herodotus Basin are 46, 24 and 36 mW m^{-2} for sites C9-117, C9-118, and CH61-53, respectively.

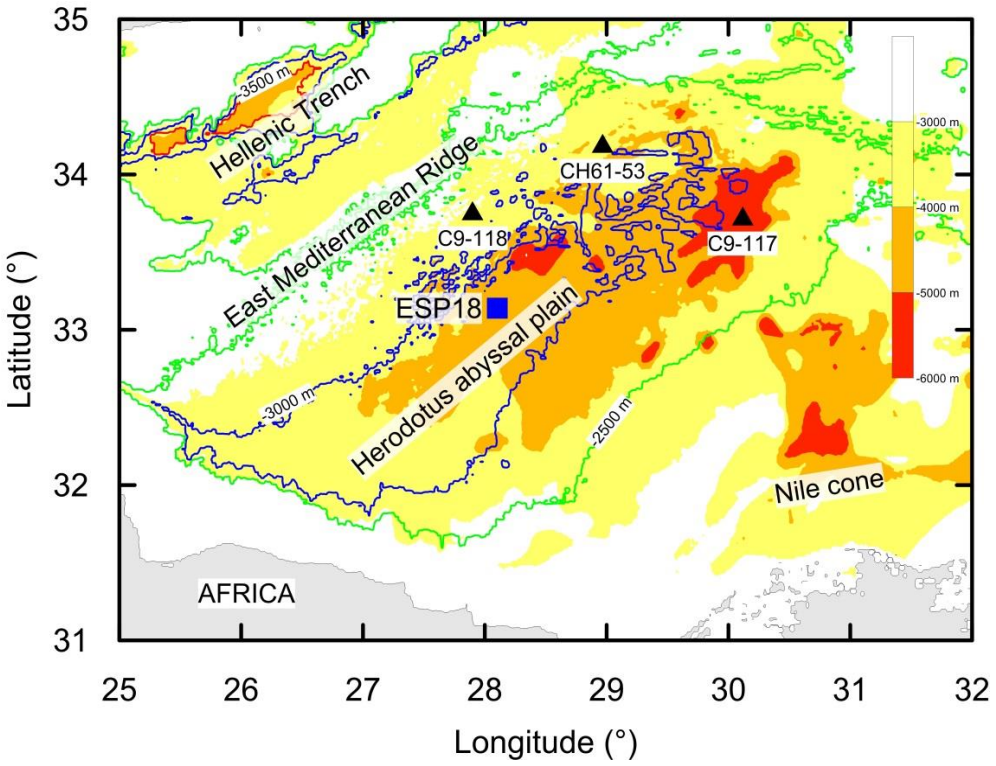

Fig. 29 Location of the heat flow data of Table 2, depth of the bottom of the Plio-Quaternary sediments, and bathymetry obtained by interpolating data on a regular grid with spatial resolution of 1 arc-minute (sediment thicknesses after Capponi et al., 2020; bathymetry from the ETOPO1 model by Amante and Eakins, 2009). Site of the seismic profiles ESP18 (de Voogd et al., 1992) is also shown. -2500 m (green line), -3000 m (blue line) and -3500 m (red line) bathymetries of the global seafloor database V18.1 by Smith and Sandwell (1997), derived from satellite altimetry and ship depth soundings (http://topex. ucsd.edu/cgi-bin/get_data.cgi), are shown.

Table 3 Terrestrial heat flow data (HF) in the oceanic lithosphere of the Herodotus Basin. nT = temperature number; k = thermal conductivity; G = thermal gradient. In parenthesis, standard deviation.

Site	**Long**	**Lat**	**Elev. (m)**	**Penetr. (m)**	**nT**	**G(mK m^{-1})**	**Nk**	**k (W m^{-1} K^{-1})**	**HF (mW m^{-2})**
C9-117	30.1167	33.7333	-2775	9.1	2	28.8 (2.3)		0.93	26.8 (3.3)
C9-118	27.9000	33.7667	-2622	8.5	2	17.8 (2.3)		1.05	18.7 (3.3)
CH61-53	28.9667	34.2000	-2603	7.8	5	30.2 (4.6)	49	0.88 (0.10)	26.6 (5.4)

4.3 Heat flow in the western sector of the EMS

Many heat-flow data, collected during several surveys (Pasquale et al., 2005 and references therein), are available for the Ionian Sea (Fig. 30 and Table 4). Data were obtained with conventional marine techniques (classical Ewing probe penetrating the seafloor sediments) and, in one case (site 7I), from temperature logging along a deep-sea borehole. The dataset contains heat flow values (uncorrected for terrain effects) ranging from 14 to 73 mW m^{-2}, and the average is 37±11 mW m^{-2}. The median is 36 mW m^{-2} while the interquartile range is 32-42 mW m^{-2}. These values indicate that the HF is rather low in the wester sector. The largest heat flow was measured close to the continental areas along the Mediterranean Ridge.

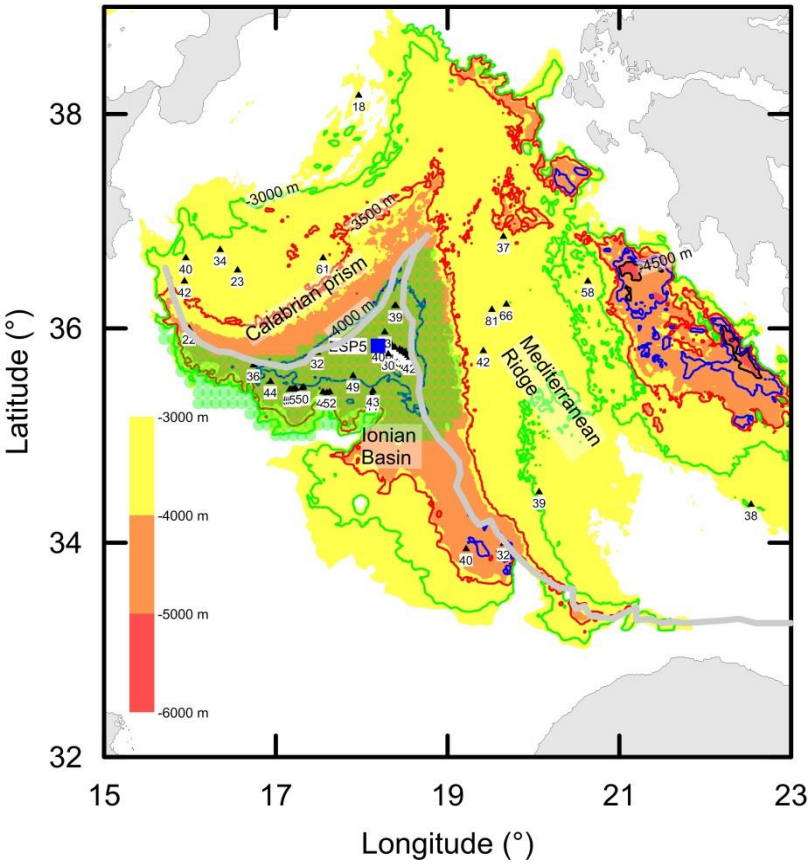

Fig. 30 Location of the corrected heat-flow data of Table 6, depth of the bottom of the Plio-Quaternary sediments, and bathymetry obtained by interpolating data on a regular grid with a spatial resolution of 1 arcminute (sediment thicknesses after Capponi et al., 2020; bathymetry from the ETOPO1 model by Amante and Eakins, 2009). The site of the seismic profile ESP5 (de Voogd et al., 1992) is also shown. -3000 m (green line), -3500 m (red line); -4000 m (blue line) and -4500 m (black line) bathymetries of the global seafloor database V18.1 by Smith and Sandwell (1997), derived from satellite altimetry and ship depth soundings (http://topex. ucsd.edu/cgi-bin/get_data.cgi), are shown. The limits of Calabrian Arc and Mediterranean Ridge (grey line) by Tugend et al. (2019) and the oceanic crust (green hatch) by Seton et al. (2020) are also indicated.

Table 4 Terrestrial heat flow (HFoss) corrected for sedimentation and paleoclimatic effects (HFcorr) for the Ionian Sea. G = Thermal gradient, k = thermal conductivity, PQ = Plio-Quaternary.

Site	Lat	Long	G (mK m^{-1})	K (W m^{-1} K^{-1})	HF_{oss} (mW m^{-2})	Elev (m)	PQ thickness (m)	HF_{corr} (mW m^{-2})	References
1C	36.74	16.35	34.9	0.83	29	-3280	310.0	34	Della Vedova and Pellis (1992)
2C	36.55	16.55	21.2	0.85	18	-3400	330.0	23	Della Vedova and Pellis (1992)
3C	36.67	17.55	65	0.83	54.0	-3400	340.0	61	Erickson et al. (1977)
4C	38.18	17.97	13	1.04	13.5	-2348	452.0	18	Erickson et al. (1977)
1H	36.87	19.65	28.3	1.1	31.1	-3373	477.0	37	Erickson et al. (1977)
2H	36.45	20.63	59.3	0.85	50.4	-2760	460.0	58	Erickson et al. (1977)
3H	36.23	19.68	76.1	0.75	57.1	-3115	555.0	66	Erickson et al. (1977)
4H	35.80	19.42	33.1	1.11	36.7	-3304	336.0	42	Erickson et al. (1977)
5H	34.48	20.07	29.2	1.11	32.4	-2860	510.0	39	Erickson et al. (1977)
6H	34.00	19.65	27.3	0.96	26.2	-3955	495.0	32	Erickson et al. (1977)
7H	34.37	22.53	27.4	1.16	31.8	-2679	521.0	38	Erickson et al. (1977)
8H	36.18	19.52	66.1	1.11	73.4	-3290	310.0	81	Erickson et al. (1977)
1I	36.67	15.95	42.2	0.83	35	-3285	295.0	40	Della Vedova and Pellis (1992)
2I	36.45	15.94	43.4	0.83	36	-3345	325.0	42	Della Vedova and Pellis (1992)
3 I	36.01	15.99	20.5	0.83	17	-3685	355.0	22	Della Vedova and Pellis (1992)
4 I	36.22	18.39	27.5	1.2	33	-4070	350.0	39	Della Vedova and Pellis (1992)
5 I	36.22	18.40	27.5	1.2	33	-4070	350.0	39	Della Vedova and Pellis (1992)
6I	35.97	18.27	23.3	1.2	28	-4085	365.0	33	Della Vedova and Pellis (1992)
7I	35.85	18.20	27.7	1.23	34	-4078	342.0	40	Erickson and von Herzen (1978)
8I	35.78	17.48	32	0.84	26.9	-4036	384.0	32	Erickson et al. (1977)
9I	35.67	16.74	36.9	0.84	31	-3925	325.0	36	Della Vedova and Pellis (1992)
10I	35.85	18.35	37.1	0.96	35.6	-4087	333.0	41	Della Vedova and Pellis (1992)
11I	35.83	18.39	38.1	0.97	37.0	-4087	328.0	43	Della Vedova and Pellis (1992)
12I	35.81	18.44	37.1	0.98	36.4	-4085	332.0	42	Della Vedova and Pellis (1992)
13I	35.80	18.47	35.1	1.01	35.5	-4084	333.0	41	Della Vedova and Pellis (1992)
14I	35.80	18.47	34.4	0.98	33.7	-4081	336.0	39	Della Vedova and Pellis

									(1992)
15I	35.78	18.50	32.4	0.95	30.8	-4079	346.0	36	Della Vedova and Pellis (1992)
16I	35.78	18.52	35.4	0.96	34.0	-4079	371.0	40	Della Vedova and Pellis (1992)
17I	35.76	18.54	37.4	0.97	36.3	-4073	357.0	42	Della Vedova and Pellis (1992)
18I	35.74	18.56	36.6	0.98	35.9	-4070	355.0	42	Della Vedova and Pellis (1992)
19I	35.77	18.31	25.8	0.97	25	-4085	345.0	30	Della Vedova and Pellis (1992)
20I	35.57	17.90	50.7	0.83	42.1	-3963	427.0	49	Erickson et al. (1977)
21I	35.51	16.94	37.1	1.05	39	-3980	220.0	44	Della Vedova and Pellis (1992)
22I	35.46	17.32	33.3	1.05	35	-3950	328.0	41	Della Vedova and Pellis (1992)
23I	35.44	17.16	41.4	1.09	45.1	-3890	315.0	51	Della Vedova and Pellis (1992)
24I	35.44	17.19	42.3	1.06	44.8	-3900	310.0	51	Della Vedova and Pellis (1992)
25I	35.44	17.21	45.8	1.08	49.5	-3890	330.0	56	Della Vedova and Pellis (1992)
26I	35.45	17.23	46.1	1.02	47.0	-3920	314.0	53	Della Vedova and Pellis (1992)
27I	35.45	17.31	42.6	1.04	44.3	-3942	318.0	50	Della Vedova and Pellis (1992)
28I	35.42	17.55	39.5	1.06	41.9	-3930	240.0	47	Della Vedova and Pellis (1992)
29I	35.41	17.60	41.5	1.04	43.2	-3921	319.0	49	Della Vedova and Pellis (1992)
30I	35.42	17.63	43.5	1.05	45.7	-3920	325.0	52	Della Vedova and Pellis (1992)
31I	35.39	18.12	36	0.99	35.6	-3875	345.0	41	Della Vedova and Pellis (1992)
32I	35.43	18.13	34.7	1.07	37.1	-3864	346.0	43	Della Vedova and Pellis (1992)
33I	33.95	19.22	33.6	1.03	34.6	-3889	221.0	40	Erickson et al. (1977)

The heat flow sites 3I and 33I are in the abyssal plain of the Ionian Basin where the oceanic lithosphere is present (Fig. 30 and Table 4). These thirty-one corrected heat flow data provide a median value of 41 mW m^{-2} and an interquartile range of 39-48 mW m^{-2}.

Even if the number of heat flow data in the Herodotus Basin is very low, the oceanic lithosphere of this basin provides a heat-flow median lightly smaller (36 mW m^{-2}) than that of the Ionian Basin.

In summary, the corrected heat flow values in the Eastern Mediterranean Sea are characteristically low, rather uniform and substantially lower than the average global heat flow value of the oceanic domains (Table 5). With only a few exceptions, heat flow values are uniformly low throughout the entire Eastern Mediterranean Sea. Significant deviations of individual heat flow values from the regional mean are believed to be due to localized environmental disturbances rather than to thermal disturbances in the crust or upper mantle.

Table 5 Average global heat flow values in oceanic domains as suggested by different authors.

Oceanic Heat Flow (mW m^{-2})	**Reference**
66 (>66.5 Ma)	Davies and Davies 2010
56.4 (>84 Ma)	Pollack et al., 1993
48 (>80 Ma)	Jaupart et al., 2007
65 (>65 Ma)	Pasquale et al., 2012

5. PHYSICAL PROPERTIES OF SEDIMENTS

This section deals with the physical properties of the EMS sediments which are required for the calculation of the seafloor water loaded depth (Section 6). They are fundamental to produce a curve of variation of the bulk sediment density as a function of depth below the seabed till the crustal basement. For this purpose, I used different methodologies. First, direct measurements of porosity and density from the Ocean Drilling Program (ODP) and the Deep Sea Drilling Program (DSDP) in the EMS were gathered and analysed. Data were treated under the assumption of an exponential decrease of porosity with depth due to the increase in compaction. Bulk density increases as it depends on the fluid in pore space and solid grains. A study of the sediment physical properties was conducted over data collected from ODP and DSDP. However, this method of analysis cannot be extended to large depth since it overestimates bulk density values but gives consistent results only for the shallowest part of the sedimentary sequence (up to 1 km). Therefore, a more precise and realistic stratigraphic study was undertaken where sediment bulk densities were obtained after converting seismic velocities for the deep sediment layers. Results complemented the observed and corrected bulk densities of the shallow penetrated layers.

5.1 Marine sediments

Sediments have wide variability in nature, origin and size and this is mainly due to specific events and processes such as lithology, weathering, erosion, transport, energy and human action. As for their origin, sediments can be classified into:

1- Clastic or eroded sediments (weathering of outcropping rocks and occasionally volcanic explosion), mechanically transported and deposited on the seafloor after settling through the water column.
2- Chemical sediments, such as carbonate, siliceous, ferriferous, manganiferous, aluminiferous, phosphate, carbon, bituminous, sulphurous.
3- Biologic or those derived from organisms.

Marine sediments are strongly related to the history, tectonism, biology and hydrology of oceans and seas. They provide information regarding processes such as ocean widening, deepening and opening of new paths for surface and deep-water circulation and consequently for distribution of water masses and nutrients supply. They particularly explain events such as plate tectonics and climatic change. Several factors (morphology and geological structure of oceans and continents, weathering and erosion conditions on the continents, volcanism, transport through runoff, winds and currents, chemistry of water masses and pattern of oceanic mass circulation) influence the composition, fluxes and distribution of sediments in the ocean (Fig. 31).

Marine sediments do not only cover the seabed in coastal areas but also the deeper waters. Offshore oceanic expeditions identified their presence. Different sediment types were determined using cores and deep boreholes; in fact, the Eastern Mediterranean Sea was subject to many scientific drilling expeditions, the Ocean Drilling Program (ODP) and Deep Sea Drilling Project (DSDP). Drilling locations are selected based on the interpretation of marine seismic data indicating sediment thickness, structure and geometry.
The implementation of new geophysical methods of exploration revealed many petrophysical parameters of sediments. Geophysical and geodynamical models of oceanic basins creation and plates or microplates motions are based on using correct values of such parameters.

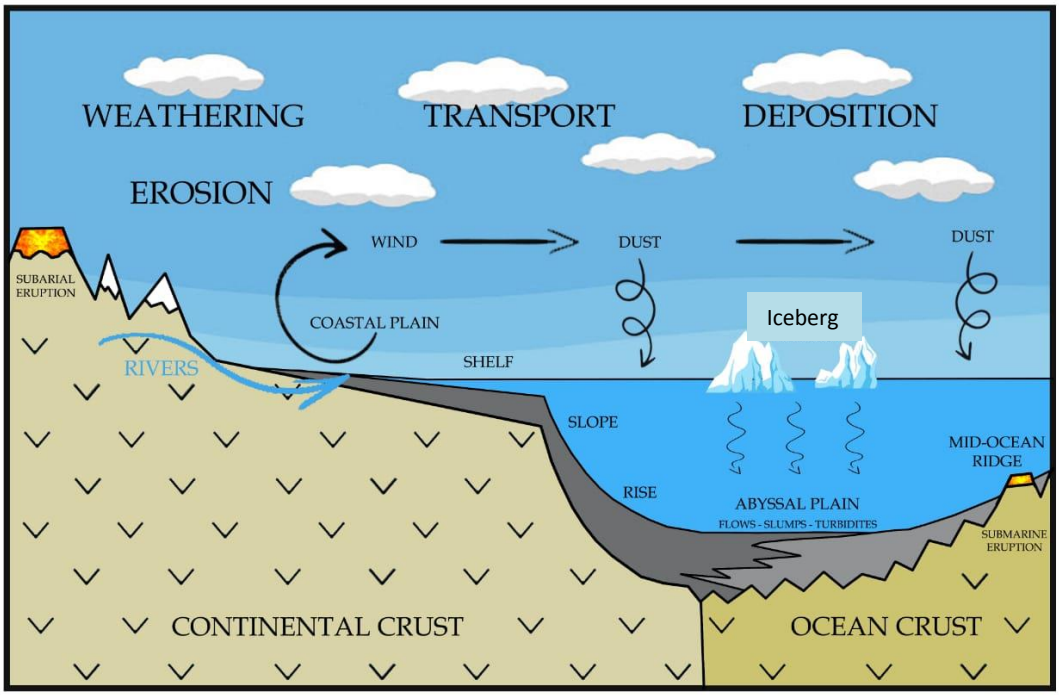

Fig. 31 Sediment distribution systems to the ocean including major influencing factors.

5.1.1 Classification of deep-sea sediments

A macroscopic description of sediments composition provides a distinction of silico-clastic (terrigenous), volcano-clastic (lithic fragments, glass, pumice), pelagic (diatom, foraminifer, radiolarian, etc.) and neritic (shells, oolith, etc.) or authigenic particles of mixt origin and derived from water (Mazzullo and Graham, 1988). Major volumes of sediments on the ocean floor are constituted of clay, sand and carbonate, and evaporite. Jones (1999) distributed deep-sea sediments into several categories. Such a distribution considers sediment chemical composition, and the mechanism of transport and deposition.

1. Pelagic oozes: fine sediments which accumulate after settling of microscopic, calcareous or siliceous shells of phytoplankton or zooplankton or clay-size

siliciclastic sediment or a mixture of these two. Meteoric extra-terrestrial dust, volcanic ash and terrigenous debris may be found within pelagic sediments. In marine sediments, ooze refers to sediment composition consisting of a far-land accumulation of about 30% of calcareous or siliceous planktonic skeletal debris from the overlying water column and the rest is of clay minerals. Oozes are classified according to their mineralogy (calcareous, siliceous) when the biogenic debris are not identifiable otherwise, they are replaced by the dominant composing organism (diatom, coccolith, foraminifera, globigerina, pteropod and radiolarian). Calcareous globigerina ooze composed of foraminiferal genus covers about half of the world's ocean floor. This ooze accumulates at depths shallower than the carbonate compensation depth (CCD) due to the rapid dissolution of calcium carbonate $CaCO_3$ in seawater. With lower occurrence, are found Siliceous ooze such as siliceous radiolarian and diatoms which instead accumulate at depths higher than the CCD. Finally, pelagic clay covers about 38% of the ocean floor and accumulates after a slow settling of sediment, remaining after the dissolution of calcareous and siliceous biogenic elements. Their colour varies between brown and red based on the oxidation state.

2. Turbidites: they result from rapid deposition of dense sediment within the bottom gravity flow or turbidity current. This current allows the distribution of clastic sediments into the deep ocean below the continental shelf. Once in the rest station, coarser material such as sand will settle first followed by mud and other finer particles. Turbidites sequences have strong reverberant echoes.
3. Contourites: they result from the deposition on the continental rise to lower slope domains of sand to clay-sized sediments. They are produced from contour-following geostrophic currents influenced by wind or tidal forces and thermohaline deepwater bottom currents. Thus, contourites geomorphology depends mainly on current velocity in addition to sediment supply and seafloor topography. Contourites reflectors indicate non-uniform accumulation.
4. Volcanogenic sediments originate from either terrestrial or underwater volcanic eruptions. They can be solid and detrital or chemical.
5. Glaciomarine sediments are composed of organic and inorganic components deposited by floating ice and marine-related processes.

In deep sequences, sediments have consolidated forms and two main accumulations are to be considered:

1. Marine evaporites are sedimentary rocks formed by chemical sediments after concentration and crystallization by evaporation. They are composed of calcite, halite, gypsum and other representative minerals after desiccation events such as the Miocene salt of the Mediterranean during the Messinian salinity crisis.
2. Black shales are found in deep-sea cretaceous sequences and have a high degree of organic carbon and form under oxygen-poor conditions. They consist of a mixture of clay minerals, quartz silt, organic particles and kerogen (Schieber, 1978).

Different from deep-sea sediments, terrigenous sediments may be found within the continental margins. They result from the weathering of rocks exposed at the Earth's surface and transported to the ocean by rivers, wind and ice with a redistribution due to oceanic currents (Hemming, 2007). Murray and Renard (1891) from the results of the Challenger Expedition highlighted the dominance of clastic muds near the continents and the presence of biogenic calcareous (foraminifer and nannofossil) and siliceous (radiolarian and diatom) oozes in most of the pelagic realm.
In addition to the previously mentioned sediments categories, further classifications exist and describe more precisely the sediment. For example, the ODP standard classification checks the core visual description and smear slide estimation to define lithologic units and formation. The actual ODP classification is based on three endmembers (biogenic siliceous, biogenic calcareous and terrigenous siliciclastic), the texture (size) of siliciclastic sediments (clay, silt, and sand-sized grains) and the degree of induration.

Table 6 Sediment classification and naming based on ODP standards.

Clay (%)	Nannofossil (%)	Name of sediment
0 – 25	100 – 75	Nannofossil ooze
25 – 50	75 – 50	Clayey nannofossil ooze
50 – 75	50 – 25	Nannofossil clay
75 – 100	25 – 0	Clay

Table 6 shows that nannofossil ooze is pelagic sediment, clayey nannofossil ooze and nannofossil clay are hemipelagic sediments and clay is terrigenous.
From a diagenesis degree point of view, a naming convention exists where soft sediments are named ooze or mud, firm sediments are chalk and hard sediments are designated by adding the suffix "stone" (limestone) or "ite" (radiolarite).

5.1.2 Distribution

Drilling sites were used for reconstructing the history of the ocean. They showed typical sequences where the oldest deposits are mainly siliciclastic in nature containing relatively high proportions of organic matter. They usually grade upwards, abruptly or progressively, to hemipelagic and sometimes to pelagic biogenic sediments.
Generally, sediment thickness increases greatly towards the continental margins and sediments thicken almost symmetrically far from ridge axis domains. Crustal age and distance from the continents are the two main factors that affect sediment distribution: in the Atlantic Ocean, sediment thickness varies between 100 m in the ridge zone and more than 6 km near the continental margins. A thin pelagic sediment layer near the Mid-Atlantic Ridge indicates a young lithosphere. Sediments settling and accumulation are a function of terrain slopes. Gentle slopes will permit a conformable settlement over the basement. Instead, rugged terrains, sliding and gravity flow

currents create flat-bottomed sediments ponds. In the South-Easternmost part of the Mediterranean, the Nile River is one of the major sources of sediments and has delivered sediments to coastal zones and deeper abyssal plains of the Central and Eastern Mediterranean Sea.

5.1.3 Mineralogy

Among the different characteristics of rocks and sediments, physical properties are strong indicators of composition, formation and environmental conditions of the deposits. Offshore drilling and core logging (geophysical measurements) offer the possibility of a rapid and high spatial resolution control of physical properties. The quantitative resulting data are generally well-defined allowing, after their analysis, to interpret and constrain the complex mineralogical and fluid systems in rocks and sediments. In soft and semi-consolidated sediments, data appear as proxies for sediment composition controlled by origin, depositional and erosional processes, oceanographic and climatic changes, and post-depositional processes such as consolidation and early diagenesis. On the other hand, in consolidated sediments and igneous rocks, diagenetic processes, including cementation, major lithological changes, and major faults, tend to dominate many physical properties. Adding to this, hydrothermal circulation in the sedimentary and rocky environment can be evidenced through physical measurements.

When dealing with applied engineering such as soil mechanics and geology, the physical and mechanical properties of sediments have central importance. In marine sediments, it is fundamental to account for interactions and interrelationships between the different components of the whole sediment including solid minerals and fluid or gaseous pore filling (Fig. 32).

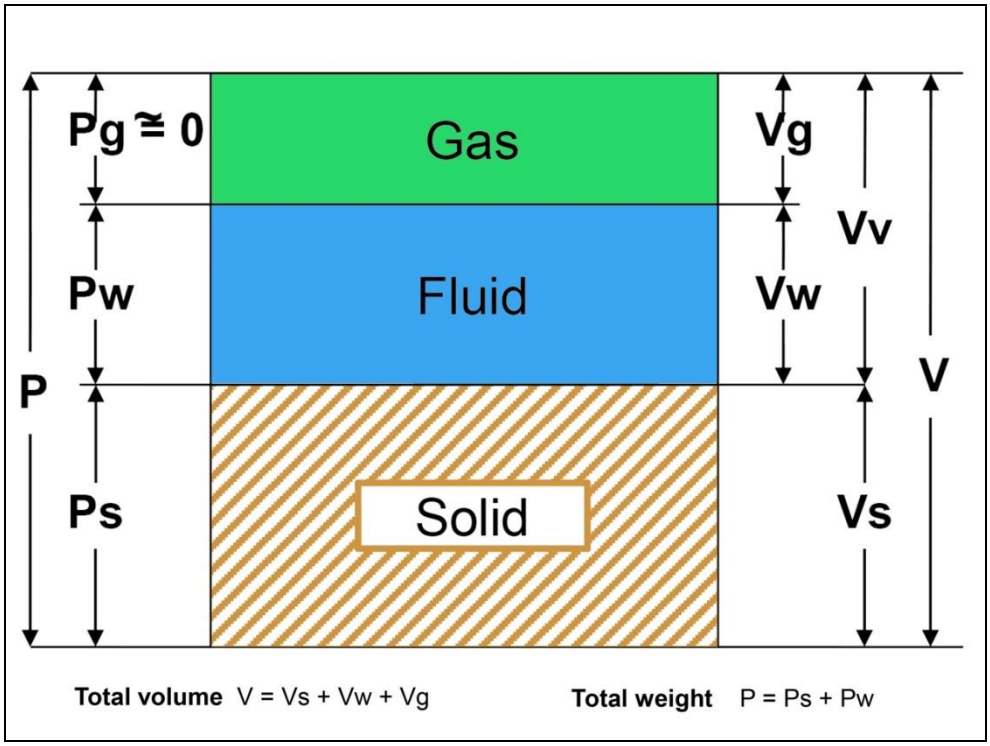

Fig. 32 Possible physical states of the different components of sediment.

Large amounts of marine sediments physical properties were made available through drilling and coring the bottoms of oceans and seas. Those include bulk density, water content, porosity, permeability, plasticity, compressional wave velocities and thermal conductivity. Shear strength and consolidation allow predicting the bearing capacity of the seafloor under a given applied load and its resistance to penetration. In this domain, an important factor is the density of the material defined as the mass per unit volume of that material measured in kilograms per cubic meter ($kg.m^{-3}$) in SI units. Sediment density depends mainly on its composition (Table 7). The density of a sediment sample may be calculated by adding a known weight of dry sediment to a known volume of water. The volume change is measured and it is the volume of the sediment. The sediment mass (=weight/acceleration of gravity) divided by its volume is the density.

Table 7 Density of common mineral sediments in coastal and deep water areas.

Sediments, minerals and ores	**Density ($kg.m^{-3}$)**
Sand, dry	1400 – 1650
Coal, anthracite	1300 – 1800
Dolomite	2300 – 2900
Salt	2100 – 2600
Shale	2000 – 2700
Andesite	2400 – 2800
Gneiss	2600 – 3000
Peridotite	2800 – 3200
Slate	2600 – 2800
Barite	4300 – 4700
Galena	7400 – 7600

Magnetite ore	4900 – 5300
Sphalerite	3500 – 4000
Clay	1500 – 2600
Sand, saturated	1900 – 2100
Chalk	1900 – 2500
Coal, lignite	1100 – 1500
Limestone	2000 – 2700
Sandstone	2000 – 2600
Quartz	2648
Feldspar	2560 – 2650
Illite	2660
Montmorillonite	2608
Kaolinite	2594
Calcite	2716
Aragonite	2931
Radiolarian ooze	2270
Diatomaceous ooze	2420
Terrigenous sediments	2760
Calcareous ooze	2650
Deep sea pelagic clay	2730
Chalcopyrite	4100 – 4300
Haematite ore	4900 – 5300
Pyrite	4900 – 5200
Igneous and metamorphic	
Basalt	2700 – 3000
Granite	2500 – 2800
Quartzite	2600 – 2700
Other	
Water	1000 – 1050
Oil	600 – 900

5.2 Porosity and density change with depth

Density and porosity vary with increasing depth in marine sediments and rocks. Such variations may explain the results of some important geophysical measurements and geological processes (gravity, diagenesis…). Profiles of porosity variation with depth can help in computing the original quantity of sediments that have been subject to overburden compression till reaching the actual thickness.

Different physical and chemical processes contribute to sediment compaction. Plastic deformation such as grains compression, squash, redistribution and other deformational events are examples of such physical events. Whereas minerals dissolution and resettlement are examples of chemical processes. Compaction of various types of sediment (clay, chalk, mudstone…) will not be similar since the sedimentary matrix will react differently. Porosity φ indicates the degree of compaction of material. It decreases exponentially with increasing burial depth. Such relation and dependence derive from basic principles of soil mechanics which was traduced by Ruby and Hubbert (1960) through the relation

$$\sigma = s - P_f \quad (5.1)$$

where σ represents the effective stress or load on the material, s the overburden stress (a stratum being buried under an increasing load of sediments) and P_f is the fluid pressure. This means that the support of the total overburden stress is divided between σ and P_f.

The effective stress or pressure can be easily determined by subtracting the density of pore water from the mean saturated bulk density of the sediments and then multiplying it by depth in the sediments.

The total vertically (sediment column from sea-bottom surface z=0 to a depth z) exerted overburden stress s will be physically and mathematically expressed by the relation:

$$s = \int_0^z [\rho_w \, g \, \varphi + \rho_{sg} g \, (1-\varphi)] \, dz = \rho_b \, g \, z \quad (5.2)$$

where ρ_b is the mean value of the water-saturated bulk density of the overlying materials, g the acceleration due to gravity, φ the porosity and ρ_w and ρ_{sg} the pore-water and grain densities respectively.

On the other hand, the fluid pressure P_f is given by

$$P_f = \lambda \, s = \lambda \, \rho_b \, g \, z \quad (5.3)$$

with λ being the ratio of fluid pressure to overburden pressure (known as proportionality parameter) expressed by $\lambda = \frac{\rho_w}{\rho_b}$ .By substitution

$$\sigma = (1 - \lambda) \, \rho_b \, g \, z \quad (5.4)$$

(5.2.4)

Overburden pressure creating the decrease of sediments volume with depth in sediments derives only from the submerged weight of mineral grains and is independent of water depth. Mechanically speaking, sediments compaction is a process during which water is expelled from voids until λ reaches the lowest limit compatible with the hydrostatic column. In other terms, λ varies (Sclater and Christie, 1980) between 0 (zero pressure) and 1 (water pressure equal to the entire weight per unit area of the overburden). When the pore pressure is essentially hydrostatic, and it is the case of almost all sea floor sediments (Hamilton, 1976), the fluid pressure becomes:

$$P_f = \rho_w \, g \, z \quad (5.5)$$

and

$$\sigma = (\rho_b - \rho_w)\, g\, z \qquad (5.6)$$

Under normal pressures, porosity φ would decrease exponentially with depth following the relation (Ruby and Hubbert, 1960; Sclater and Christie, 1980):

$$\varphi(z) = \varphi_0\, e^{-cz} \qquad (5.7)$$

where φ_0 is the surface porosity and c is the compaction depth constant (m^{-1}) that quantifies the rate of porosity diminution with depth.
By substitution, it is possible to express the change of porosity as a function of the effective stress with the relation:

$$\varphi(\sigma) = \varphi_0\, e^{\frac{-c\sigma}{(\rho_b - \rho_w)g}} \qquad (5.8)$$

For our area of study, porosity and density values were made available using ODP and DSDP data of cored sediments and rocks.

Table 8 ODP and DSDP sites used in the study area and some related parameters.

Drilling project and Leg	**Site and Hole**	**Location**	**Lat. N**	**Long. E**	**Water depth (m)**	**Penetration (m)**	**Age at base of the hole (Ma)**
ODP Leg160	964A	Foot of the Calabrian Ridge (near the Ionian abyssal plain)	36°15.623'N	17°44.990'E	3657.7	101.8	3.85 (Middle Pliocene)
ODP Leg160	965A	Fault-controlled upper northern slope of ESM	33°55.080'N	32°42.785'E	1506.6	250.4	3.85 (Middle Pliocene)
ODP Leg160	966A	Fault-bounded northern margin of the ESM plateau area	33°47.799'N	32°42.095'E	926.6	106.8	4.52 (Early Pliocene)
ODP Leg160	967A	Small ridge near the foot of the northern slope of the ESM	34° 4.098'N	32°43.523'E	2553	141.3	5.1 (Early Pliocene)
ODP Leg160	967E	Small ridge near the foot of the northern slope of the ESM	34° 4.106'N	32°43.525'E	2552.7	600.3	Middle Eocene
ODP Leg160	968A	Crest of a small ridge in a southward direction from Cyprus slope base	34°19.900'N	32°45.065'E	1961	302.7	3.57 (Middle Pliocene)
ODP Leg160	969A	Mediterranean Ridge	33°50.399'N	24°53.065'E	2200.3	108.3	5.1 (Early Pliocene)
ODP Leg160	970A	Northern part of the Mediterranean Ridge (150km South of Crete) Milano Mud volcano	33°44.194'N	24°48.120'E	2075.5	200	1.75 (Late Pliocene)
ODP Leg160	970B	Distal part from the Mud volcano (600 m away from the volcano)	33°44.214'N	24°48.694'E	2078.6	50	Early Plesitocene
ODP Leg160	970C	Upper flank of the mud volcano	33°44.134'N	24°47.457'E	2036.9	50	Not defined
ODP Leg160	970D	Crestal area of the mud volcano	33°44.042'N	24°46.613'E	1953.3	30	Not defined
ODP Leg160	971A	Margin of the Napoli mud volcano	33°42.190'N	24°42.814'E	2026.1	105.9	Middle Pliocene
ODP Leg160	971B	Moat of the Napoli mud volcano	33°42.817'N	24°42.108'E	2140.9	203.5	Late Pleistocene
ODP Leg160	971D	Mud volcano crestal area	33°43.437'N	24°41.276'E	1933.1	46	Middle Miocene
ODP Leg160	971E	Mud volcano crestal area	33°43.621'N	24°40.839'E	1943.6	28.5	Miocene

ODP Leg160	972A	Small high on the lower slope of the Hellenic accretionary prism	35°46.797'N	18°43.515'E	3930.6	95.4	Late Pliocene
ODP Leg160	973A	Broad high slightly higher on the slope relative to site 972	35°46.820'N	18°56.889'E	3695	148.5	1.75 (Late Pliocene)
DSDP Leg 13	125	Mediterranean Ridge Central Ionian Basin	34°37.488'N	20°25.758'E	2782	97	4.2 (Early Pliocene)
DSDP Leg 13	125A	Mediterranean Ridge Central Ionian Basin	34°37.488'N	20°25.758'E	2782	121	7.75 (Early Miocene)
DSDP Leg 13	126	Near the axis of a deep cleft in the Mediterranean Ridge, the Ionian basin	35° 9.720'N	21°25.632'E	3730	129.4	13.25 (Middle Miocene)
DSDP Leg 13	127	Inner wall of the Hellenic Trench	35°43.902'N	22°29.808'E	4654	437	2.6 (Late Pliocene)
DSDP Leg 13	127A	Hellenic Trench floor	35°43.902'N	22°29.808'E	4636	80	0.9 (Pleistocene)
DSDP Leg 13	128	Near the seaward edge of the trench floor	35°42.582'N	22°28.098'E	4640	480	1.5 (Early Pleistocene)
DSDP Leg 13	130	On the Mediterranean Ridge North of Herodotus Abyssal Plain	33°36.312'N	27°51.990'E	2979	563	0.9 (Early Pleistocene)
DSDP Leg 13	131	Distal part of western Nile Cone in the Levantine Basin	33° 6.390'N	28°30.690'E	3035	49	0.9 (Early Pleistocene)
DSDP Leg 13	131A	Distal part of western Nile Cone in the Levantine Basin	33° 6.390'N	28°30.690'E	3037	272	0.9 (Early Pleistocene)
DSDP Leg 42	374	Central Messina Abyssal Plain	35°50.868'N	18°11.778'E	4078	457	7.75 (Late Miocene)
DSDP Leg 42	376	Antalya Basin flank of the Florence Rise - West of Cyprus	34°52.320'N	31°48.450'E	2101	216.5	7.75 (Late Miocene)
DSDP Leg 42	377	Cleft on the Mediterranean Ridge	35° 9.702'N	21°25.860'E	3718	263	13.25 (Middle Miocene)

Table 8 lists data from the holes that have reliable values to estimate φ_0 and λ (compaction decay length scale, $\lambda=1/c$) for the cored and sampled sediments. In the present analysis, a basin distribution methodology was adopted. The studied area was divided into 3 main basins: Ionian Basin (Western Mediterranean Ridge), Herodotus Basin (Eastern Mediterranean Ridge included) and Levantine Basin. This division followed the distribution of boreholes and their concentrations within the study area as shown in figure 33. The total available data for porosity variation with depth is 875 values. Sediments were distinguished based on a lithological classification from ODP reports (Kastens et al., 1987) and were grouped into three main categories: pelagic, terrigenous and evaporites. To better account for porosity values obtained during shipboard surveys, it is necessary to correct for the rebound effect. This effect is nothing but the increase in volume or elastic rebound due to removal of overburden sediments pressure. Hamilton (1959) considered the effect of sediment consolidation and thus the reduction of porosity in sediment (or increase in density) being under pressure either in laboratory conditions or in thick strata of deep-sea sediments. Then Hamilton (1976) constructed in situ profiles of porosity and density versus depth for oozes, pelagic clay and terrigenous sediments using results of consolidation tests on samples from the Deep Sea Drilling Project (DSDP) to estimate the amount of elastic rebound. To perform a consolidation test, a water-saturated sediment sample should be placed within a cylinder and then larger loads or pressures that would cause water to drain from the cylinder.

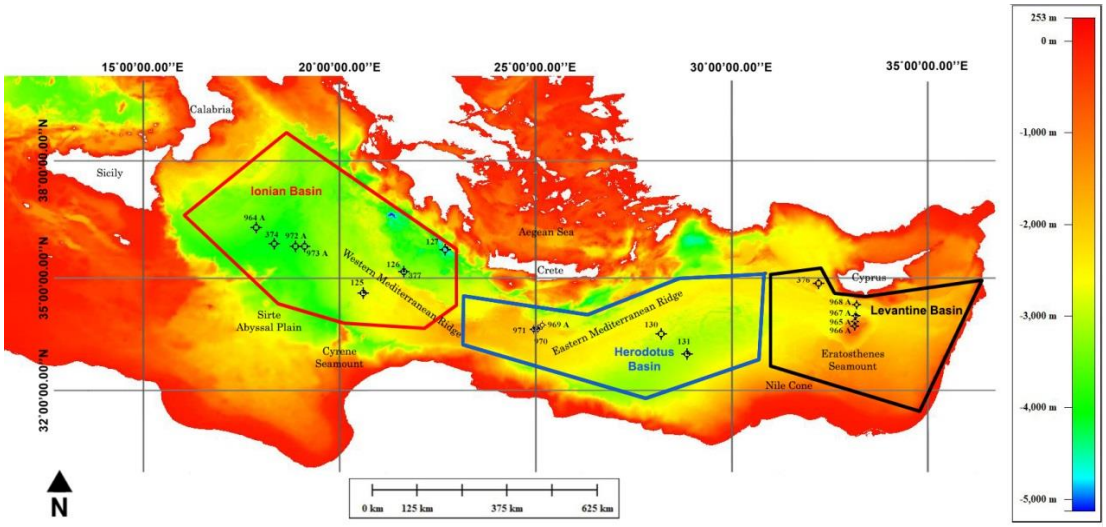

Fig. 33 Bahymetric map of the study area showing the distribution of ODP, DSDP (black stars) and ESP sites (black inversed triangles) used in this study.

Rebound or increase in volume is obtained by removing pressure at any desired depth. Calcareous ooze is the type of sediment that is frequently present in high depths of the seafloor below the calcite compensation depth. Pelagic clay can be both seafloor sediment and deep sediment where calcareous sediment cannot accumulate. Pelagic sediments have a lower percentage of calcium carbonate (< 30%) than calcareous sediments. Whereas siliceous marine sediments contain more than 30% silica and less than 30% calcium carbonate. Instead, terrigenous sediments (sand, silt, clay) are those having land origins. They accumulate over the continental shelf and slope zones and reach the abyssal plains through deep-sea fans and canyons. We recalculated and plotted (Fig. 34) the regression equations for the rebound in porosity using the same data from Hamilton (1976) for deep-sea pelagic and terrigenous sediments. Equations were constrained to zero since at the very shallow sediment surface the overburden pressure is null as well as rebound.

The newly obtained regression equations were used to estimate the rebound in porosity of our dataset and to calculate a corrected in situ porosity versus depth by subtracting the estimated rebound in porosity from laboratory porosity. Rebound in porosity increases with depth and is only valid to a given depth after which the regression equation is not valid anymore. This was explained by Hamilton, for terrigenous sediments, through the fact that at lower sediment depths, rocks formed from lithified sediments usually rebound less than unconsolidated sediments at the same depth. Below 600 m depth (end of the curve), sediment may be then transformed into a mudstone. Pelagic curve ends at 500 m since lithification of calcareous sediments into limestone occurs at shallow depth after which porosity will hardly vary. Such depths are expected for unconsolidated sediments. Since our ODP and DSDP depth values are like those used by Hamilton, regression curves were considered valid.

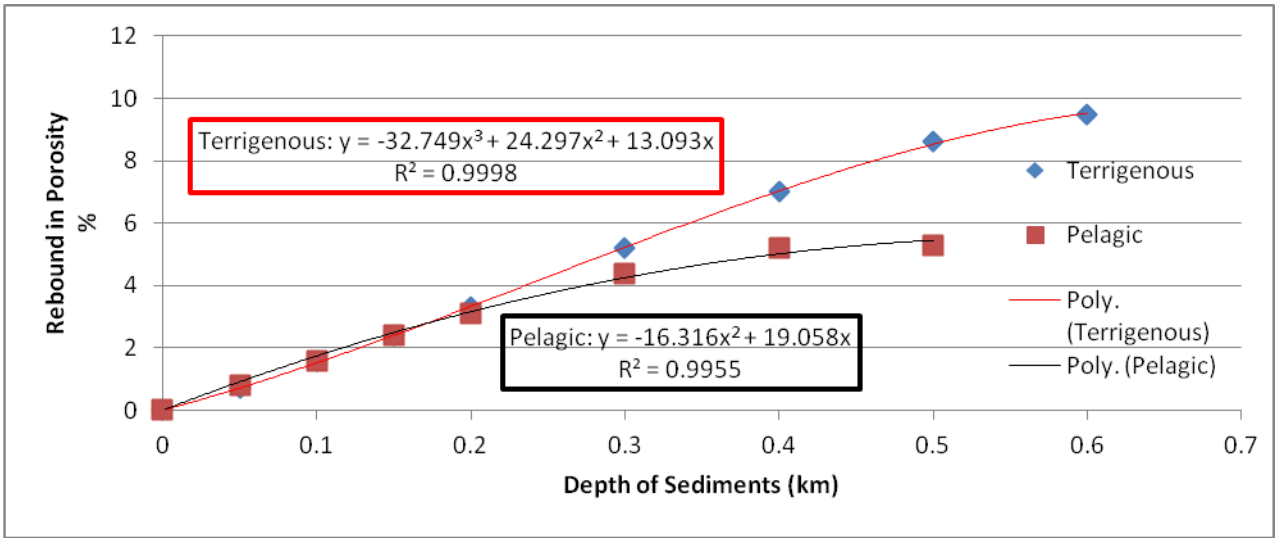

Fig. 34 Curves of the rebound in porosity variation with depth for terrigenous and pelagic sediments.

When passing from borehole to laboratory, porosity will increase and consequently density will decrease. In situ bulk density for all used ODP and DSDP sites was calculated from in situ porosity values using the relation between bulk density and porosity with depth:

$$\rho_s(z) = \rho_w\ \varphi(z) + \rho_{sg}[1- \varphi(z)] \qquad (5.9)$$

and adopting ρ_w = 1030 kg m^{-3} as pore-water density and appropriate drilling core values of grain density ρ_{sg} for each depth "z". Figures 35 and 36 show the difference between porosity and bulk density values measured in the laboratory and those corrected for rebound and thus reduced to in situ conditions for core samples from ODP leg 160 site 968A.

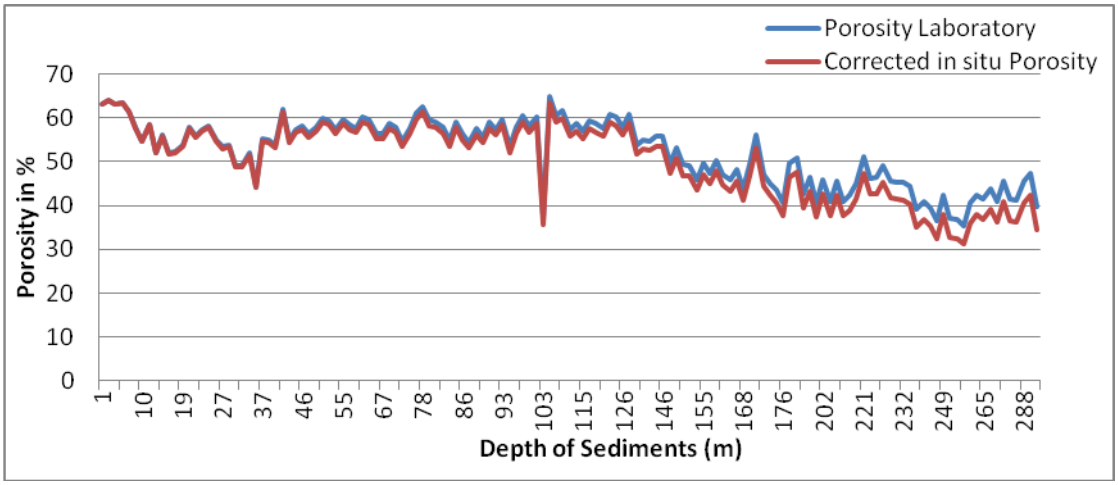

Fig. 35 Difference between laboratory porosity and in situ porosity variation with depth in sediments for ODP leg 160 site 968 A.

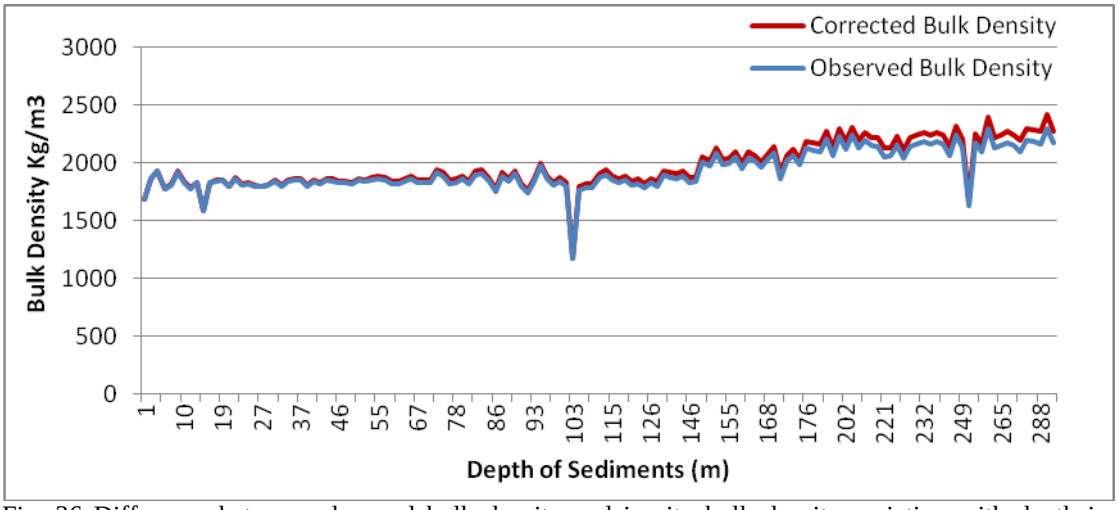

Fig. 36 Difference between observed bulk density and in situ bulk density variation with depth in sediments for ODP leg 160 site 968 A.

Moreover, density and porosity measurements from ODP and DSDP may be affected by some errors (small amount of core sample, disturbed samples, systematic errors, human errors, ecc.). In fact, after plotting ODP and DSDP porosity data in function of depth for the study area (Fig. 37) some irregular and abnormal values were noticed especially those of unexplained high porosity > 0.9 or very low porosity < 0.2 in shallow sediment depth.

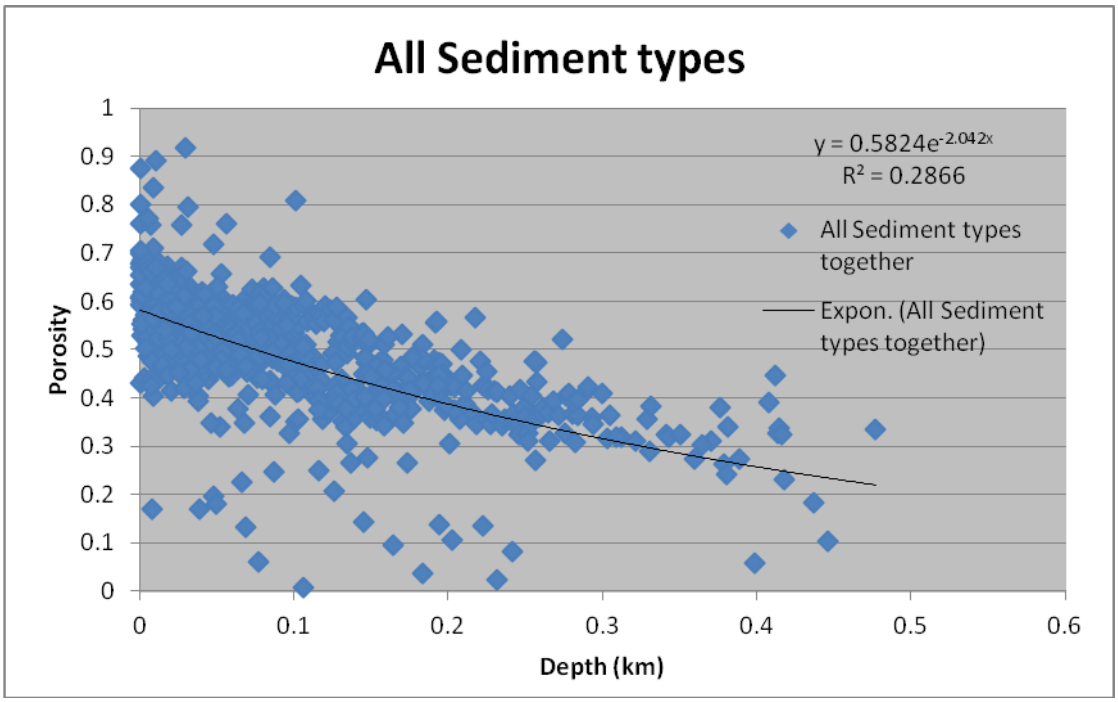

Fig. 37 Porosity corrected for rebound effect versus depth in sediments (all data).

Those irregularities caused a misfit of the tendency curve lowering the correlation factor (R= 0.535) and thus producing an inaccurate curve for the general trend of porosity with depth. Outliers were identified according to their corresponding ODP and DSDP locations. A very precise investigation of those outliers was conducted by re-evaluating data acquisition, processing reports and comparing datasets with

experimental curves to eliminate any possible erroneous values or doubtful and inconsistent ones.

Table 9 clearly shows that outliers are only observed in the Levantine and Herodotus Basins and not within the Ionian Basin. It was also noted after separating porosity datasets between pelagic and terrigenous that pelagic sediments data contained the largest number of outliers. Some absurd porosity values were corrected by replacing them with their corresponding graphical values. Other values were eliminated because of a lack of core samples recovery. In addition, unexplained very high- and low-porosity values, obtained for limited core sections along with the drill and not reflecting the general trend of porosity variations, were eliminated. Very low porosity value (<0.2) in shallow sediment depth (up to 200 m) cannot be explained by a simple compaction effect as well as very high porosity values (> 0.9) in some materials under 10 m of sediment cover. After filtering, the dataset was reduced to 855 porosity-depth values.

Table 9 Analysis of outliers of porosity values observed in some drilling sites (red values: filtered out – black values: corrected and updated)

Basin	Drilling Leg /Site	Sediment Category	Sediment depth (m)	Porosity	ODP reports interpretation	Decision
Levantine	160 – 965 A	Pelagic	7.8	0.17	Graphical porosity= 0.23	Filter out those measurements
			38.93	0.16	Owing to the poor core recovery between 29 and 250 mbsf (less than 5%) we can make only general statements for the recovered packstone/ grainstone/mudstone section: density is between 2.4 and 2.7 g/cm^3 and porosity is below 20%.	
			48.31	0.19		
			68.4	0.13		
			77.18	0.06		
			87.16	0.24		
			106.53	0.01		
			115.86	0.24		
			126.35	0.2		
			145.1	0.14		
			164	0.09		
			173.68	0.26		
			183.11	0.03		
			202.4	0.1		
			222.4	0.13		
			231.99	0.02		
			241.73	0.08		
	160 – 966		65.82	0.22	From graph GD=2.9 and	Use graphical

	A				Porosity = 52	porosity value
	160 – 967 A		29.68	0.91	Porosity=0.7 and GD=3	Use graphical porosity value
	160 – 967 E		148.01	0.27	Well lithified nannofossil chalk	Use this value
			256.48	0.26	Coherent with graphical value	Accept those values
			330.98	0.28	Coherent with graphical value	
			359.94	0.27	Coherent with graphical value	
			379.21	0.26	Changes in the composition and texture of the sediments sequence boundaries or changes in the sedimentary environment	Accept those values
			380.57	0.24		
			388.88	0.27		
			398.5	0.05		Filter out
			417.68	0.22		Accept this value
			436.6	0.18		Filter out
			446.36	0.1		
Herodotus	160 – 971 A	Pelagic	9	0.83	GD=2.25 and BD=1.4	Accept this value
	160 – 971 B	Pelagic	0.45	0.87	Variations in clast content, lithology and size are likely first-order controls on the index properties. GD=2 and BD=1.5 GD=2.3 and BD=1.2	Accept this values
			10.64	0.89		Filter out
	160 – 971 A	Terrigenous	100.72	0.80	GD=2 and BD=1.5	Accept this value
	160 – 971 B		49.81	0.18	GD=3.1 and BD=2.6	Filter out this value
			137.15	0.26	Correct values of GD and BD	Accept this value
			194.29	0.13	Correct values of GD and BD	Filter out this value

After removing outliers and plotting again porosity variation in function of depth in sediments, figure 38 shows a better-correlated curve of porosity (correlation factor R= 0.745). Initial porosity value φ_0 (at depth z=0) equal to 0.58 was not changed and compaction depth constant decreased from 20.42×10^{-4} m^{-1} to 16.94×10^{-4} m^{-1} referring to a lower general compaction trend, more indicative to a regional study rather than to a particular local effect.

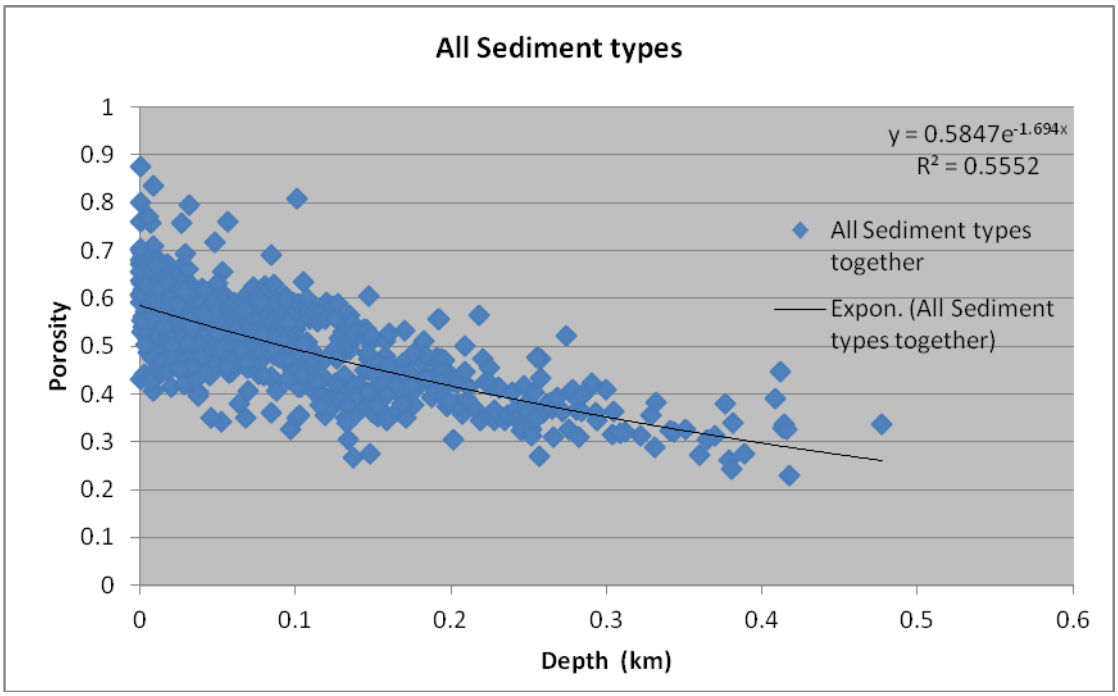

Fig. 38 Porosity corrected for rebound effect versus depth (without outliers).

The best correlation coefficient was found for pelagic sediments of the Levantine Basin. Values of φ_0 ranged between 0.532 and 0.63 and ρ_{sg} between 2695 and 2952 kg.m^{-3}. The mean grain sediment density ρ_{sg} was calculated for each basin – lithology and the total study area as shown in table 10. Some irregular and unexplained values of sediment grain density reaching even 10 g cm^{-3} were observed in the global database. Those were either eliminated or replaced by the corresponding graphical values.

Due to the lack of sampled evaporites in the study area since drillings did not manage to core and sample in the Messenian sequence, a different methodology was followed. Pasquale et al. (2006) studied the variation of evaporites porosity with sediment depth in the Southern Tyrrhenian Basin. Raw data from that study ranging between 240 m and 720 m sediment depth were provided and plotted together with only 7 evaporitic values found in the study area in sediment depth between 90 m and 120 m. Figure 39 shows that those 7 shallow values would follow the general trend of distribution of Pasquale et al. (2006) dataset extending to some additional hundreds of meters. Thus, it was assumed that the evaporitic sequence found in the Tyrrhenian Basin can be extended to the EMS Basins. However, the EMS basins have a thicker layer of evaporites not reached by coring unless in a few locations of vertical seismic logs, which will be better detailed in the next sections. To overcome the difficulty lying with the anomalous density of the Messinian evaporites, Schreiber et al. (1973) have measured density and velocity at intervals of higher confining pressure (up to 7 kilobars) on DSDP evaporitic samples (anhydrite, gypsum and halite) recovered during Leg 13 of the Deep Sea Drilling Project in the western Mediterranean. In

relation to evaporitic layer depth and compressional seismic wave, the density of the Messinian evaporites ranged between 2200 and 2400 kg.m^{-3}.

Table 10 Values of parameters appearing in the relation between porosity and sediment depth.

Area	**Lithology**	**Measurements counts**	φ_0	**c x 10^{-4} (m^{-1})**	**Correlation Coefficient**	ρ_{sg} **(kg.m^{-3})**
Levantine Basin	Terrigenous	145	0.58	15.58	0.749	2879 ± 299
	Pelagic	233	0.63	22.4	0.853	2952 ± 359
	Both	378	0.615	20.2	0.822	2923 ± 339
Herodotus Basin	Terrigenous	169	0.532	12.14	0.611	2822 ± 244
	Pelagic	180	0.593	16.18	0.696	2851 ± 221
	Both	349	0.562	13.71	0.582	2851 ± 217
Ionian Basin	Terrigenous	32	0.564	16.73	0.55	2695 ± 377
	Pelagic	114	0.572	13.31	0.757	2768 ± 286
	Both	146	0.569	13.7	0.701	2752 ± 308
All study area	Terrigenous	346	0.549	13.17	0.655	2834 ± 286
	Pelagic	527	0.605	18.94	0.796	2878 ± 311
	Both	873	0.584	16.94	0.745	2861 ± 302
	Evaporites (including Tyrrhenian)	114	0.606	16.29	0.852	2752 ± 88
	All Data	987	0.58	15.8	0.864	2848 ± 288
Hoggard et al., 2017			0.61	2.56		2650
Pasquale et al., 2006			0.71	15.62		2740

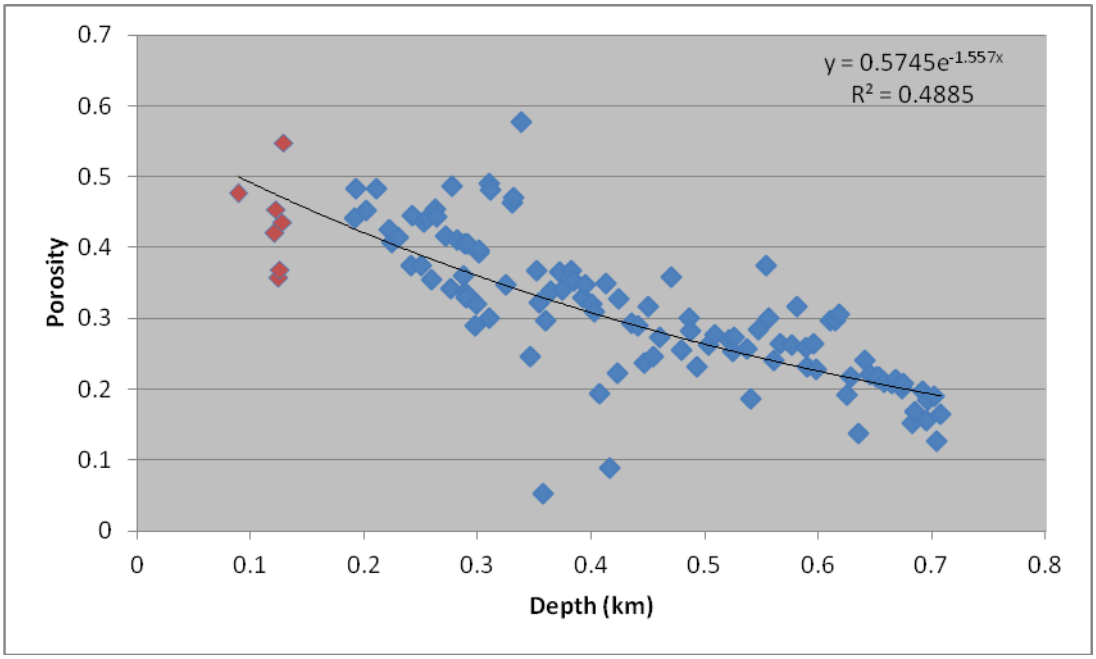

Fig. 39 Porosity corrected for rebound effect versus depth for evaporites. Blue: Porosity data for the southern Tyrrhenian after Pasquale et al. (2006). Red: Corrected porosity of Eastern Mediterranean Sea evaporites.

Assuming an exponential decrease of porosity as a function of depth, the bulk sedimentary density increases with compaction as it depends on the fluid in the pore space and the solid grains and the change within the sedimentary column is given by:

$$\rho_s = \rho_{sg} + \frac{\phi_o \lambda}{z}\left(\rho_w - \rho_{sg}\right)\left(1 - e^{\frac{-z}{\lambda}}\right) \qquad (5.10)$$

Where ϕ_0 is the initial sediment porosity and λ is the compaction decay length scale (Athy, 1930).

Variation curves of bulk sediment density as a function of sediment thickness were plotted for each lithology distribution in each considered basin. Curves were extended down to 12 km of sediment thickness, the limit before reaching the crust (Fig. 40). Two additional curves were plotted for comparison, the first one represents the bulk sediment density variation as a function of sediment thickness in the Southern Tyrrhenian after Pasquale et al. (2007) and a general oceanic one after Hoggard et al. (2017). To obtain bulk density values of sedimentary columns in given locations, Hoggard 2017 took into consideration the compaction within the sedimentary pile and combined the velocity model used by Winterbourne et al., 2009 converting seismic profiles two-way travel time into thickness, and the Wyllie et al. 1956 empirical function of porosity change with depth. Hoggard assumed the solid grain to be a mixture of quartz and clay (2650 $\pm$ 0.05 Kg m^{-3}, Christensen, 1982). Hoggard et al. (2017) in their global modelling collected seismic databases from around the world including the Eastern Mediterranean Sea. From intersections between seismic

reflection and refraction profiles, they calibrated the velocity model and determined optimal global values of ϕ_0 and λ (0.61 and 3.9 km respectively). However, Pasquale et al. (2005) through an isostatic study in the Southern Tyrrhenian, where a thick sediment layer of evaporites exists, found specific values for the two previous parameters. They used a ϕ_0 equal to 0.71 and a porosity rate with depth "c" equal to 15.66 x 10^{-4} m^{-1}. λ being the inverse of c, a value of 0.64 km is obtained.

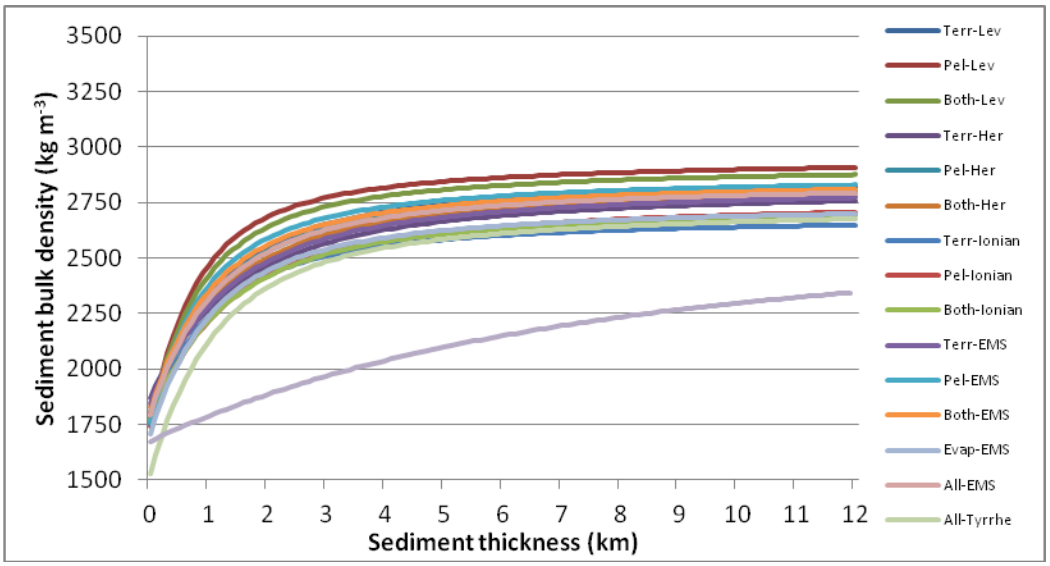

Fig. 40 Variation curves of bulk sediment density as a function of sediment thickness for different adopted lithological and basins distribution. Lev: Levantine, Her: Herodotus, EMS: Eastern Mediterranean Sea, Tyrrhe: Tyrrhenian, All: all sediment types, Pel: Pelagic, Terr: Terrigenous.

Figure 40 clearly shows that curves of bulk density variation with sediment thickness for terrigenous, pelagic and evaporitic sediments in the Ionian, Herodotus and Levantine Basins follow the same trend. It can be noted that the curve corresponding to "All data" may be very well representative of all basins. It is also clear that the curve after Pasquale et al. (2007) has the same trend of variation with the only difference of having lower values of grain density reducing values of bulk density.
A major difference can be observed for the curve obtained after Hoggard 2017. This global curve, which includes the Mediterranean Sea, cannot be representative of the EMS and thus cannot be adopted for further detailed calculations of sediment corrections and residual depths in the EMS. Hoggard, 2017 used global datasets of seismic surveys from areas located on the oceanic crust (including the Mediterranean) characterized by sediments with lower densities than those from the Mediterranean and an optimal compaction decay length scale much higher than the one corresponding to the Mediterranean.

5.2.1 Validity of the bulk density variation curve

The density-depth curve obtained in section 5.2 is very well representative of the Plio-Quaternary and Messinian sediments up to 1 km of sediment thickness. To check the validity of its extension into deeper older sediment layers, it is necessary to use

correct values of sediment densities and related parameters and compare them with what would be obtained through the variation curve based on Athy, 1930.

5.3 Relation between seismic velocities and sediment thickness

Compressional waves undergo attenuation when traveling through oceanic sediments. This attenuation will depend on sediment bulk density, porosity, shear strength and consolidation. Compressional wave velocities gradually increase with sediment thickness as it was observed in many seismic refraction profiles. Nafe and Drake (1957) deduced the following relation:

$V_p=0.43d + 1.83$

Where d is the depth in kilometres below the seafloor and V_p is the seismic velocity in km/s. From an acoustic point of view and considering the fact of oblique reflections in shallow sedimentary sequences, Officer (1955) deduced the following relation:

$V_p=1.5\sqrt{(1 + 1.37d)}$

Another relation was obtained by Laughton (1957) from laboratory testing conducted on cores of globigerina ooze with different compaction degrees:

$V_p=0.44\sqrt{d} + 1.65$

Compressional wave velocities range between 1.5 km/s for seawater and 3.5 km/s for deep compacted sediments. Higher sediment compaction and lithification, thus higher sediment density value will result in higher compressional velocity values. Seismic velocity anisotropy is observed in many situations such as:

1. Lithological variations where vertical and horizontal P-waves velocities vary when passing through different sediment layers. For example, variation is about 20 % between terrigenous muds and pelagic clays (Laughton, 1957).
2. Sediment thickness where higher overburden level increases transverse anisotropy due to more pronounced mineral grains orientation.
3. Physical and morphological state such as cementation and recrystallization of deep-sea calcareous sediments presenting P-wave and S-wave anisotropy.

5.3.1 Seismic velocity and density of marine sediments and rocks

When dealing with underwater acoustics and wave propagation into sediments under the seabed, it is necessary to understand the effect of the medium where propagation occurs. It should be also taken into consideration the relation which exists between acoustic wave velocity and material density and impedance. Therefore, if seismic velocity is measured and known, one can determine the density of sediments or rocks

under the seafloor up to the mantle. To convert seismic velocity into sediment density, one can easily adopt the most convenient empirical variation curve among those existing for a set of marine sediments and rocks exist (Table 11). They were produced from experimental (laboratory) data and drilling (in situ) measurements. Hamilton (1978) stated that the choice of the appropriate sediment-rock curve from which extracting density is more important and sensible when dealing with lower seismic velocities (4 to 5 km/s).

I used the Ludwig et al. (1970) equation that is based on the classical Nafe and Drake curve as it is generally valid for a wide range of rock types and thus applicable to the overall sedimentary column. Other relations available in literature are limited to specific sediment types or seismic velocities. Velocity values in the sedimentary column were derived from the available Expanding Spread Profiles (ESP) results and seismic surveys conducted in the EMS.

Table 11 Empirical regression equations relating compressional wave velocities to sediments and rocks densities.

Layer type	**Regression equation (V_p in km/s and ρ in g/cm^3)**
Sea floor Surface (Magara)	$\rho = 14.8\ V_p - 21.014$
Soft sediment (Magara :0-500 m with $1.53 < V_p < 2$)	$\rho = 1.135\ V_p - 0.190$
Shale (average of Magara and Perrier-Quiblier) up to 3 km	$\rho = 0.917 + 0.744\ V_p - 0.08\ V_p^2$
Marine calcareous sediments and rocks (Hamilton, 1978)	$\rho = 0.112\ V_p + 1.979$ (between 3 km/s and 6.6 km/s)
	$\rho = 2.351 - 7.497\ V_p^{-4.656}$ (between 1.9 and 3 km/s)
Marine siliceous sediments and rocks (Hamilton, 1978) from 0 to 500 m	$\rho = -2.770 + 4.316\ V_p - 1.102\ V_p^2$ (diatomaceous)
	$\rho = 1.124 + 0.347\ V_p - 0.0157\ V_p^2$
Christensen and Salisbury (1982) for Basalts (500 m depth)	$V_p = 2.33 + 0.081\ \rho^{3.63}$
Gardner et al., 1974 (valid for $1.5 < V_p < 6.1$)	$\rho = 0.23\ V_p^{0.25}$ (V_p in ft/s)
Ludwig et al. (1970)	$\rho = 1.6612\ V_p - 0.4721\ V_p^2 + 0.0671\ V_p^3 - 0.0043\ V_p^4 + 0.000106\ V_p^5$
Christensen and Mooney (1995) for crystalline rocks ($5.5 < V_p < 7.5$)	$\rho = 0.541 + 0.3601\ V_p$
Godfrey et al. (1997) for basalt, diabase and gabbro at depth of 10 km ($5.9 < V_p < 7.1$)	$\rho = 2.4372 + 0.0761\ V_p$

After plotting bulk density values in function of depth below seabed obtained from different sources (measured in ODP and DSDP, converted density from seismic velocity) against the bulk density variation curve (related to porosity, Athy 1930), it was clear that this latter does not accurately represent the variation of bulk densities

and the trend does not reflect the true density variation with depth (Fig. 41). In fact, in the shallower layer, the initial porosity and density of sediments rapidly vary with depth. The predicted curve does not manage to follow this initial trend of density variation. In addition, it overestimates density values for the following deeper sequences. Therefore, this curve (related to porosity, Athy 1930) will not be adopted for further calculations. A detailed stratigraphic study will be conducted and bulk density variation curves will be obtained after controlling and analysing available seismic surveys results.

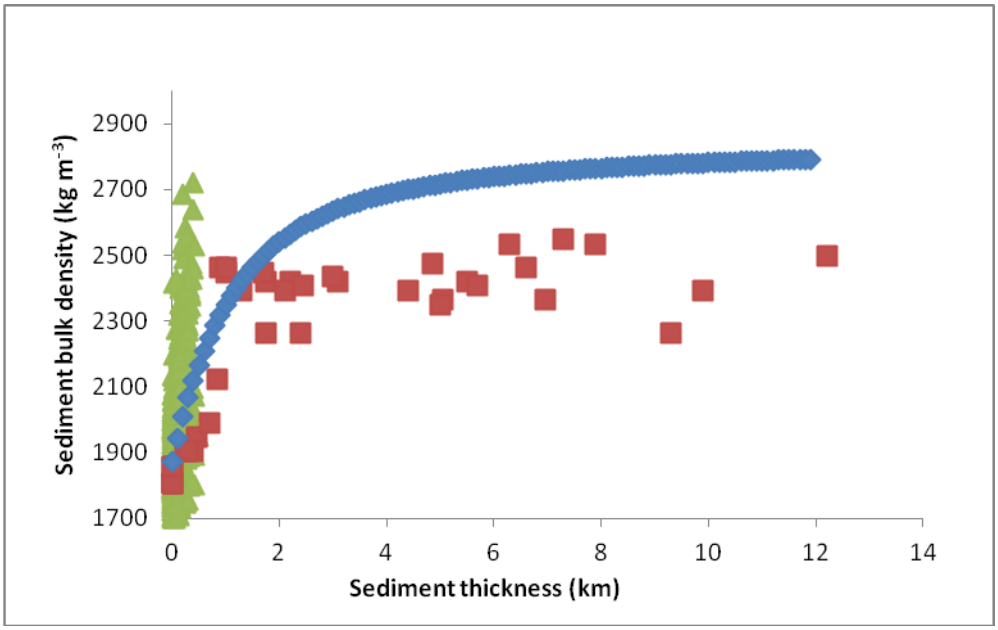

Fig. 41 Bulk Density variation with depth below the seabed from different methods Blue: all sediment types available in the study area (EMS) as deduced from the relation between porosity and density. Green triangles: measured bulk density from ODP and DSDP. Red squares: density values after converting seismic velocities).

5.4 Seismo-stratigraphy

Measurements on rock samples and in drilled boreholes present a direct evaluation of rock properties but are limited to upper sediment layers. Indirect geophysical methods (i.e. gravity, magnetic, seismic) may produce additional information about the deeper layers. Both direct and indirect methods complement each other either by constraining geophysical models through the adoption of observed parameters or by determining lateral variations of rocks properties and lithospheric depths.

It is convenient to subdivide the EMS into the several basins and to analyse the physical properties of the lithosphere and overlying sediments of each. Such sedimentary basins are characterized by sediments that accumulated and preserved for long time periods. de Voogd et al., 1992 stated that a thick layer (reaching 12 km) of fragmented and stacked sediments started depositing since the Mesozoic era in the Mediterranean oceanic basins and margins. The Messinian crisis event affected almost all basins and resulted in a thick evaporitic layer (Finetti, 1976).

Direct measurements from ODP and DSDP boreholes were available but limited to the Plio-Quaternary and evaporitic layers with a maximum depth that reached 600m (see Section 5.2). Thus For the rest of the sedimentary column, bulk density can be estimated through seismic velocity conversions. To determine the vertical and lateral distribution of sedimentary layers, I used geophysical data from available Expanding Spread Profiles (ESP) and seismic profiles in the EMS. Moreover I inferred the sediment bulk density variation as function of depth down to the crystalline basement by converting seismic velocity into density. Figure 42 shows the position of the seismic profiles and Expanding Spread Profiles (ESP) that were chosen and analysed.

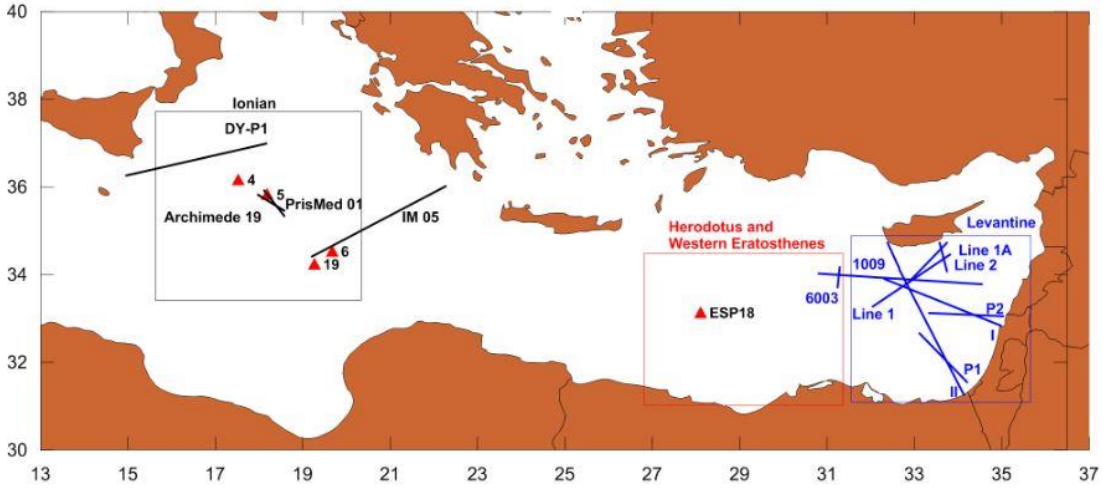

Fig. 42 Distribution and positions of ESPs and seismic profiles used in the EMS relatively to the different sedimentary basins and main seabed features. In the Ionian Basin: Wide-angle seismic profile DY-P1 (after Dellong et al., 2018), seismic profiles PrisMed 01 and Archimede 19 (after Gallais et al., 2011) and ESPs 4, 5, 6 and 19. In the Western Mediterranean Ridge: seismic profiles PR3 (after Makris et al., 2006) and a part of IM 05 (after Chamot-Rooke et al., 2005). In the Herodotus Basin: ESP 18 and a part of seismic profiles 1009 and 6003 (after Papadimitriou, 2017) to the western Eratosthenes Seamount. In the Levantine Basin: Seismic profiles Line 1, 1A and 2 (after Welford et al., 2015), seismic profiles (after Ben Avraham et al., 2002) and profiles P1 and P2 (after Netzeband et al., 2006)

Seismic data from Expanding Spread Profiles (ESP) are perhaps the most important information on the velocity structure of the EMS (de Voogd et al. 1992), even if the limitation of the one-dimension velocity model of this technique along a seismic line and its lateral homogeneity should be accounted for. On the top of the sedimentary cover, ESPs show Messinian evaporites that cause velocity inversions but do not prevent reaching Moho depths. This allowed de Voogd (1992) to identify the Moho boundary and the main crustal units, from the Calabrian prism to the west to the Mediterranean Ridge and Herodotus Sea to the east. The crust and the Moho were easily identifiable from their higher velocity values (6.2 to 8.6 km/s). Depositional sequence starts with a Plio-Quaternary unconsolidated sediments (1.8 to 2.2 km/s), followed by one or two layers of evaporites (4 to 4.6 km/s) after which one or two Mesozoic sedimentary layers (3 to 5 km/s) and finally an ambiguous layer considered an oceanic layer with low seismic velocity values (4.8 to 6.8 km/s) due to particular geological effects, intrusions or deformations.

The five ESPs stratigraphic sequences were checked and are summarised in table 12 and figure 43, after conducting a close analysis and comparison of various direct and

indirect data measurements. For the shallowest layers of newly deposited and unconsolidated sediments I proceeded by comparing information from ESP 4, 5 and 18, and the nearby ODP Leg 160 – 964 A (Emeis et al., 1996), DSDP Leg 13 site 130 (Hsü et al., 1973) and Leg 42 site 374 (Hsü and Montadert, 1978).

Table 12 Sedimentary and crustal layering based on ESP interpretation results after de Voogd et al., 1992. Density values were obtained from the empirical relation of Ludwig, 1970 except for evaporites where a mean value was adopted (see explanation in the text).

ESP 5 Ionian Basin	**Layer**	**Depth interval (km)**	**Layer thickness (km)**	**Velocity top – bottom (km/s)**	**Density ($kg.m^{-3}$)**
	Water Column	0 – 3.9	3.9	1.5	1030
	Recent Sediments (Plio-Quaternary)	3.9 – 4.35	0.45	1.9 – 2.1	1900
	Upper and Lower Evaporites units (intra-Messinian of halite composition)	4.35 – 4.8	0.45	4.5	2200
		4.8 – 5.65	0.85	4.2	2200
	Cenozoic – Tertiary Tortonian age Sediments (Velocity inversion: pre-Messinian velocity < than evaporites above)	5.65 – 6.3	0.65	3 – 3.2	2260
		6.3 – 8.95	2.65	3.8	2360
	Deformed oceanic layer (de Voogd, 1992)	8.95 – 10.2	1.25	4.7 – 5.0	2510
	Crust	10.2 – 12.3	2.1	6.2 – 6.4	2780
		12.3 – 17.3	5	7.1	2990
	Moho - Top of Mantle	≥ 17.3		8.5	≥ 3300
ESP 4 Beneath the Calabrian prism	Water Column	0 – 3.5	3.5	1.5	1030
	Recent Sediments (Plio-Quaternary)	3.5 – 3.75	0.25	1.8 – 2	1850
	Upper and Lower Evaporites units	3.75 – 5.2	1.45	4.4	2200
		5.2 – 6.6	1.4	4.2	2200
	Cenozoic -Tertiary Sediments (Velocity inversion: pre-Messinian velocity < than evaporites above)	6.6 – 10.45	3.85	3 – 3.8	2300
	Deformed oceanic layer (de Voogd, 1992)	10.45 – 11.4	0.95	4.8 – 5	2510
	Crust	11.4 – 14.9	3.5	6.3 – 6.5	2800
		14.9 – 19.65	4.75	7.45	3100
	Moho - Top of Mantle	≥ 19.65		8.5	≥ 3300
ESP 19 Sirte Basin	Water Column	0 – 3.8	3.8	1.5	1030
	Recent Sediments (Plio-Quaternary)	3.8 – 4.2	0.4	1.8 – 2	1850
	Upper and Lower Evaporites units	4.2 – 4.8	0.6	4.4	2200
		4.8 – 6	1.2	4.2	2200
	Cenozoic -Tertiary Sediments (Velocity inversion: pre-Messinian velocity < than evaporites above)	6 – 8.2	2.2	3 – 4	2320
		8.2 – 9.3	1.1	4.2	2420
	Deformed oceanic layer (de Voogd, 1992)	9.3 – 11.1	1.8	4.9 – 5.1	2530
	Crust	11.1 – 14.2	3.1	6.4 – 6.6	2830
		14.2 – 18.4	4.2	7.15	3010
	Moho - Top of Mantle	≥ 18.4		8.5	≥ 3300
ESP 6 Western Med Ridge	Water Column	0 – 3.1	3.1	1.5	1030
	Recent Sediments (Plio-Quaternary)	3.1 – 3.4	0.3	1.8 – 2	1850
	Upper and Lower Evaporites units	3.4 – 4.1	0.7	4.5	2200
		4.1 – 4.4	0.3	4	2200
	Cenozoic -Tertiary Sediments (Velocity inversion: pre-Messinian velocity < than evaporites above)	4.4 – 8.1	3.7	3.5 – 3.7	2330
		8.1 – 8.8	0.7	4.1	2400
	Deformed oceanic layer (de	8.8 – 9.7	0.9	4.5	2460

	Voogd, 1992)				
	Crust (basalt)	9.7 – 12.3	2.6	6.2 – 6.5	2790
		12.3 – 16.2	3.9	6.7 – 6.8	2900
		16.2 – 19.8	3.6	7.1	2990
	Moho - Top of Mantle	≥ 19.8		8.4	≥ 3300
ESP 18 Herodotus Basin	Water Column	0 – 3	3	1.5	1030
	Recent Sediments (Plio-Quaternary - thickness related to proximity from Nile Delta)	3 – 3.7	0.7	1.9 – 2.2	1920
		3.7 – 3.85	0.15	2.4 – 2.6	2100
		3.85 – 4.75	0.9	2.8 – 3.2	2210
		4.75 – 5.1	0.35	3.7 – 4	2370
	Three Evaporites layers	5.1 – 5.45	0.35	4.1	2200
		5.45 – 6	0.55	4.3	2200
		6 – 7.85	1.85	4.6	2200
	Cenozoic-Tertiary Sediments(Velocity inversion (pre-Messinian velocity < than evaporites above)	7.85 – 12.3	4.45	3 – 3.2	2240
	Deformed oceanic layer or thinned continental (de Voogd, 1992)	12.3 – 12.9	0.6	4	2390
	Crust	12.9 – 15.2	2.3	4.75	2490
		15.2 – 21.75	6.55	5.5	2620
		21.75 – 22.5	0.75	6.5	2830
		22.5 – 23.5	1	7.4	3090
	Moho - Top of Mantle	≥ 23.5		8.6	≥ 3300

Table 12. (continued)

For ODP 964A located in the Strait of Sicily at the foot of the Calabrian Ridge, 120 m of terrigenous and calcareous pelagic sediments were found extending up to 250 m as shown in ESP 4 results. For DSDP 374 located in the central Messina Abyssal Plain, only the top of the evaporites deposition was observed between 381 and 457 m (the deepest reached penetration of the borehole) following a terrigenous and turbidites deposits between the seabed and 381 m (Hsü andand Montadert, 1978). Such information is in good accordance with the nearby ESP 5 where recent Plio-Quaternary sediments were observed between the seabed and 450 m followed by 1.3 km of evaporites. Velocity models of Le Meur (1997) showed an increase of the evaporitic sequence from 1.1 km in the Sirte Abyssal Plain to 1.9 km in the Ionian Abyssal Plain. For DSDP 130 located in the distal part of the western Nile Cone, the very shallow penetration did not allow to reveal the nature of the second depositional sequence but confirmed the terrigenous type of sediments noted to be very thick (2.45 km) in the ESP 18 and resulting from the Nile Cone sedimentation transport effect.

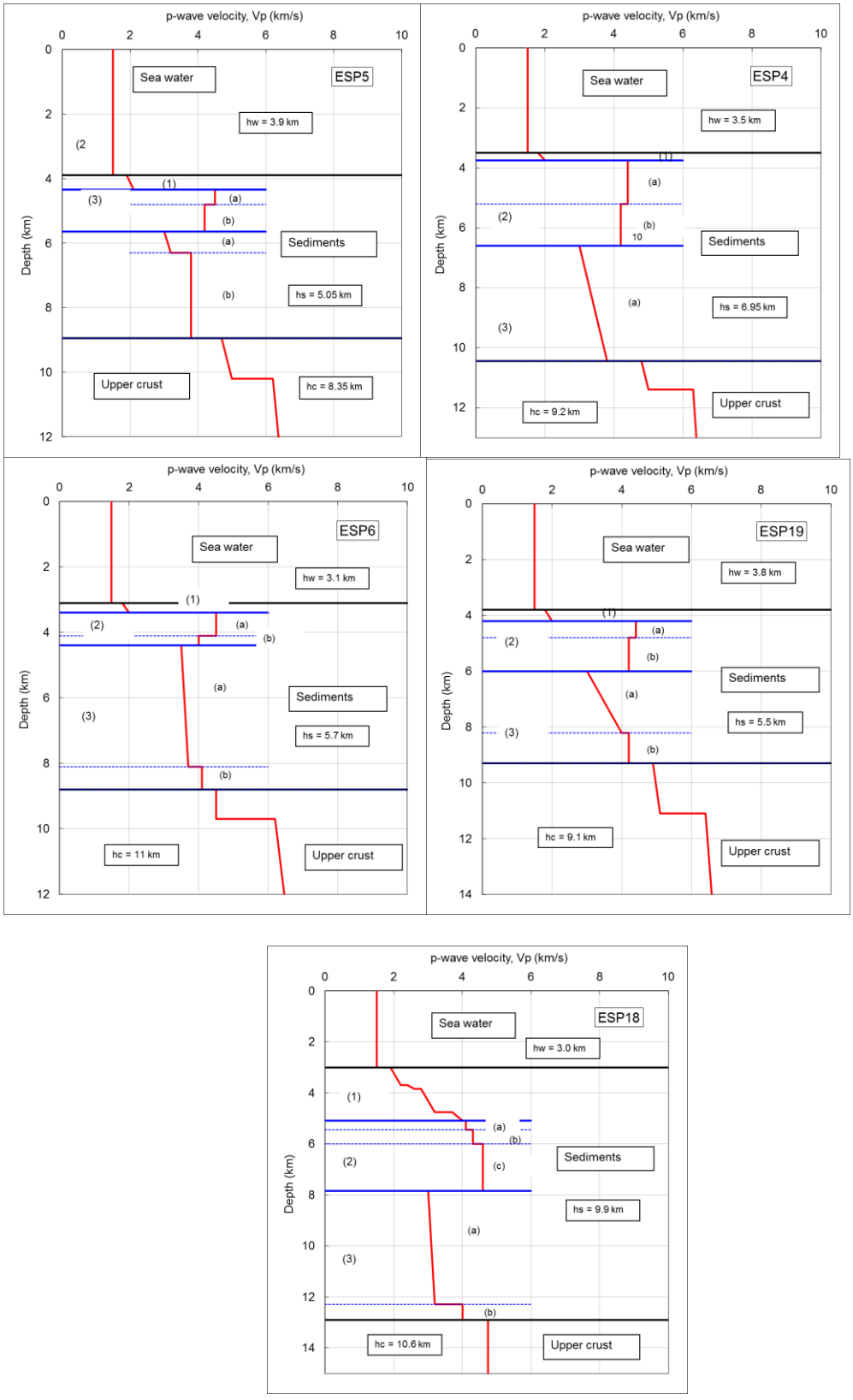

Fig. 43 Velocity models (p-wave velocity, Vp) of expanding spread profiles (ESPs) central points, recorded during the Pasiphae cruise. (1) Plio-Quaternary sediments, (2) Messinian deposits, (3) pre-Messinian sediments. For (a), (b) and (c) see table 13.

5.4.1 Sediment and crustal thickness in the Ionian Basin

In the Ionian Sea, a very thick (~10 km) layer of sediments overlies an old Tethyan oceanic crust in the south becoming in the north a relic of the Apulian continental margin (Finetti, 1982, Mueller, Stephan & Kahle, Hans-Gert, 1993). Thick Messinian evaporites underlay the Ionian Abyssal Plain (Gallais et al., 2012; Minelli and Faccenna, 2010; Delong et al., 2018). The interpretation of Dellong et al. (2018) for seismic profile DY-P1 showed a sedimentary infill in the deep Ionian Basin with thickness ranging between 8 and 12 km separated into four layers with thickness, seismic velocities and densities as shown in table 13. The uppermost sedimentary layer of the Ionian Basin is a young layer with high water content and low velocities corresponding to the Plio-Quaternary sediments. A velocity inversion was modelled between the second evaporitic layer (4.3 and 4.6 km/s) and the third layer (3.2 and 3.6 km/s) assumed to be of Mesozoic origin. The fourth sedimentary layer considered as ambiguous for de Voogd et al., (1992) was interpreted by Gallais et al., (2011) as consolidated Jurassic-Cretaceous carbonates. Crustal thickness ranges between 7 and 9 km in the Ionian Basin (Makris et al., 1986).

Two distinct crustal layers are found; between Malta escarpment and the IAP they are considered as thinned continental crust (two layers of equal thicknesses). In the Ionian deep basin, they were best interpreted as an old and highly compacted oceanic crust with the hypothesis of a peridotites intruded oceanic crust or partially serpentinized upper mantle though having higher velocities values with respect to normal oceanic crust.

De Voogd et al. (1992) compared the general features of the crust in the Ionian Abyssal Plain with the average oceanic crustal model of Spudich and Orcutt (1980) and noticed the similarity regarding crustal thickness, presence of velocity gradient in the upper crustal layer and high velocity within the two lower layers.

Moho depth is observed at 16 to 18 km (Gallais et al., 2011). Such values agree with the global values of Laske (2013). Mantle layer velocities range between 8.1 km/s at the Moho interface and 8.4 km/s at the bottom.

Table 13 Sediments and crustal layers distribution along DY-P1 seismic profile (after Dellong et al., 2018)

Layer	**Thickness (km)**	**Velocity (km/s)**	**Density (kg/m^3)**
Plio-Quaternary	0.7	2.2	2200
Evaporites	1.8	4.6	2200
Mesozoic	2.5	3.6	2360
Ambiguous unit of consolidated sediments (Jurassic-Cretaceous Mesozoic carbonates)	5.0	4.8	2490
Upper-crustal layer (Oceanic)	2.5	6.5	2760
Lower-crustal layer (Oceanic)	4	7.5	3060
Upper-Mantle		8.1	3330

Notice that evaporites have high seismic velocities due to their crystalline structure and may be of density lower than that obtained from velocity-density conversion (de

Voogd et al., 1992; Dellong et al., 2018). Evaporites bulk density depends on their mineral composition (i.e. 1860 kg/m^3 for sylvite, 2040 kg.m^{-3} for halite, 2350 kg.m^{-3} for gypsum and 2980 kg.m^{-3} for anhydrites). This is the case of the Eastern Mediterranean Basins where the few direct measurements from ODP and DSDP gave drilling bulk densities different than what would be obtained from direct conversions (~2470 kg.m^{-3}). Few ODP and DSDP reached the evaporitic layer: ODP 160-967A shows few evaporitic sediments at 120 m depth with drilling bulk density ranging between 1876 and 2185 kg.m^{-3}. Another evaporitic horizon was found at 90 m depth in the DSDP 13-125A with a drilling bulk density of 1740 kg/m^3. However, the in the Tyrrhenian Basin well closer to the investigated area, the mean bulk densities for evaporites is 2230 kg.m^{-3} (Pasquale et al., 2006).

5.4.2 Sediment and crustal thickness in the Levantine and Herodotus basins

The Levantine Basin is underlain by a succession of sediments deposited in deep-water mixed settings resulting from high-stand systems (carbonate platforms) and low-stand systems (siliciclastic and carbonate turbidite complexes) (Gardosh et al., 2008; Inati et al., 2016). The Levantine margins at the African and Arabian plates witnessed the generation of siliciclastic-carbonate platforms during a post-rift phase. The subsidence history continued at the end of the Mesozoic with terrigenous sedimentation deriving from continental inputs and replacing carbonates (Inati et al., 2016). Isopach maps (Papadimitriou, 2017) revealed a 2.5 km Late Jurassic unit near the Eratosthenes Seamount. This unit gets thinner towards the Levantine Basin with an even sediment distribution; the overlying cretaceous deep layer is thicker, reaching 1.5 km. The Early-Miocene sequence thickness is about 1.2 km. At the top, Messinian and Pliocene sediments were deposited. Evaporites thickness varies in the Levantine Basin and is thinner in the north than in the south with 1.5 – 2 km thickness in the centre of the Basin (Nader, 2011; Inati, 2017; Papadimitriou, 2017). The Plio-Quaternary in the Levantine Basin may be considered of uniform thickness of 1.4 km.

Some seismic studies constrained by use of wells (Garfunkel, 1998; Ben-Avraham, 2002; Rybakov and Segev, 2004; Netzeband et al., 2006; Gardosh et al., 2008; Steinberg et al., 2011; Papadimitriou, 2017) revealed the Levantine Basin sedimentary infill. Interpreted reflection data (Ben-Avraham et al., 2002) revealed the existence of an uppermost sedimentary layer (200 – 700 m thickness; 2.0 – 2.5 km/s) followed by salt and evaporites (2 km; 4.2 km/s), which is followed by a thick velocity inversion layer of 3.8 km/s. The last layer probably of highly compacted pre-tertiary sediments has a velocity of 4.5 km/s. The crystalline basement is characterized by a high velocity of 6.7 – 7 km/s interpreted as an oceanic crust (Ben-Avraham et al., 2002).

Messinian evaporites and underlying sedimentary cover were inferred in the Levantine Basin by Welford et al. (2015) and of similar thickness ((10 – 14 km) as suggested by Ben-Avraham et al. (2002). This was an indication of the regionally continuous shallow velocity structure of the Levantine and a Moho located between

19 and 22 km. Density models were estimated from velocity models after dividing it into zones of similar velocity and by using the relationship from Ludwig et al. (1970). Netzeband et al., (2006) presented an uppermost layer consisting of Plio-Quaternary sediments (1.9 – 2.1 km/s) followed by an evaporitic layer (4.3 – 4.4 km/s) over older Jurassic-Miocene sediments (3.5 – 3.9 km/s and 3.7 – 4.4 km/s). The last sedimentary layer was identified as marine carbonates (4.4 – 4.8 km/s and 4.6 – 4.9 km/s). Differently from the interpretation of Ben-Avraham et al. (2002), Netzeband et al., (2006) suggest a crust of continental nature that is divided into two layers, an upper one (with velocity ranging from 5.7 to 6.4 km/s) and a lower one (6.4 –6.9 km/s). V velocity in the uppermost mantle is 7.8 – 7.9 km/s.

Recent interpretation of refraction seismic lines (Papadimitriou, 2017) revealed the sedimentary sequences between the Levantine and Herodotus Basins through the top of the Eratosthenes Seamount. The sequences are in general agreement with other previous studies and vary between an upper Pliocene sequence followed by the evaporitic Messinian layer then by the Eocene – Miocene sequence. The deepest sedimentary sequence is the pre-Tertiary – Mesozoic one (deep marine turbidites or carbonates and carbonate platforms).

The crust of the Levantine and Herodotus Basins is relatively thin. The Levantine Basin may be a transitional domain occurring between the unstretched continental crust, onshore, and the oceanic crust beneath the Herodotus Basin. Inati (2017) suggested a crystalline crust which thins from 35 km under the Arabian plate to 8 km in the Levantine Basin. Inati also suggests that the initial pre-rift crustal thickness was 25 km. Geophysical modelling demonstrated a continental crust flooring the Levantine Basin divided into an upper crust of 2750 $kg.m^{-3}$ and a lower crust of 2900 $kg.m^{-3}$ (Netzeband et al., 2006, Inati (2017) and an oceanic crust (only one thin layer) flooring the Herodotus Basin.

The Levantine Basin stratigraphy is summarized in Table 14 showing the resulting velocity and density values of sequences as interpreted by the different authors.

Table 14 Sedimentary and lithospheric layers with relative velocity and density values for the Levantine Basin.

Layer	**Velocity (km/s)**	**Density (kg/m^3)**
Quaternary sediments	1.9 – 2.5	2200 – 2600 (density increase for compaction effect)
Evaporites (2 km thick)	4.2 – 4.4	2100
Cenozoic/Mesozoic	3.5 – 4.4	2500 (Density not dependent on pressure)
Palaeozoic and Mesozoic Carbonates	4.4 – 4.9	2650
Upper felsic crust	5.7 – 6.4	2650 – 2770 (Netzeband et al., 2006)
Lower mafic crust	6.4 – 6.9	2900 (Netzeband et al., 2006)
Oceanic crust	6.7 – 7	2900 (Ben-Avraham et al., 2002)
Upper mantle	7.8 – 7.9	3350 – Density is function of temperature: $3200(1+3.5*10^{-5}(T_a-T_z))$ with T_a=1330˚C (Inati, 2017)
LAB		3200

Tables 15 and 16 summarise the thickness, seismic velocity and density values in the EMS basin lithosphere as inferred from all the different direct and indirect pieces of information.

Table 15 Sedimentary and lithospheric layers with relative thickness, velocity and density values for the Eastern Mediterranean Basins.

Basin	**Layer**	**Thickness (km)**	**Velocity (km/s)**	**Density ($kg.m^{-3}$)**
Levantine	Recent Plio-Quaternary sediments	0.5 – 2	1.9 – 2.5	1600 – 2150
	Evaporites (Messinian)	1.5	4.2 – 4.4	1900 – 2200
	Hemipelagic – Pelagic marls (Eocene to Miocene)	4 – 5	3.5 – 4.4	2350 – 2500
	Highly compacted pre-tertiary deep marine and carbonates (Jurassic to Eocene)	2 – 4	4.4 – 4.9	2650
	Upper crystalline basement	7 – 8	5.7 – 6.2	2650 – 2770
	Intruded lower crystalline basement	0.5 – 2	6.4 – 6.9	2840 – 2900
	Oceanic basement		6.8 – 7.0	2900 – 3000
	Upper mantle		7.8 – 8.0	3200 – 3350
Herodotus	Recent Plio-Quaternary sediments	1.5 – 3	1.9 – 4	1600 – 2300
	Evaporites (Messinian)	1.5 – 2	4.1 – 4.6	2000 – 2200
	Cenozoic – Tertiary sediments	4 – 5	3 – 4	2240 – 2390
	Mesozoic compacted sediments	4 – 5	4.5 – 5.9	2490 – 2600
	Oceanic crust	6 – 7	6 – 7.4	2900 – 3090
	Upper mantle		8.6	3300
Ionian	Recent Plio-Quaternary sediments	0.2 – 0.6	1.9 – 2.2	1600 – 2200
	Evaporites (Messinian)	1 – 1.5	4.2 – 4.5	1700 – 2200
	Cenozoic – Tertiary Tortonian sediments	4	3.0 – 3.8	2260 – 2360
	Mesozoic compacted carbonates sediments	2.7	4.7 – 5.0	2510
	Basaltic oceanic crust	6.7	6.2 – 7.4	2780 – 2990
	Upper mantle		8.5	3300

Table 16 Average sediment, crustal and lithospheric thicknesses for the different basins and margins of the EMS. Lithosphere thickness after Calcagnile and Panza (1981) and Inati et al. (2016)

Basin	Moho Depth	Lithospheric thickness	Crustal thickness	Sediment thickness
Levantine	20 – 23	100 – 150	7 – 9 (thin continental)	12 – 14
Herodotus	26	180	6 – 10 (oceanic)	10
Ionian	16 – 18	90	7 – 9 (oceanic)	6 – 8

5.5 Bulk density models

Figure 44 shows the bulk density variation with depth in sediments for the Eastern Mediterranean Sea as inferred from core sample measurements and by conversion of seismic data. The best fitting curves are a logarithmic one from the seabed to 3000 m of sediment thickness, and a linear curve to larger depth. Due to the large scatter of data, it is highly likely that calculations of sediment corrections and water-loaded depths can be largely biased (see section 6).

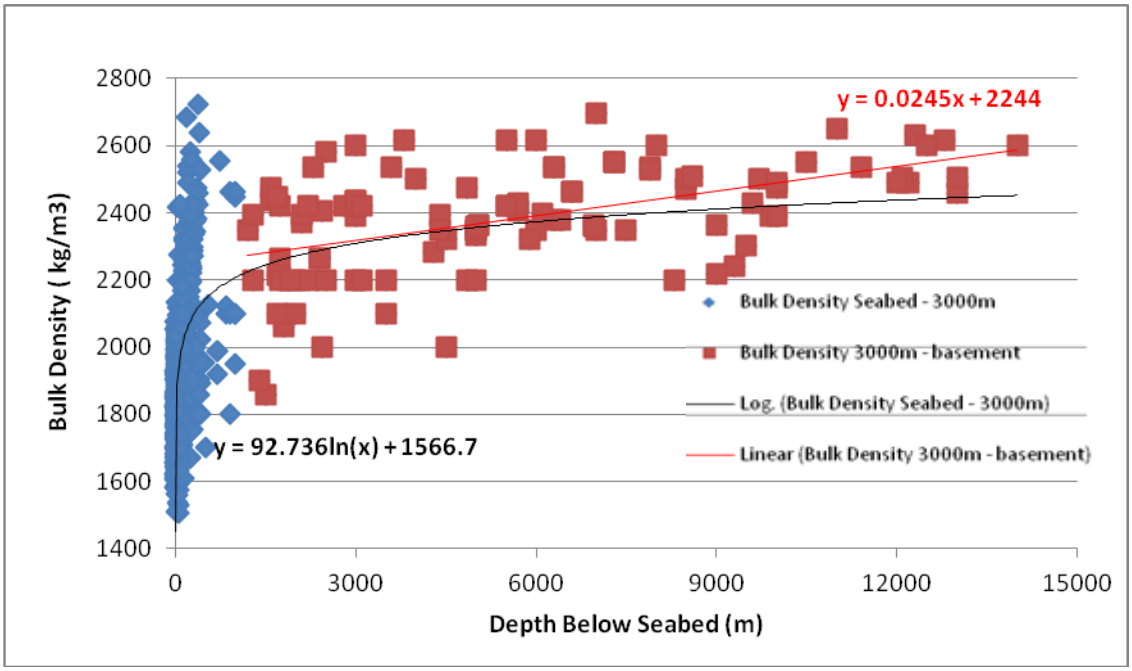

Fig. 44 Bulk density with depth below the seabed -in the EMS. The logarithmic curve matches the bulk density data in the 0-3000 m depth range. The linear curve is the best fit line from 3000 m to the crystalline basement.

Since the different basins of the EMS are characterized by different stratigraphic and crustal settings, I preferred to determine an independent bulk density model for each of them. This allows more reliable calculations of the sediment correction. For the Herodotus and Ionian basins, the density-depth variation is well matched with logarithmic model from the seabed to 3000 m and by a linear curve at larger depth. A simple logarithmic curve well describes the bulk density variation in the Levantine

Basin. Figures 45-47 presents the bulk density variation with depth for each basin of the EMS.

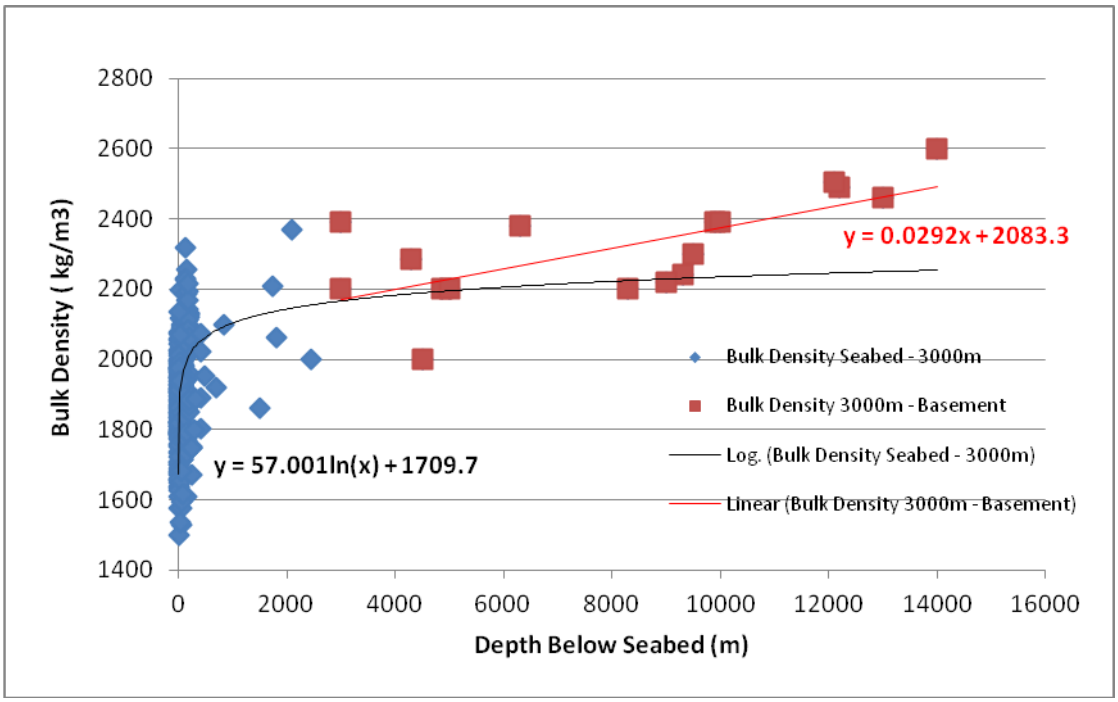

Fig. 45 Model curves of bulk density variation with depth below seabed for the Herodotus Basin.

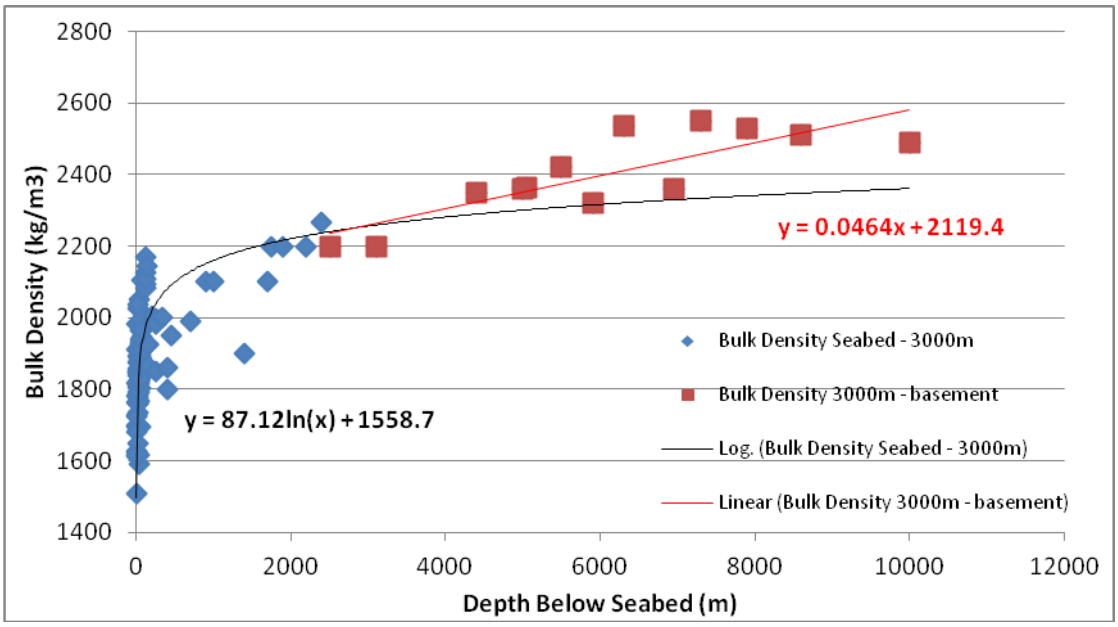

Fig. 46 Model curves of bulk density variation with depth below seabed for the Ionian Basin.

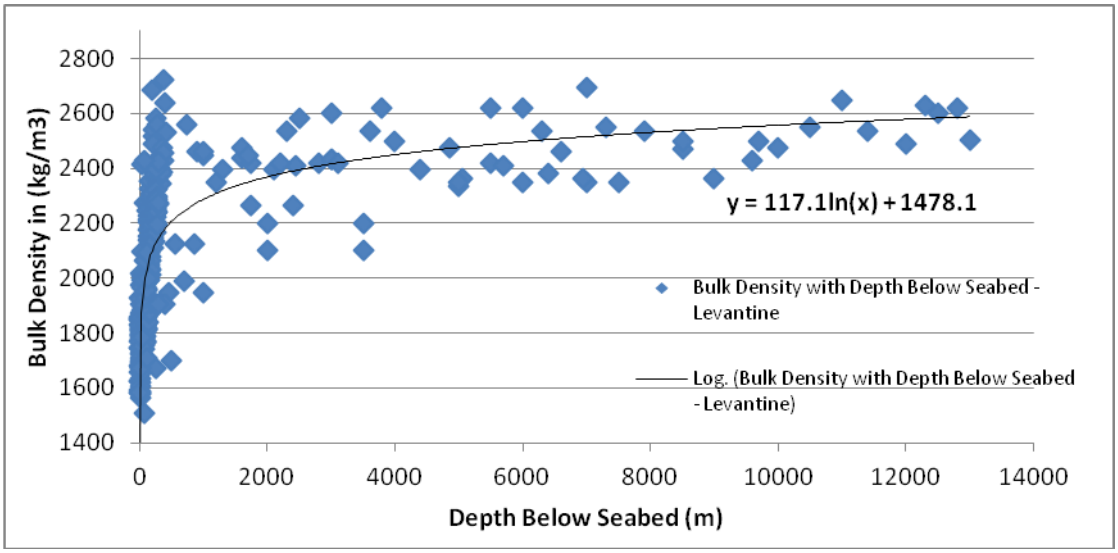

Fig. 47 Model curves of bulk density variation with depth below seabed for the Levantine Basin.

6. SEAFLOOR WATER-LOADED DEPTH

To understand the tectonic processes which contributed to the formation of the EMS basins, numerous geophysical and geological data relative to the lithospheric structure are needed. Observation of magnetic anomalies might provide information about the structure and dynamics of oceanic basins. Sedimentological analysis might give interesting information related to vertical and horizontal movements of the upper basement surface. The analysis of the seafloor water-loaded depth (WLD) can be an important tool to study the EMS evolution.

To calculate the WLD it is necessary to consider water depth and sediment thickness and to assume that the upper surface of the basement coincides with the mean sea level at the beginning of the basin formation. The subsidence of the upper surface of the basement is the sum of water depth and sediment thickness. To transform this subsidence into WLD, it is necessary to remove the sediment layer, thus eliminate the subsidence of the basement surface caused by the deposition of the sedimentary layer (sediment correction). In oceanic areas, an additional crustal correction is required.

6.1 Sediment and crustal correction

Sediment accumulation over a newly formed basin is the principal cause of subsidence of the basement surface. The large weight of sediments deposited causes the crust to sink. The effect of such sedimentary cover can be calculated through an equation that balances the masses of two lithospheric columns one with a sediment cover and the other without (Fig. 48). The sedimentary correction, C_s, assuming that the basement was initially aligned with sea level before the basin formation, is thus given by:

$$C_s = \frac{\rho_a - \rho_s}{\rho_a - \rho_w} h_s \qquad 6.1$$

where ρ_a is the asthenosphere density, ρ_w the seawater density, ρ_s the bulk density of the sedimentary column, and h_s is the sedimentary column thickness. The bulk density increases with sediment compaction as it depends on fluid in the pore space and the solid grains.

It must be stressed that the foregoing equations assume an Airy local isostatic compensation. If compensation was reached regionally and not locally, the effect of sediments load should be calculated considering the flexural load of a thin elastic or viscoelastic plate. However, flexural loading and local isostatic model are similar in regions where sediments have a uniform lateral thickness at all nearby points

(Sawyer, 1985; Heine et al., 2008). This condition is reasonably applicable at least in the central portions of the Eastern Mediterranean Sea.

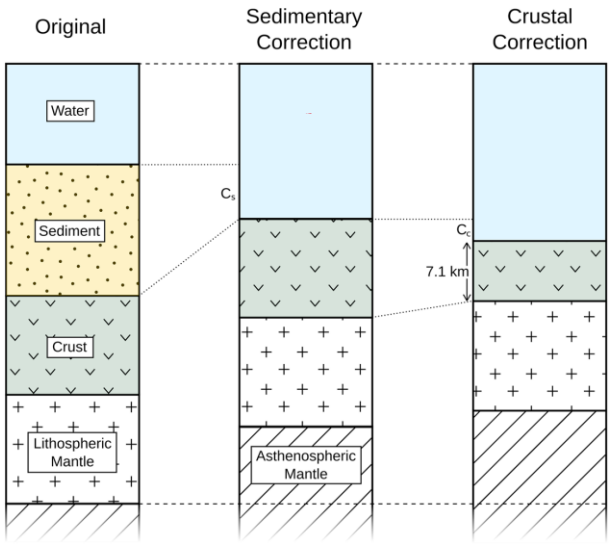

Fig. 48 Isostatic balances for sedimentary and crustal corrections. Sedimentary correction, C_s, replaces sedimentary mass with equivalent mass of water and asthenospheric mantle. Crustal correction, $_{Cc}$, replaces mass of oceanic crust with mass of reference 7.1 km of crust, water, and asthenospheric mantle (after Hoggard et al., 2017).

I used the basins model curves of bulk density variation with depth as obtained in Section 5.5. and calculated the sediment correction as a function of the sedimentary column thickness for the Eastern Mediterranean basins. Figure 49 shows the calculations with the eq. (6.1) by assuming ρ_a = 3200 kg m^{-3} and ρ_w = 1030 kg m^{-3}. Notice that the sediment correction is not the same for all the basins of the area of interest. This argues that the area of study should be analysed on a basin scale in order to better evaluate water-loaded depth values.

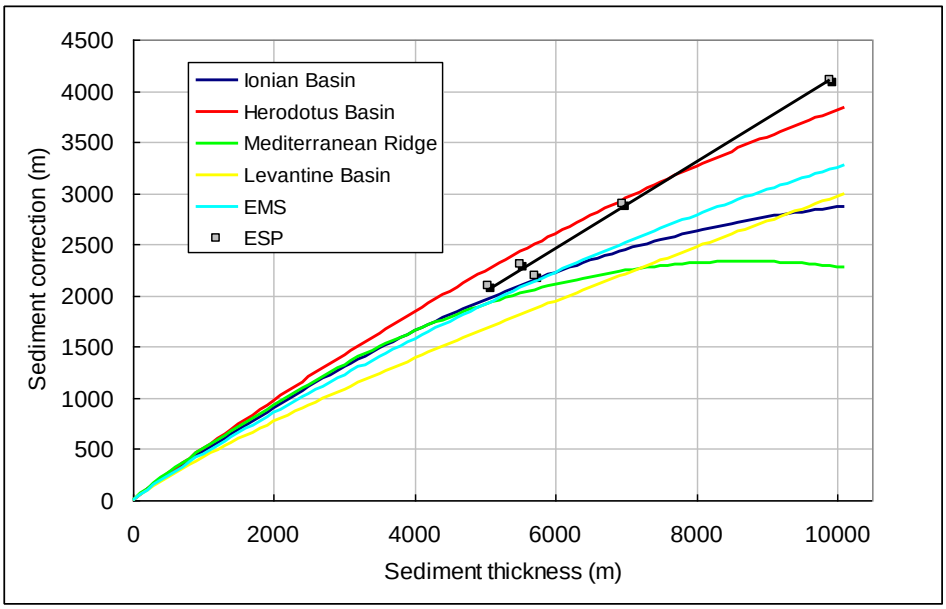

Fig. 49 Different sediment correction variation curves plotted as a function of sediment thickness from density-depth data reported in Section 5.5, together with the linear interpolation of the C_s results obtained from sediment and bulk density data inferred in the five ESP sites of the Ionian and Herodotus Basins (see also Table 20).

In order to check the validity of the sediment correction curves of figure 49, I used, as constraints, the data from five available expanding spread profiles (ESP) that provide the best information we have on the structure of the crust in the deep Ionian, Sirte and Herodotus basins (de Voogd et al., 1992).

In particular, the crust within the Ionian (ESP 5) and Sirte (ESP 19) basins has a thickness of about 9 km and a typical oceanic seismic stratigraphy. The sedimentary thickness is large, more than 5 but less than 6 km. In the Herodotus basin (ESP 18), the sedimentary thickness is so large 10 km that the seismic stratigraphy is not well resolved and the actual position of the crust–sediment interface is uncertain (see discussion by de Voogd et al. 1992). However, the crustal thickness is about 11 km. According for the authors the thin crust of the Herodotus basin may be interpreted either as oceanic or thinned continental crust (see also Table 17). The location of the available ESP is shown in figure 50.

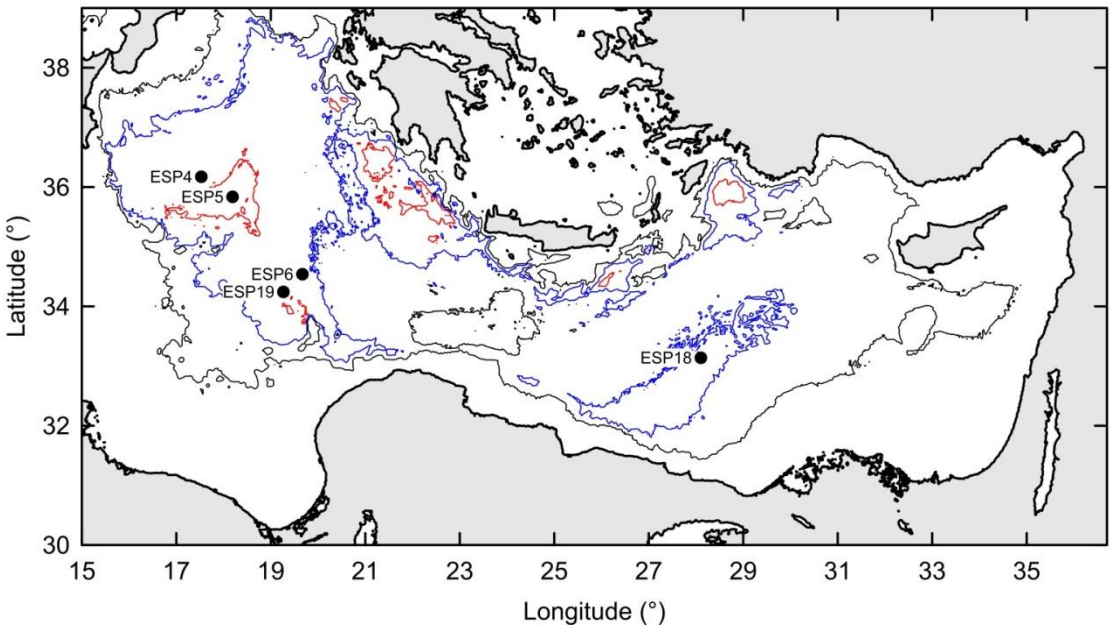

Fig. 50 Location of the ESP sites by de Voodg et al. (1992). Bathymetries of -2000 m (black curve), -30000 m (blue curve) and -4000 m (red curve) are indicated.

In each ESP sites, after converting seismic velocities into bulk densities for each seismic sequence/sediment deposition layer, a mean bulk density BD was obtained by

$$BD=(\Sigma\ BD_{layer}*h_{layer})/H \qquad 6.2$$

where BD_{layer} is the bulk density of each layer, h_{layer} is the thickness of each layer and H the total sediment thickness. The results of C_s for each EPS site are reported in table 17.

Table 17 Sediment correction (Cs) and bulk density (BD) calculation from the ESPs data. WD = water density; MD = mantle density; h = layer thickness

ESP	Layer	Age	Depth km	Thickness (h) km	Vp km/s	BD kg/m3	Used BD kg/m3	BD x h
4	1	Plio-Quaternary	3.5-3.75	0.25	1.8-2.0	1758-1880	1820	455
	2a	Messinian	3.75-5.20	1.45	4.4	2300	2300	3335
	2b	Messinian	5.20-6.6	1.4	4.2	2200	2200	3080
	3a	Pre-Messinian	6.6-10.45	3.85	3.0-3.8	2305-2420	2363	9097.55
	3b	Pre-Messinian	10.45-11.40	0.95	4.8-5.0	2547-2571	2559	2431.05
			H (km)	7.9			BD (kg/m3)	2329
							WD (kg/m3)	1030
							MD (kg/m3)	3200
							Cs (km)	**3.2**

ESP	Layer	Age	Depth km	Thickness (h) km	Vp km/s	BD kg/m3	Used BD kg/m3	BD x h
5	1	Plio-Quaternary	3.90-4.35	0.45	1.9-2.1	1758-1981	1870	841.5
	2a	Messinian	4.35-4.80	0.45	4.5	2300	2300	1035
	2b	Messinian Halite	4.80-5.65	0.85	4.2	2200	2200	1870
	3a	Pre-Messinian	5.65-6.30	0.65	3.0-3.2	2305-2335	2320	1508
	3b	Pre-Messinian	6.30-8.95	2.65	3.8	2420	2420	6413
		Pre-Messinian	8.95-10.2	1.25	4.7-5.0	2534-2571	2553	3191.25
			H (km)	6.3			BD (kg/m3)	2359
							WD (kg/m3)	1030
							MD (kg/m3)	3200
							Cs (km)	**2.4**

ESP	Layer	Age	Depth km	Thickness (h) km	Vp km/s	BD kg/m3	Used BD kg/m3	BD x h
6	1	Plio-Quaternary	3.1-3.4	0.3	1.8-2.0	1758-1900	1820	546
	2a	Messinian	3.4-4.1	0.7	4.5	2300	2300	1610
	2b	Messinian	4.1-4.4	0.3	4.4	2200	2200	660
	3a	Pre-Messinian	4.4-8.1	3.7	3.5-3.7	2376-2404	2390	8843
	3b	Pre-Messinian	8.1-8.8	0.7	4.1	2456	2456	1719.2
	3c	Pre-Messinian	8.8-9.7	0.9	4.5	2509	2509	2258.1
			H (km)	6.6			BD (kg/m3)	2369
							WD (kg/m3)	1030
							MD (kg/m3)	3200
							Cs (km)	**2.5**

ESP	Layer	Age	Depth km	Thickness (h) km	Vp km/s	BD kg/m3	Used BD kg/m3	BD x h
19	Layer	Age	Depth km	Thickness (h) km	Vp km/s	BD kg/m3	Used BD kg/m3	BD x h
	1	Plio-Quaternary	3.8-4.2	0.4	1.8-2.0	1758-1943	1820	728
	2a	Messinian	4.2-4.8	0.6	4.4	2300	2300	1380
	2b	Messinian	4.8-6.0	1.2	4.2	2200	2200	2640
	3a	Pre-Messinian	6.0-8.2	2.2	3.0-4.0	2305-2445	2375	5225
	3b	Pre-Messinian	8.2-9.3	1.1	4.2	2471	2471	2718.1
	3c	Pre-Messinian	9.3-11.1	1.8	4.9-5.1	2558-2583	2571	4627.8
			H (km)	7.3			BD (kg/m3)	2372
							WD (kg/m3)	1030

							MD (kg/m3)	3200
							Cs (km)	**2.8**
ESP	**Layer**	**Age**	**Depth km**	**Thickness (h) km**	**Vp km/s**	**BD kg/m3**	**Used BD kg/m3**	**BD x h**
18	Layer	Age	Depth km	Thickness (h) km	Vp km/s	BD kg/m3	Used BD kg/m3	BD x h
	1	Plio-Quaternary	3.0-5.1	2.1	1.9-4.0	1817-2504	2161	4538.1
	2a	Messinian Halite	5.1-5.45	0.35	4.1	2200	2200	770
	2b	Messinian	5.45-6.0	0.55	4.3	2300	2300	1265
	2c	Messinian	6.0-7.85	1.85	4.6	2400	2400	4440
	3a	Pre-Messinian	7.85-12.3	4.45	3.0-3.2	2305-2335	2320	10324
	3b	Pre-Messinian	12.30-12.9	0.6	4.0	2445	2445	1467
			H (km)	9.9			BD (kg/m3)	2303
							WD (kg/m3)	1030
							MD (kg/m3)	3200
							Cs (km)	**4.1**

The calculated C_s as a function of sediment thickness for the ESP data is also shown in figure 49. It appears that the obtained results substantially agree with the general trend described by the C_s-sediment thickness curves obtained for the different basins.
For the oceanic lithosphere, Hoggard et al. (2017) suggested that a crustal correction should be applied to account for the isostatic replacement of a crustal thickness that differs from a reference crustal thickness with an equivalent water load. Crustal correction, C_c, is given by:

$$C_c=\left(\frac{\rho_a-\overline{\rho_c}}{\rho_a-\rho_w}\right)(z_c-7.1) \qquad 6.3$$

where z_c and $\overline{\rho_c}$ are respectively the thickness and average density of oceanic crust and 7.1 km is the global average crustal thickness after White et al. (1992) that was used to normalize the observed crustal thickness.
Crustal correction as a function of crustal thickness for the studied area is shown in figure 51. The adopted average density of the oceanic crustal is 2860 kg m^{-3} (Carlson and Herrick, 1990). This value is based upon analysis of core material from drilling programs, ophiolitic samples, and the observed seismic velocity structure of oceanic crust. Notice that, for crustal thickness lower than 7.1 km, the crustal correction is negative while it produces subsidence effects for values > 7.1 km.

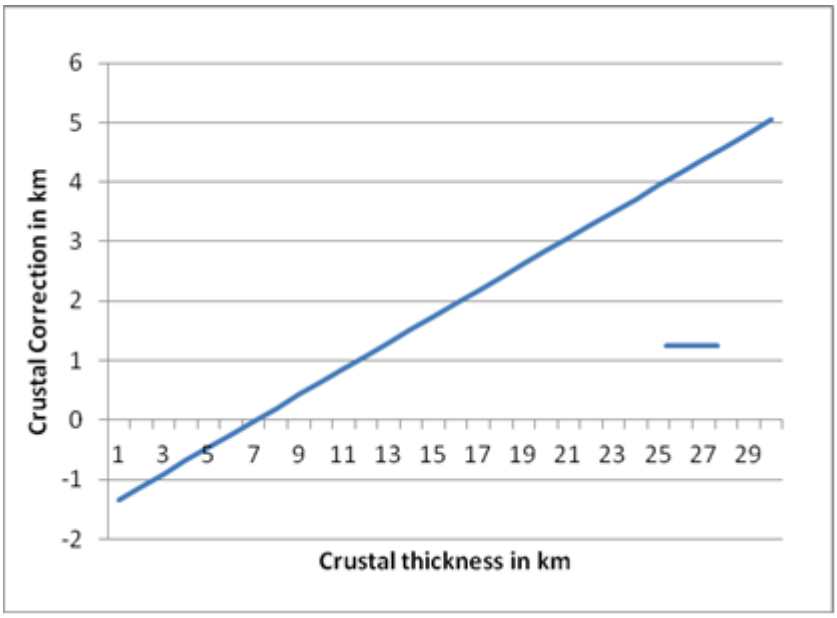

Fig. 51 Crustal correction plotted as a function of crust thickness.

6.2 Water loaded depth (WLD)

WLD is the deepening of the continental/oceanic basement which follows the basin formation and is not related to sediments load, mean sea level change or other external phenomena, but it can be a result of lithosphere stretching and cooling. The seafloor water-loaded depth can be estimated from the actual bathymetry corrected for the sediment load. Calculation implies the knowledge of the thickness of the sediment overlying the crystalline crust (basement).
If sediments were deposited in water at a depth h_w, the true basement depth in the continental crust will be (Fig. 48):

$$WLD_s = h_w + C_s \quad 6.4$$

whereas in the oceanic domain will be:

$$WLD_o = h_w + C_s + C_c \quad 6.5$$

A commonly used technique to analyse the WLD is the modelling of subsidence history developed by Steckler and Watts (1978) that used geological and geophysical observations in deep wells. This methodology is strictly related to the geological-sedimentological information derived from deep wells data. Such data are limited to tectonic structures suspected to be hydrocarbons traps. The calculated WLD can provide results not representative of the whole basin and thus it will be difficult to obtain a regional picture of the area.
In the Eastern Mediterranean basins, information on paleo-bathymetry data is not available and wells data are rather scattered. However, interpretation of seismic profiles and bathymetric charts can provide indirect data for tectonic subsidence

estimation. Such data was made available from global sources and numerous surveys (e.g. de Voogd et al., 1992; Sagy Y., 2016; Gallais et al., 2011; Chamot-Rooke et al., 2005; Dellong et al., 2018)

Another technique can be used to evaluate the lateral variation of WLD on a regional scale for stretching basins that, although giving less precise local results, is applicable on a larger scale. This technique relies on maps of basement depth and detailed seismic profiles (see for example Sawyer, 1985). In this study, I applied this approach which relies on data of sediment thickness and allows obtaining WLD estimations in the EMS.

6.2.1 Sediment and crustal thickness database

Due to the regional character of this study and in the light of the uneven coverage of the available seismic profiles giving detailed information on the crustal structure and composition, data on sediment and crustal thickness in the oceanic domains for the Eastern Mediterranean Sea were extracted from the Crust 1.0 model (https://igppweb.ucsd.edu/~gabi/crust1.html), which incorporates the global sediment thickness database by Laske et al. (2013). In oceanic zones, this global sediment thickness grid was averaged from published digital high-resolution maps and hand-digitized using atlases and maps. For most of the continental areas, the EXXON Tectonic Map of the World (1985) was digitized. This database was obtained from published digital high-resolution maps and hand-digitized atlases and maps and contains data with a 1° x 1° spatial resolution (about 111 x 111 km). 102 data points were investigated within the area of study delimited by coordinates (15.0° E – 35.5° E) and (31.5° N – 38.5° N).
Figure 52 shows the distribution of the sediment thickness in the EMS. We note that the Herodotus Basin shows greater sediment thickness (about 10 km) with respect to the Ionian Basin (about 6 km). This global sedimentary thickness grid has an adequate spatial resolution but is prone to significant error. Errors are observed where thick sedimentary deposits are found, especially adjacent to continental margins, or where significant basement topography is present, besides the inaccurate interpolation between sparse measurements (see for example Hoggard et al., 2017, Winterbourne et al., 2014). Figure 53 shows the crustal thickness map of the EMS. The crustal thickness in the Ionian Basin results thinner than that in the Herodotus Basin.
Since the 102 sites shown in figure 52 might be subject to biases, a number of available seismic profiles was analysed. Figure 54 shows these profiles where additional data points of sediment and crust thickness were inferred.

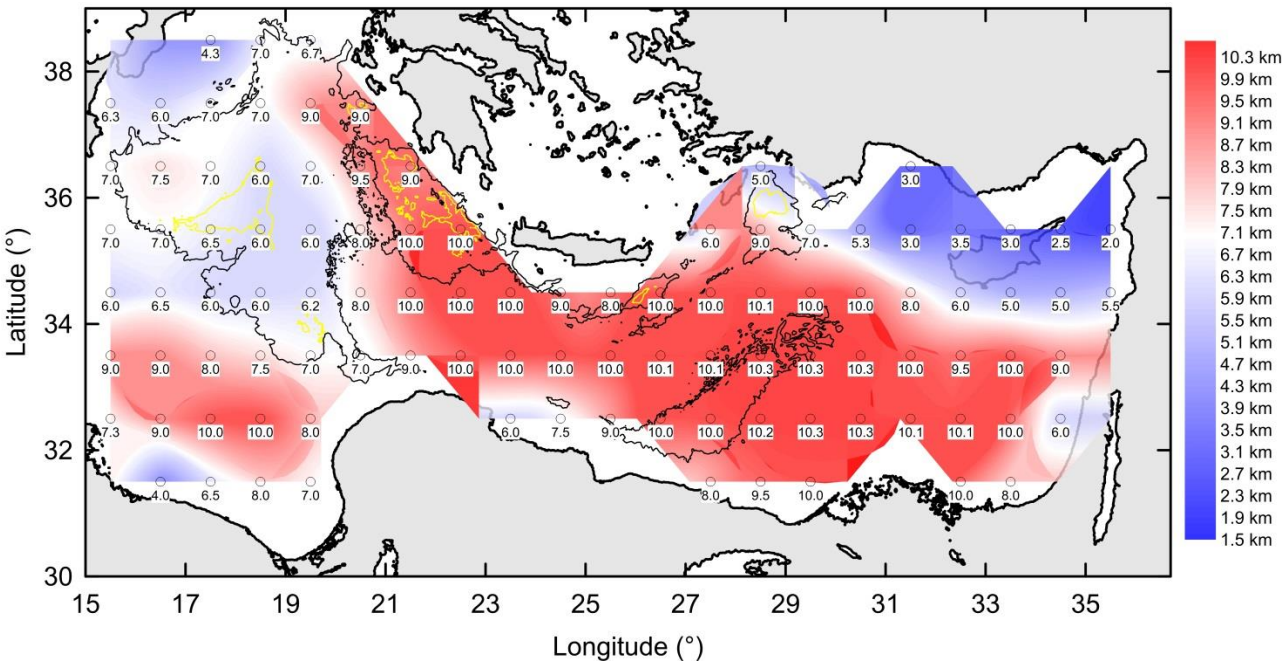

Fig. 52 Sediment thickness map and location of the sites extracted by the Crust 1.0 database. Isobathymetry of -3000 m (black curve) and -4000 m (yellow curve) are indicated.

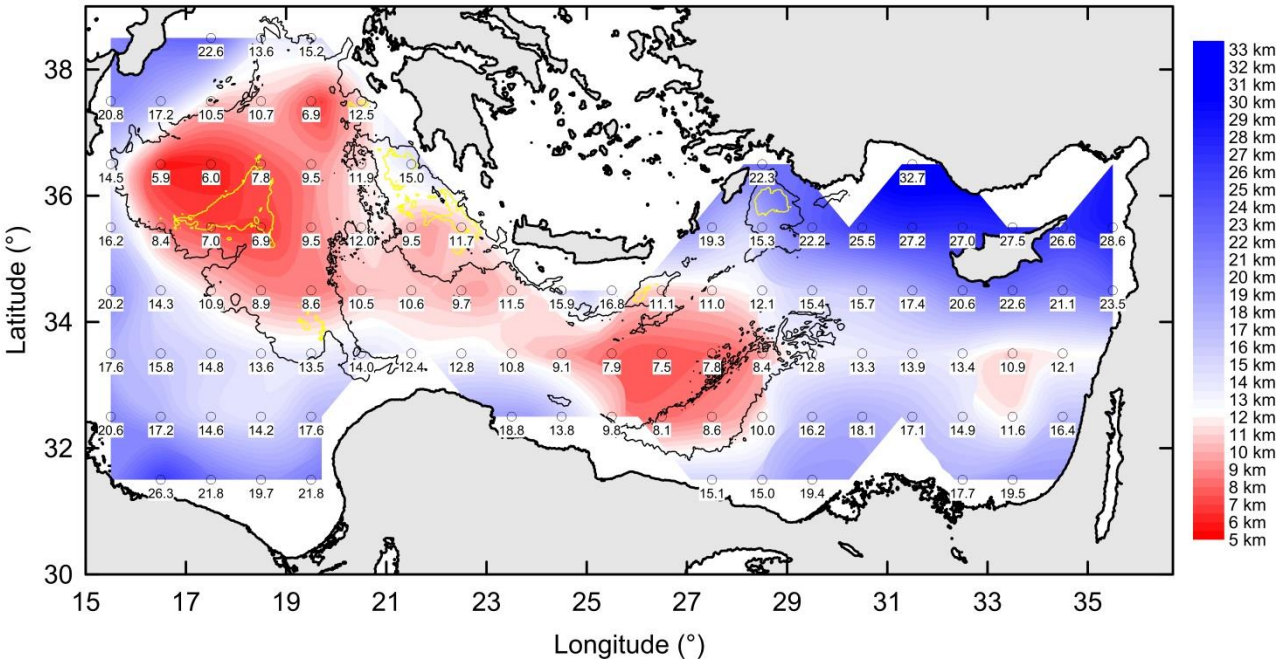

Fig. 53 Crustal thickness map and location of the sites extracted by the Crust 1.0 database. Isobathymetry of -3000 m (black curve) and -4000 m (yellow curve) are indicated.

In the Southeastern MediterraneanSea, Netzeband et al. (2006) processed and analysed two seismic refraction profiles P1 (150 km) and P2 (158 km) and produced two final velocity models from which I extracted a total of 15 data points and 14 data points respectively.

On the other hand, Ben-Avraham et al. (2002) processed and analysed three seismic refraction profiles acquired in 1989 (profile I, 270 km long, profile, II more than 100 km long) and re-evaluated a third profile acquired in 1979 (profile III, 400 km long)

producing velocity depth model along each profile from which I extracted 50 data points.

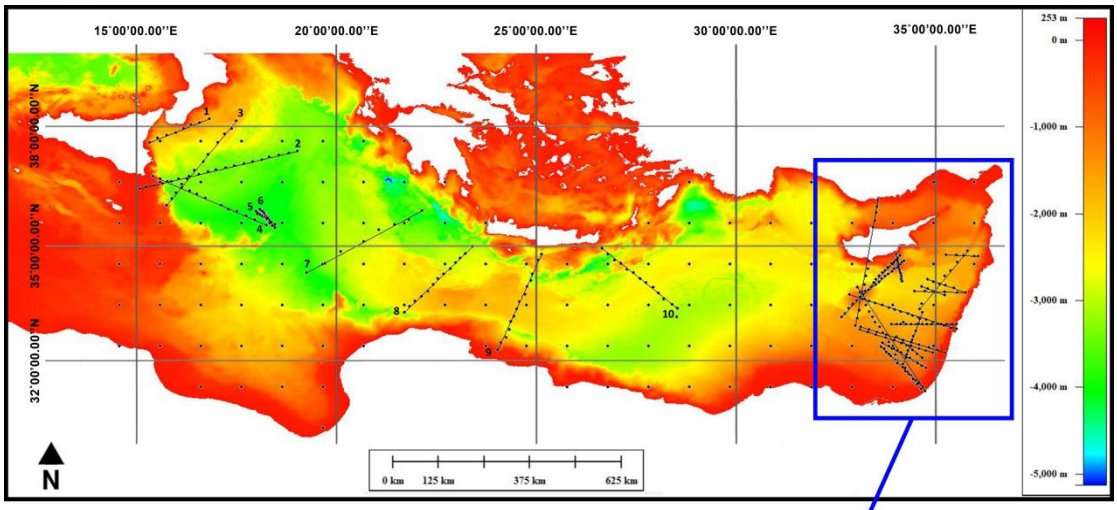

PROFILE NUMBER	PROFILE NAME	AUTHOR
1	DY-P3	Dellong et al., 2018
2	DY-P1	
3	Prof 2	Makris, 1986
4	Prof 1	
5	Archimede 19	Gallais et al., 2011
6	PrisMed 01	
7	IM 05	Chamot-Rooke et al., 2005
8	PR3	Makris, 2006
9	PR4	
10	PR5	

PROFILE COLOR	PROFILE NAME	AUTHOR
Red	Line 1	Welford, 2015
	Line 1A	
	Line 2	
	Line 3	Feld et al., 2017
Dark Blue	P1	Netzeband et al., 2006
	P2	
Green	-	Ben Avraham et al., 2002
Black	EMED 27A, 39, 52, 56	Sagy, 2016
Light Blue	L2, 6, 25, 35, 39	Inati et al., 2017

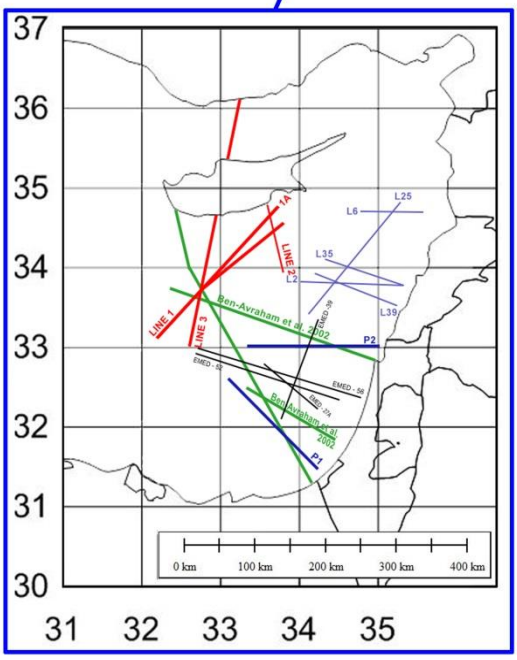

Fig. 54 Seismic profiles used in this study from which sediment and crust thicknesses were extracted. Black dots distributed according to a regular grid from the global crustal model.

In the Northeastern Mediterranean Sea, Feld et al. (2017) processed and analysed seismic data along a 650 km profile (from the Tuz Golu basin in the north to the Eratosthenes Seamount in the south crossing Cyprus) and produced a velocity depth model of which 14 data point were extracted.

Welford et al., 2015 reported the results of wide-angle reflection refraction seismic survey (line 1, 1A and 2 with respectively 200, 150 and 80 km length) used to examine the crustal structures of the Cyprus Arc, Eratosthenes seamount, Hecataeus rise and the Levantine Basin; 48 data points were extracted.

Inati et al. (2017) produced a crustal model of the northern Levant Basin offshore Lebanon based on the interpretation of seismic profiles. Some uncertainties were revealed regarding the detection of the Moho unconformity due to the unreliability of

stacking velocities and the adoption of a mean value from previous findings in the zone. From the corresponding velocity depth models 27 additional data points were added to the database.
Sagy Y. (2016) analysed and interpreted several seismic reflection lines in the Southeastern Mediterranean Sea. Velocity depth models depicted the basement depth from which 36 data points with only sediment thickness were extracted.
Gallais et al. (2011) studied the Miocene tectonic inversion in the Ionian Sea analysing multichannel seismic reflection profiles from which 25 sediment thickness values were extracted and sediment layers thicknesses were separated between Plio-Quaternary, Evaporites and Mesozoic.
Chamot-Rooke et al. (2005) interpreted a deep seismic profile across an accretionary prism and Hellenic backstop in the Western Mediterranean Ridge. Eight crustal and sediment thicknesses were obtained along the profile.
Dellong et al. (2018) studied the crustal structure of the Ionian Basin and Eastern Sicily Margin using a Wide-Angle seismic survey. Twenty-seven values of crustal and sediment thicknesses were deduced.
Makris et al. (1986) from a seismic study in the western Ionian Sea presented schematic structural section along two seismic reflection profiles from which 25 data points of sediment thickness were extracted. In 2006, Makris et al. obtained velocity models from deep seismic profiles between Cretan Sea and Libyan Sea. Forty-one thicknesses values were extracted.
In summary, 334 data points, irregularly distributed over the area of interest, were chosen to integrate the 102 regularly distributed data of sediment thickness inferred from the global dataset.

6.2.2 Results

Figure 55 shows the map of the WLD_s calculated using the eq. (6.4) and considering the bathymetry values presented in section 3. Excluding the high value of WLDs in the trench zones of the Hellenic Arc, generally, the Ionian and Herodotus basins show the highest WLDs in their abyssal plain.

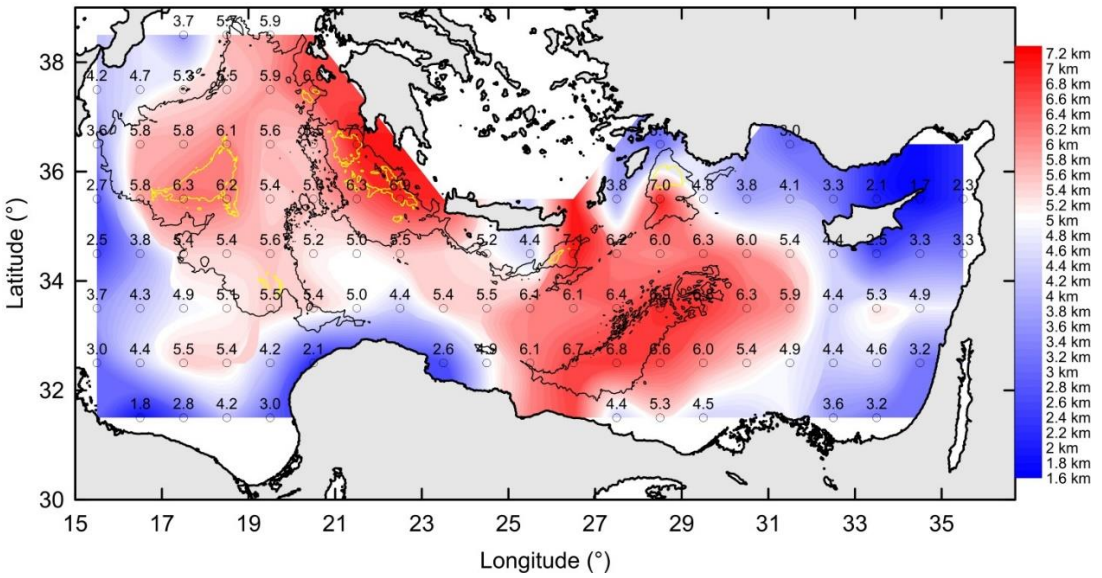

Fig. 55 Map of the sediment corrected water-loaded depth (WLD) and sites of the global dataset (black circle, value in km).

The uncertainty on the WLD estimation is mainly related to errors in bathymetric data and the thickness of the sediment cover. Regarding the bathymetry, a comparison between the dataset used in this study (EMODnet) and other openly available seafloor files, namely ETOPO1 (Amante et al., 2009) and TOPEX (Smith and Sandwell, 1997) shows that the average differences in bathymetry are ~ 50 m. The sediment correction is instead more important. We carried out a preliminary analysis at two specific sites of the Herodotus and Levantine basin wherein detailed seismic information about the sediment thickness are available. In the Herodotus Basin, de Voogd et al. (1992) presented results of the expanding spread profile ESP18 (Fig. 43) indicating a thickness of the whole sediment cover of more than about 1.4 km compared to the Crust 1.0 model. The seismic refraction and reflection records by Netzeband et al. (2006) along the profile P2 of the Levantine Basin (Fig. 2) shows that the sediment thickness of the Crust 1.0 model might be on average < 0.7 km. If we assume that the reference database assumed for this study underestimates the sediment thickness by ~ 1000 m, the uncertainty on the sediment correction, C_s, is of ~ 200 m. In summary, the overall uncertainty due to sediment thickness and bathymetry errors is thus ~ 250 m. Error produced by uncertainties on the density assumed both for Cs and the crustal correction C_c are more difficult to quantify. By considering the typical average sediment thickness of the eastern Mediterranean, according to the error analysis suggested by (Hoggard et al., 2017), the error on C_s can be as large as ~ 200 m whereas it is negligible for C_c.

7. LITHOSPHERE NATURE

The mode of formation and age of the Eastern Mediterranean Sea are still widely debated as well as whether the nature of the lithosphere is continental or oceanic. Among those who attributed an oceanic origin, of Carboniferous age (340±25 Ma) of the Herodotus Basin, one can mention Granot (2016). For the Ionian Basin, others, like e.g., Speranza et al. (2012), based on magnetic anomalies, suggested a Triassic age (220–230 Ma), whereas Stampfli and Borel (2002), based on geological considerations, argued for ages as old as Permian.

I tried to contribute to these issues by analysing the seafloor water-loaded depth (WLD) and the terrestrial heat flow data in comparison to those predicted by continental stretching and oceanic cooling models (e.g., McKenzie, 1978; Le Pichon and Sibuet, 1981; Sawyer, 1985; Pasquale et al., 1994; Verdoya and Chiozzi, 2018; El Jbeily et al., 2019). I particularly focussed on three selected areas to infer the nature and geological age of the lithosphere.

Figure 56 shows the boundaries of the likely oceanic lithosphere in the Ionian and Herodotus Basins and the continental lithosphere in the Levantine Basin. In order to analyse only undeformed areas, I focused on the areas ranked as oceanic in the updated global dataset of oceanic crustal age by Seton et al. (2020). I neglected the zones belonging to the Mediterranean Ridge and Calabrian accretionary prism (after Tugend et al., 2019). In the Ionian Basin, the oceanic area has been extended using the recent data based on seismic studies by Dannowski et al. (2019). In the Levantine Basin, I highlighted the flat portion of the seafloor based on the morphological features.

I analysed WLD for the three selected zone in figure 56. I determined the average WLDs values, using the global dataset and some seismic profiles. In particular, in the Ionian and Herodotus basins the crustal correction was taken into account as these basins should be oceanic. By assuming an average crustal thickness in the Ionian and Herodotus Basins of 7.5, 11.3 km respectively, C_c is about 100 m for the Ionian Basin and 700 m for the Herodotus (Table 18). This implies a further increase of the average estimated water loaded depths. Age data derive from the updated global dataset of oceanic crustal age by Seton et al. (2020). In the Levantine Basin, I assumed an age as proposed by Segev et al. (2018). Table 18 also reports the stretching factor (β-factor), defined as the ratio between the crustal thickness before and after stretching. As in the Ionian Basin, the crust is very thin (on average 7.5 km), β-factor is high about 4.0 depending on the initial crustal thickness of 30 km.

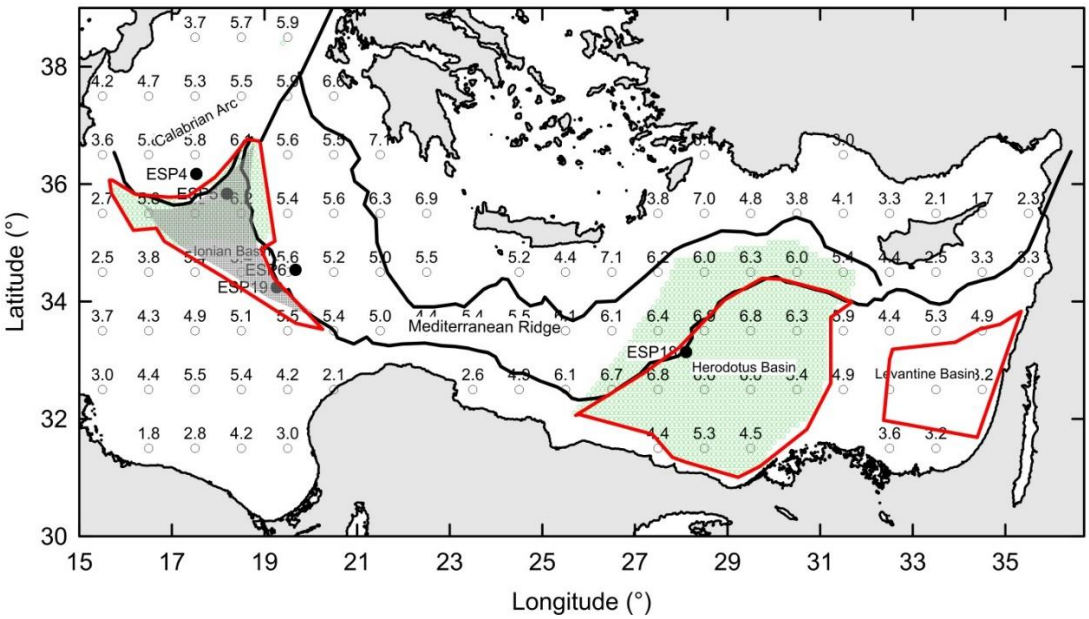

Fig. 56 Location of the sediment corrected water-loaded depth (WLDs) sites (black circle, value in km), the expanding spread profiles (ESPs) central points, recorded during the Pasiphae cruise (black full circle), the limits of Calabrian Arc and Mediterranean Ridge by Tugend et al. (2019), the undeformed oceanic lithosphere (grey area) in the Ionian Abyssal Plain by Dannowski et al. (2019) and the oceanic crust (green zones) by Seton et al. (2020). Red polylines delineate the WLD analysis selected zones for the three main sedimentary basins.

Table 18 Values of the mean WLD_s, crustal correction (C_c), corrected WLD_o for crustal thickness, stretching factor (β) and geological age of the Ionian, Herodotus and Levantine basins.

Basin	**Sites/Datasets**	**WLD_s (km)**	**h_c (km)**	**C_c (km)**	**WLD_o (km)**	**β**	**Age (Ma)**
Ionian	2 ESP, 5 global datasets and 3 seismic profiles	5.8 (0.3)	7.5 (0.9)	0.1 (0.1)	6.0 (0.3)	4.0 (0.5)	220-230
Herodotus	1 ESP, 15 global datasets and 1 seismic profile	6.5 (0.3)	11.3 (3.7)	0.7 (0.6)	7.2 (0.3)	2.5 (0.7)	340±25
Levantine	4 global datasets and 5 seismic profiles	3.9 (0.5)	N/A	N/A	N/A	2.5 (0.4)	95-125

7.1 WLD of the continental lithosphere

As a first step, I checked whether WLD values fit a continental lithosphere pure-shear stretching (McKenzie, 1978). The model envisions a first stage, represented by thinning of the crust and lithospheric mantle, and by asthenosphere upwarping. Contemporaneously, initial subsidence by isostatic rebound takes place, because of the density change resulting from stretching and temperature increase of the uppermost mantle. Subsequently, a passive process caused by the lithosphere comeback to thermal equilibrium, with consequent lithosphere contraction, results in long-term thermal subsidence. Stretching is assumed instantaneous and uniform, and the lithosphere thickness H is reduced by a factor β.

If the compressibility effect on of the crust, ρ_c, and lithospheric mantle, ρ_H, density is neglected, the initial subsidence WLD_i is given by (Le Pichon and Sibuet, 1981; Pasquale et al., 1994):

$$WLD_i = \frac{H\rho_a - h\rho_c - (H-h)\rho_H}{\rho_a - \rho_w}\left(1 - \frac{1}{\beta}\right) \qquad 7.1$$

with H the lithosphere thickness and $\rho_c = \rho_{co}\left(1 - \frac{\alpha}{2}T_a\frac{h}{H}\right)$, $\rho_H = \rho_m\left(1 - \frac{\alpha}{2}T_a - \frac{\alpha}{2}T_a\frac{h}{H}\right)$, where ρ_{co} is crust density at room temperature and *h* the crust thickness. At the infinite time, the lithosphere attains thermal equilibrium with a maximum WLD expressed by

$$WLD_\infty = h\frac{\rho_H - \rho_c + \rho_m(\alpha/2)T_a + \varepsilon}{\rho_a - \rho_w}\left(1 - \frac{1}{\beta}\right) \qquad 7.2$$

where $\varepsilon = -\frac{\rho_m - \rho_{co}}{\beta}\left(\frac{\alpha h}{2H}T_a\right)$ can be neglected since it yields an error on the order of 0.5%.

The assumed values for h, H, ρ_{co}, ρ_m, ρ_w, α and T_a are listed in table 19. It follows that eq (7.1) becomes:

$$WLD_i = 3.4\left(1 - \frac{1}{\beta}\right) \qquad \text{[km]} \qquad 7.4$$

and eq (7.2)

$$WLD_\infty = 7.3\left(1 - \frac{1}{\beta}\right) \qquad \text{[km]} \qquad 7.5$$

As the thermal subsidence follows approximately an exponential law with a time constant $\tau = H^2\pi^{-2}\chi^{-1}$, for a continental lithosphere with thermal diffusivity χ = 32 $m^2\ a^{-1}$, the water-load depth as a function of time and stretching factor, WLD_s, is obtained by combining eq (7.4) and (7.5)

$$WLD_s = \left[3.4 + 3.9\left(1 - e^{\frac{t}{\tau}}\right)\right]\left(1 - \frac{1}{\beta}\right) \qquad \text{[km]} \qquad 7.6$$

By assuming the parameters of table 19, variations of WLD_s at the initial and infinite time as a function of β were calculated (Fig. 57).

Table 19. List of parameters used in calculations

Symbol	Value	Reference
ρ_w	1030 kg m^{-3}	-
ρ_m	3300 kg m^{-3}	Hoggard et al. (2017)
ρ_{co}	2780 kg m^{-3}	Le Pichon and Sibuet (1981)
α	3 10^{-5} $°C^{-1}$	Hoggard et al. (2017)
T_a	1330 °C	Hoggard et al. (2017)
h	30 km	Netzeband et al. (2006)
H	125 km	Schütz et al. (2014)

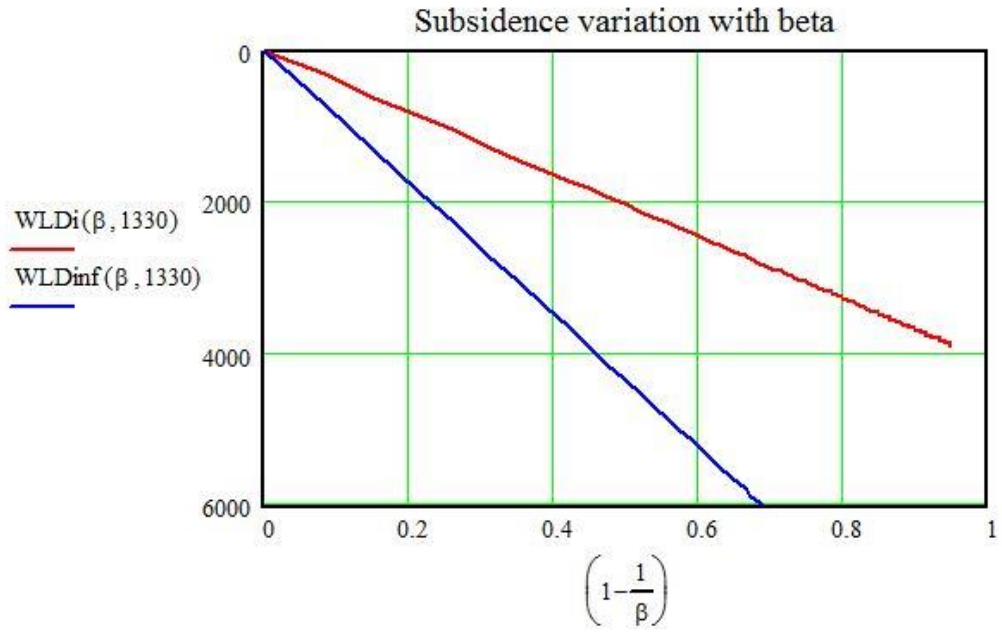

Fig. 57 Initial (WLDi) and infinite (WLDinf) variation as a function of stretching factor β.

Curves of WLD_s as a function of β calculated at different geological times since rifting using equation 7.6 are shown in figure 58, together with the WLD_s values of the undeformed sectors of the Ionian, Herodotus and Levantine basins (Table 18). After ~ 200 Ma, the stretched lithosphere is nearly in thermal equilibrium and thus WLD no longer increases with time and is nearly WLD_{inf}.

WLDs in the Levantine Basin are in good agreement with the predicted value for an age of 95-125 Ma for a stretching factor spanning from 2.1 to 2.9. WLD_s data of Herodotus and Ionian basins are significantly larger than the WLD_{inf} curve. In the Herodotus, WLD_s exceeds 2.2 km that predicted by the continental stretching model and indicate a stretching factor of 1.8-3.2. WLD_s of the Ionian Basin slightly exceed by about more than 0.5 km the water-loaded depth predicted by the model and the corresponding stretching factor is 3.5-4.5.
It must be stressed that when β is greater than 3.2, the asthenosphere material should be able to rise for lithostatic pressure and to break through a thinned continental crust

to form a new crust of oceanic type (Le Pichon and Sibuet., 1981; Sawyer, 1985; Pasquale et al., 1994). Such considerations indirectly argue for an oceanic nature of the lithosphere in the Ionian and Herodotus basins

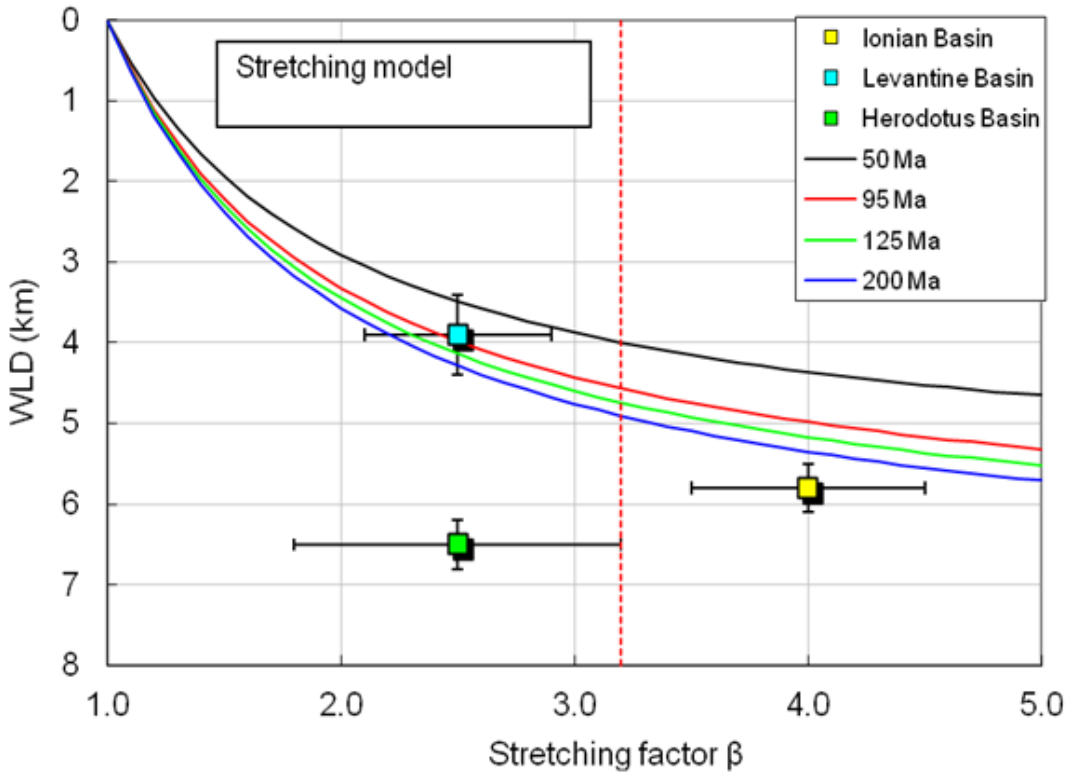

Fig. 58 WLD of a rifted continental lithosphere as a function of stretching factor β calculated at different geological times since rifting. Yellow, green and light blue squares are mean values of Water-Loaded Depth (without crustal correction) and the correspondent stretching factors. of the Ionian, Herodotus and Levantine basins, respectively. Bars are standard deviations.

The stretching factor I estimated from WLDs of the Levantine Basin is consistent with a factor β of 2.3-3.0 suggested by Netzeband et al. (2006) based on seismic data. Despite the reduced crustal thickness still records lithosphere stretching that affected the area, this basin has likely reached thermal equilibrium and therefore there is no evidence of extension in the surface heat flow.

7.2 Oceanic lithosphere and residual depth anomaly

Based on the plate or half-space cooling models, several relationships between WLDs and the oceanic crust age were suggested from global-scale observations (e.g. Parsons and Sclater, 1977; Stein and Stein, 1992; Crosby et al., 2006). A recent study by Hasterok (2013) argues that the plate model provides a better explanation for the water-load seafloor depth and heat flow of oceanic lithosphere as a function of time. According to this model, the water-load seafloor depth of oceanic lithosphere, WLD_o, is (Turcotte and Schubert, 2002):

$$WLD_o = d + \left(\frac{\rho_m \alpha T_a H_o}{2(\rho_m - \rho_w)} \right) \left\{ 1 - \frac{8}{\pi^2} \sum_{n=0}^{\infty} \frac{1}{(1+2n)^2} \exp\left[\frac{-\chi(1+2n)^2 \pi^2 t}{H_o^2} \right] \right\} \qquad 7.7$$

where d is the zero-age depth, H_o is the thickness of the oceanic lithospheric plate, t is time and n is an integer value.

Using the global database of ship track bathymetry by Crosby and McKenzie (2009), Hasterok (2013) offered the following simple approximation to calculate WLD_o (in m):

$WLD_o(t)=$

$$\begin{cases} 2514 + 414.5\sqrt{t} & t \leq 17.4 \text{ Ma} \\ 2514 + 3109 - 2520e^{-0.034607t} & t > 17.4 \, Ma \end{cases} \qquad 7.8$$

Differently from previous age-depth syntheses the curve described by eq. (7.8) is not biased towards regions with negative dynamic topography and/or with an anomalously thickened crust that were excluded in the Crosby and McKenzie database. For example, Parsons and Sclater (1977) deliberately maximized depth estimates for ages greater than 60 Ma in order to demonstrate that oceanic plates do not subside by half-space cooling. In contrast, Stein and Stein (1992) did not excise regions with thickened oceanic crust, which biases their age-depth estimates toward shallow values.

Figure 59 shows the cooling plate model (eq. 7.8) that fits better the bathymetry dataset of Crosby and McKenzie (2009). For ages greater than 150-160 Ma the WLD_o results of the order of 5600 m. To compare our WLDs estimated in the Ionian and Herodotus basins with those predicted by the plate-cooling model first one must adjust for crustal corrections (see section 6.1), then the basin formation age has to be chosen (Table 20). The latter is provided by different papers, namely Seton et al. (2020) who used the results obtained by Speranza et al. (2012) in the Ionian Basin and Granot (2016) in the Herodotus Basin. The first interpreted the magnetic anomalies of the Ionian Sea based on a compilation of different sources. They proposed a Triassic age (220–230 Ma). Granot (2016) described a sequence of two lineated anomalies and found that the skewness of the anomalies implied a 340 ± 25 Ma Early Carboniferous age.

It appears that WLD_o data in the Ionian and Herodotus oceanic areas do not fit the reference oceanic curve, being higher than expected (Fig. 59; see also Table 20). In particular, WLD_o in the Herodotus Basin exceed by 1600 m the subsidence of the cooling plate model and this involves a negative residual depth anomaly.

Table 20 Values of the mean observed $_{WLDs,}$ crustal correction (C_c), corrected WLD_o and residual depth R_d in the Ionian and Herodotus basins. hc is the crustal thickness proposed by the CRUST 1.0 model. Oceanic crustal age by Speranza et al. (2012) (*) and Granot (2016) (**).

Basin	WLD_s (km)	h_c (km)	C_c (km)	WLD_o (km)	R_b (m)	Age (Ma)
Ionian	5.8 (0.3)	7.5 (0.9)	0.1 (0.1)	6.0 (0.3)	-400	220-230*
Herodotus	6.5 (0.3)	11.3 (3.7)	0.7 (0.6)	7.2 (0.3)	-1600	340±25**

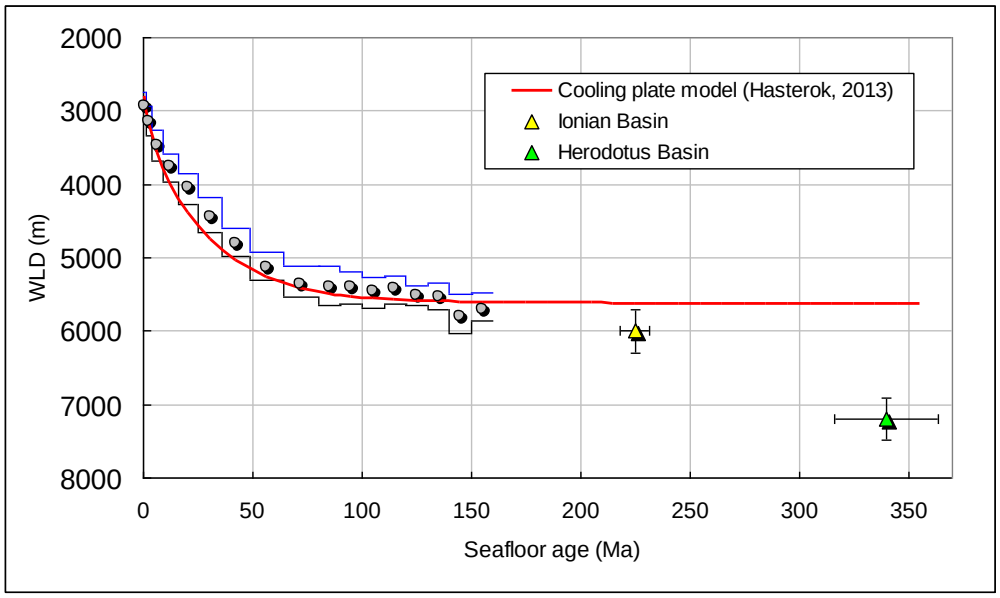

Fig. 59 Average WLD of the Ionian and Herodotus basins after sediment and crustal corrections versus seafloor age (see Table 22) and best-fitting plate cooling model (red curve) by Hasterok (2013). Thin blue and black lines are the upper and lower quartile values while grey full circles are WLD median values after Crosby and McKenzie (2009). Yellow and green triangles are calculated WLD values in the Ionian and Herodotus Basins respectively.

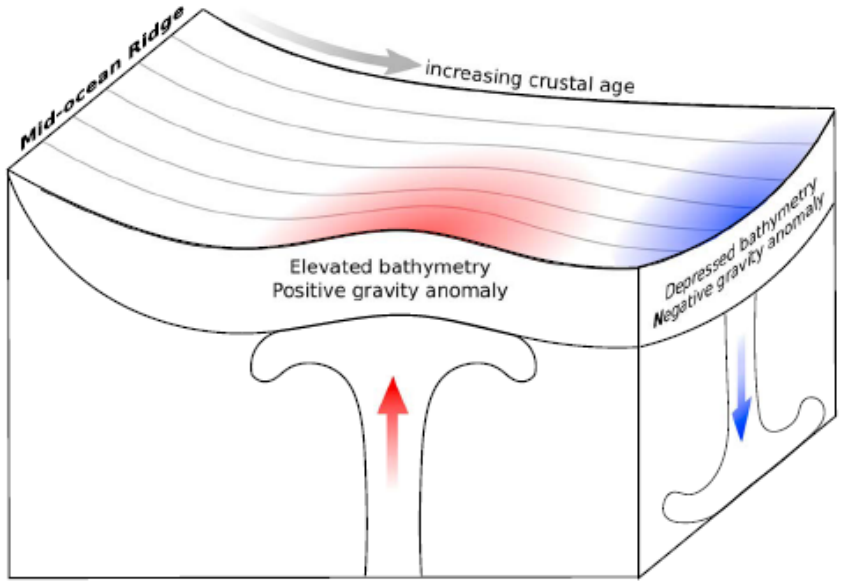

Fig. 60 The general increase in plate thickness with age is controlled by the cooling and thickening of the lithosphere mantle. Negative and positive depth anomalies are caused by convective upwellings and downwellings, respectively. The red arrow indicates convective upwelling and its surficial manifestation whereas the blue arrow indicates convective downwelling and its surficial manifestation (after Winterbourne et al., 2014).

It is helpful to examine empirically the correlation between residual depth anomalies and free-air gravity anomalies. The quality of these correlations enables us to assess the extent to which residual depth anomalies are generated by dynamic processes beneath the lithospheric plate. The plate model shows the relationship between plate

subsidence and age in regions, where dynamic topography effects are expected to be negligible. In a strict sense, dynamic topography is the deflection of the Earth's surface in response to normal stresses, which are generated by flow within the convecting mantle (Fig. 60). The regional age-depth observations in the Ionian and Herodotus basins compared to the predicted model indicate negative anomalies that have several possible explanations.

Figure 61 shows gravity anomalies from GOCE (Bruinsma et al. 2014) whose wavelengths are larger than 300 km. Long-wavelength free-air gravity anomalies can be regarded as a crude proxy for subplate density anomalies (McKenzie, 2020). Shorter wavelengths caused by flexural and edge effects at plate boundaries and continental margins have been removed from this map.
Long-wavelength gravity data suggest that, except for part of the Ionian Sea, the Eastern Mediterranean Sea is far from being isostatically compensated and that the region contains some of the largest long-wavelength gravity anomalies on Earth. In general, the distribution of positive and negative gravity anomalies matches the elevations and depressions in the topography, which suggests topographic contrasts supported by mantle convection are important throughout the region (see Howell et al., 2017).

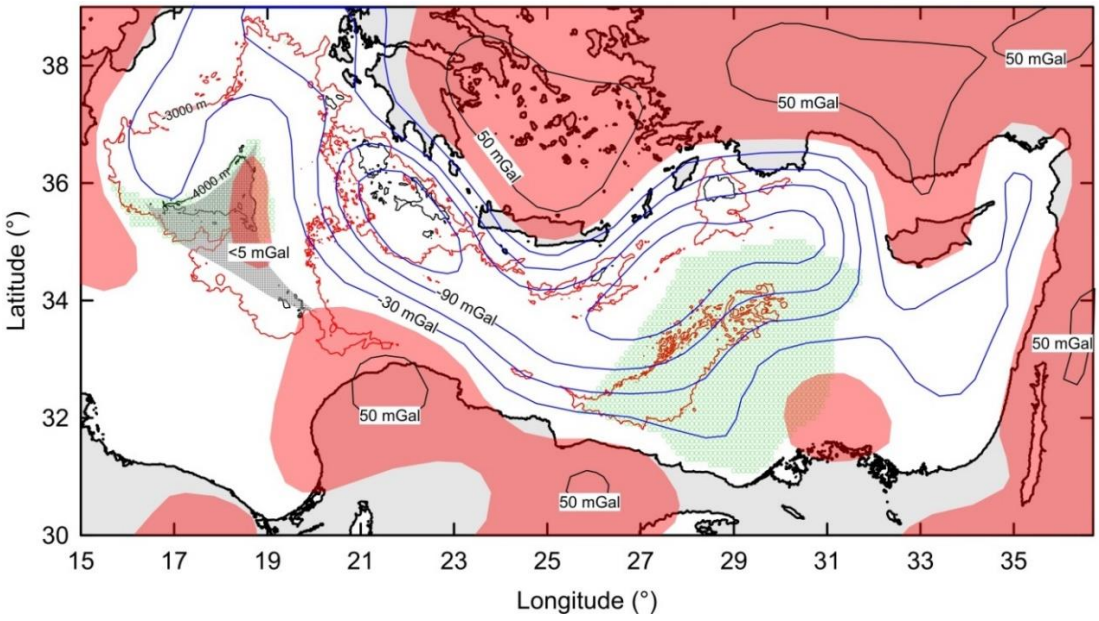

Fig. 61 Gravity anomalies from GOCE with wavelengths larger than 300 km (after, McKenzie, 2020). Areas with a positive anomaly in red; blue contours indicate negative values plotted every -30 mGal (~-1 km of dynamic topography) Bathymetry (in m) is derived from the global seafloor database V18.1 (Smith and Sandwell, 1997), from satellite altimetry and ship depth soundings (http://topex.ucsd.edu/cgi-bin/get_data.cgi). The oceanic lithosphere (light green hatch) by Seton et al. (2020) is also indicated. Gray area marks the presence of oceanic lithosphere below the seafloor in the Ionian Basin (undeformed portion) as determined by seismic studies (Dannowski et al., 2019).

In the Herodotus Basin, the free-air gravity anomaly (from -30 to -90 mGal) is larger than in the Ionian Basin (0-30 mGal). This agrees with the residual depth anomaly I have determined in the two basins (Table 20; Fig. 59).

In the oceans, dynamic topography in a broad sense can be estimated from these anomalies for an admittance value, z = 30 ± 10 mGal km^{-1}, which is appropriate for wavelengths of greater than 800 km (e.g., *Crosby et al.*, 2006; *Crosby and McKenzie*, 2009). Consequently, the values of residual depth anomaly determined by the cooling plate model are in the range of those determined with free-air gravity anomaly.

These results are in good agreement with those obtained by Winterbourne et al. (2014). Using a different sediment loading correction, reference cooling plate model, free-air gravity dataset and only the ESP sites by de Voogd et al. (1992), these authors drew a transect crossing the area of interest (Fig. 62).

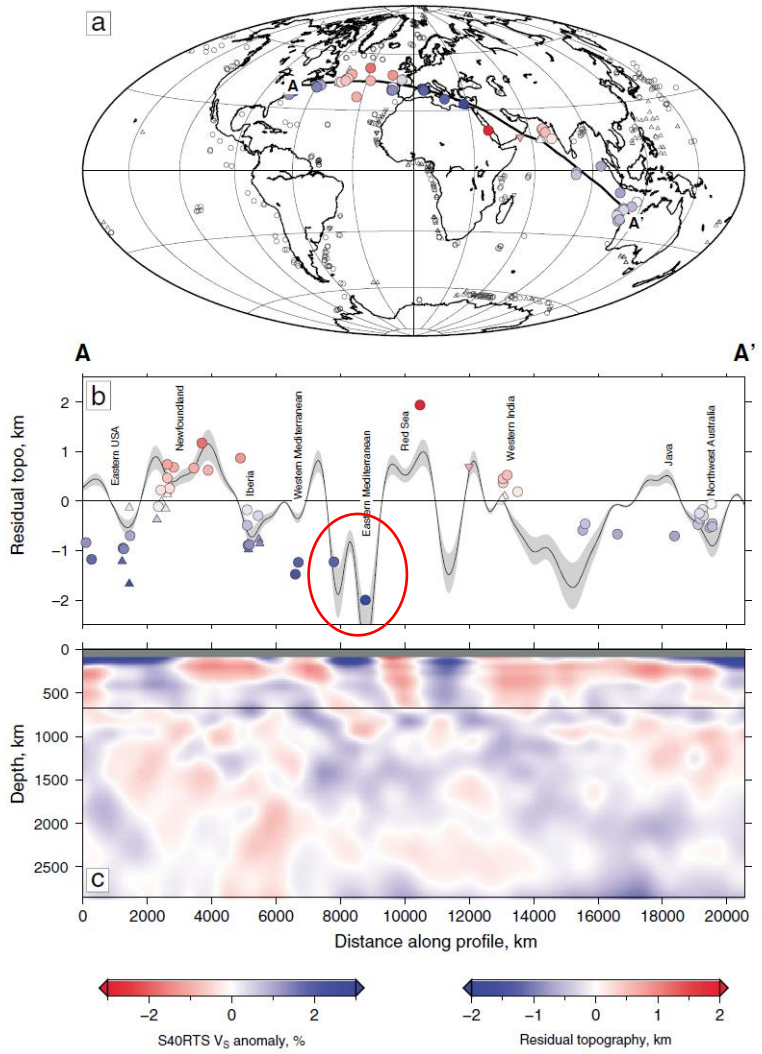

Fig. 62 (a) Traverse, A-A′, showing the variation of residual depth for oceanic crustal fragments from Northwestern Australia to the East coast of North America. Coloured circles = estimates of residual depth made from oceanic crust; Note scale at the bottom right-hand side. (b) Residual plotted as a function of distance along A-A′. Circles as above; black line with grey band = residual depth predicted from long-wavelength free-air gravity anomaly, assuming Z = 20–40 mgal/km. (c) Vertical slice from S40RTS seismic tomographic model of *Ritsema et al.* [2011]. Note scale at the bottom left-hand side. Horizontal line = 670 km discontinuity. Grey band marks top 100 km (i.e., lithosphere).

Along this transect, the Eastern Mediterranean Sea has negative residual depths and gravity anomalies which are matched by upper mantle velocity anomalies. In particular, residual depth bathymetry is negative in the Eastern Mediterranean Sea with values of about -1 km to -2 km in the Ionian and Herodotus Basins respectively. These variations are closely matched by long-wavelength gravity anomalies.

7.3 Heat flow of the oceanic lithosphere

To analyse the heat flow data of the Ionian and Herodotus basins, I applied the cooling model for the ocean plate by Hasterok (2013). This model was re-calibrated to a new "hydrothermal-free" heat flow dataset to provide a better fit to heat flow on old (>80 Ma) seafloor while simultaneously allowing for a more reasonable mantle potential temperature (1350 °C). The best-fitting plate model resulted in a lithosphere with a thickness of 90 km. Since it resolved the longstanding inability to explain high heat flow on an old lithosphere, it represents a significant improvement over previous plate models by providing an accurate prediction of terrestrial heat flow.

The simple approximation for surface heat flow q(t) (in mW m^{-2}) is given by

$$q(t) = \frac{506.7}{\sqrt{t}} \quad \text{for } t \leq 48.1 \text{ Ma} \qquad 7.9$$

$$q(t) = 53+106\, e^{-0.034607t} \quad \text{for } t > 48.1 \text{ Ma}$$

This model predicts a heat flow of ~ 50 mW m^{-2} for the age of the oldest oceanic lithosphere (~180 Ma). The Ionian and Herodotus basins estimated age is much older than the oldest oceanic crust. Thus, a comparison of the heat flow of the Ionian and Herodotus basins with the reference model is not so straightforward as the age of the lithosphere beneath the two basins is much larger than the range of age used for calibrating the cooling plate model.

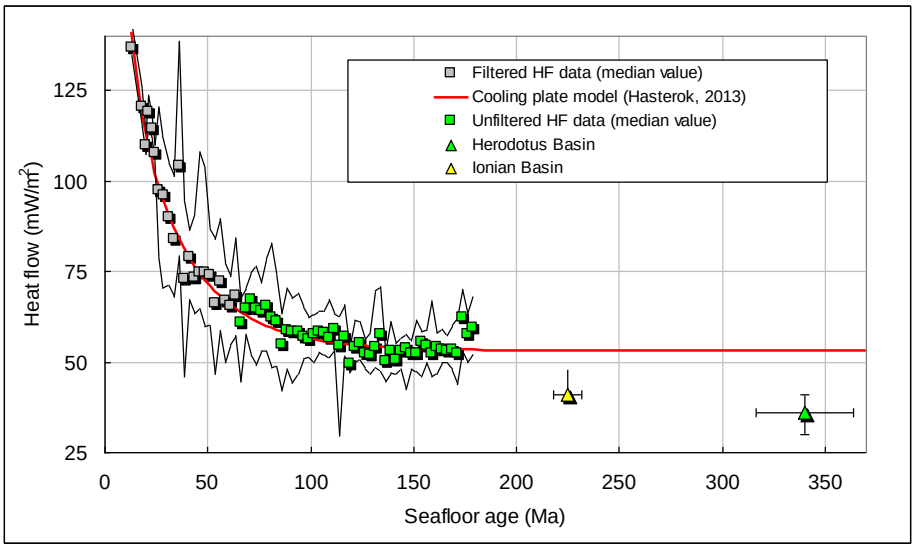

Fig. 63 Reference cooling plate model (red curve) and median heat flow dataset including globally unfiltered and filtered data binned by seafloor age (Hasterok, 2013). Black lines indicate interquartile ranges. Full triangles indicate median heat flow values in the oceanic area in the Ionian and Herodotus basins.

However, it seems that the average heat flow values of the two basins are smaller by 12-17 mW m^{-2} to the reference value predicted by the cooling plate model (Fig. 63). The low heat flow in the Ionian and the Herodotus might indicate that the lithosphere is anomalously colder than the oldest oceanic crust. In general, the combination of the large subsidence and low heat flow suggests that the lithosphere under the abyssal plain of large sectors of the Eastern Mediterranean Sea may be anomalously cold.

Provided that the lithosphere of the Ionian and Herodotus basins is oceanic, their thermal pattern exhibits similarities to that of the Gulf of Mexico, in which anomalously low heat flow was observed as well (Nagihara et al., 1996). These oceanic lithospheres might be the only older lithosphere that somehow has survived subduction and cooled without being substantially reheated. Possible hypotheses imply either these regions have escaped reheating by small-scale convection or that this convective mechanism does not hold for all ocean lithospheres.

7.4 Possible thermal structure of the lithosphere

The cooling plate model implicitly argues that for a lithosphere age of 180 Ma, thermal equilibrium is likely to have occurred. Therefore, I calculated a conductive lithosphere geotherm, under the assumption of steady-state conditions. I modelled the thermal structure of the Ionian lithosphere, for the number of heat flow data is larger than in the Herodotus basin. This allowed me to better constrain the thermal model. I also considered the thermal conductivity dependence upon pressure and temperature (e.g., Chiozzi et al., 2017; Chiozzi et al. 2021).
Figure 64 shows the modelled geotherm. A terrestrial heat flow of 39-48 mW m^{-2} and surface temperature of 13°C were assumed as boundary conditions. The crustal radiogenic heat was assumed uniform in the crust and upper mantle (values shown in Fig. 64). The crustal radiogenic heat production was estimated from the seismic structure as inferred from the expanding spread profile (ESP5) by de Voogd et al. (1992). By assuming heat-production values as suggested by Verdoya et al. (2021) and Inati et al. (2016) for the sediments, and by Pasquale et al. (2005) for the oceanic crust, the inferred crustal contribution to the surface heat flow in the Ionian Basin is about 3 mW m^{-2}. This leads to an estimated mantle heat flow of about 36-45 mW m^{-2}.

From the lithospheric temperatures, we can estimate the thickness of the thermal lithosphere beneath the Ionian Basin, defined as the depth at which the extrapolated conductive geotherm would intersect that of the convective interior (Priestley and McKenzie, 2006). The mantle potential temperature was assumed to range from 1300 to 1400 °C (Herzberg et al., 2007) and an adiabatic gradient of 0.3 mK m^{-1} was

considered in the sub-lithospheric mantle (Thompson, 1992). It turns out that the lithosphere-asthenosphere boundary (LAB) can as deep as 115-150 km (Fig. 64).

There have been several local studies of seismic wave propagation in the Eastern Mediterranean Sea region (see for example Priestley et al., 2019; Schaeffer and Lebedev, 2013; El-Sharkawy et al., 2020 and reference therein). Figure 65 shows the lithosphere thickness map recently proposed by McKenzie (2020), which reports an extensive region of thick lithosphere, beneath the Eastern Mediterranean Sea. In the early low-resolution tomographic models this anomaly was thought to be a result of the high velocities within the cold sinking slab beneath the Aegean, even though its location was south of the Hellenic Arc. However, as the resolution of the tomographic models has improved, it has become clear that this feature is indeed south of the Arc. This extensive region of thick lithosphere, beneath the Eastern Mediterranean Sea, is also the region of negative gravity anomalies (see Fig. 61). This thick lithosphere is perhaps the most enigmatic structure in the whole Mediterranean area. It is present in all tomographic models from surface waves (see e.g. McKenzie, 2020 and reference therein).

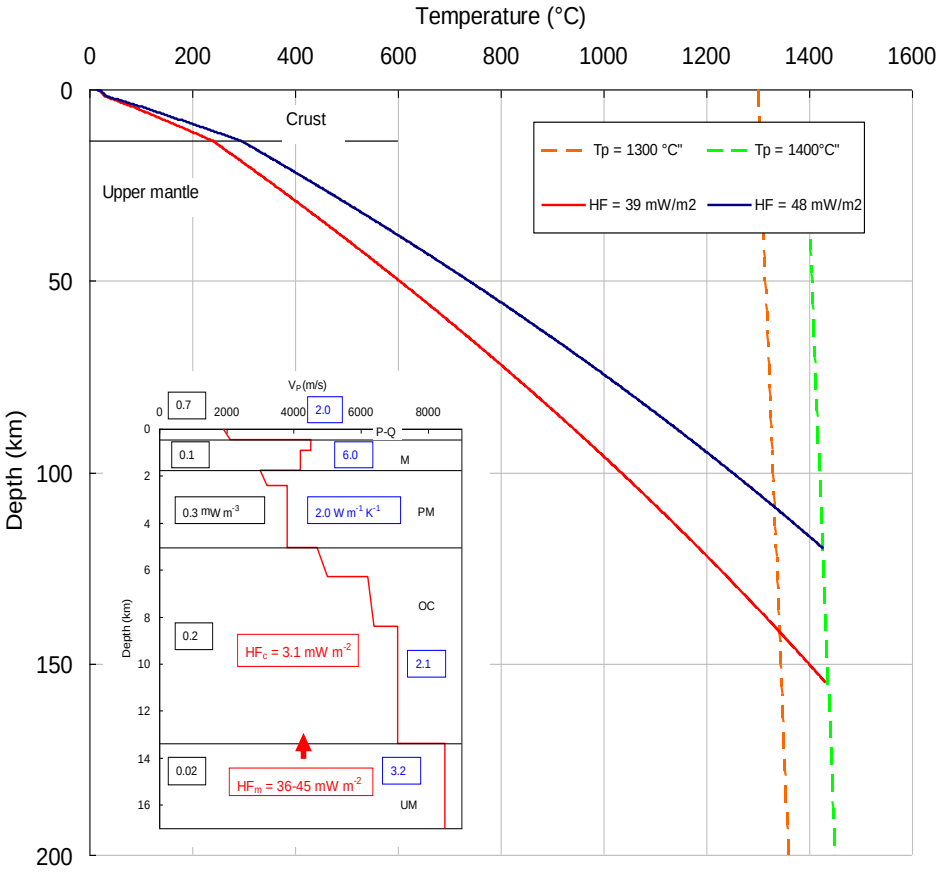

Fig. 64 Geotherms of the Ionian Basin lithosphere calculated with the approach described by Chiozzi and Verdoya (2017) for a surface heat flow of 39 and 48 mW m^{-2} (continuous blue and red, respectively). Mantle adiabats (dashed red and green line), corresponding to potential temperatures T_p of 1300 and 1400 °C, are superimposed. In the inset, crustal heat flow (HF_c) and mantle heat flow (HF_m) as inferred from the compositional model derived from p-wave velocity data (red line) of ESP5. The radiogenic heat production (black label) and thermal conductivity (blue label of each layer are

given. Plio-Quaternary (P-Q), Messinian (M), Pre-Messinian (PM) sequences, OC = oceanic crust, UM = upper mantle.

This reinforces the result we obtained based on heat flow observations. The low terrestrial heat flow of the Ionian Basin is compatible with an old, thick oceanic lithosphere that has reached thermal equilibrium.

7.5 Possible alternative interpretations: the half-space cooling model

As explained in section 7.2, the WLD of the Eastern Mediterranean basins is much deeper than the reference inferred from the plate model. This negative residual depth could be interpreted as dynamic topography.

Alternatively, in the oceans, the WLD can be well predicted up to an age of about 90 Ma by considering the cooling of a semi-infinite half-space. In this case, the depth increases as the square root of time from the ridge crest. After 90 Ma, the ocean floor does not appear to deepen significantly. This absence of deepening has been interpreted in terms of a finite thickness of the oceanic plate, which implies that the basal temperature is being maintained, presumably by some sort of small-scale boundary layer convection. This is quite reasonable for open oceans.

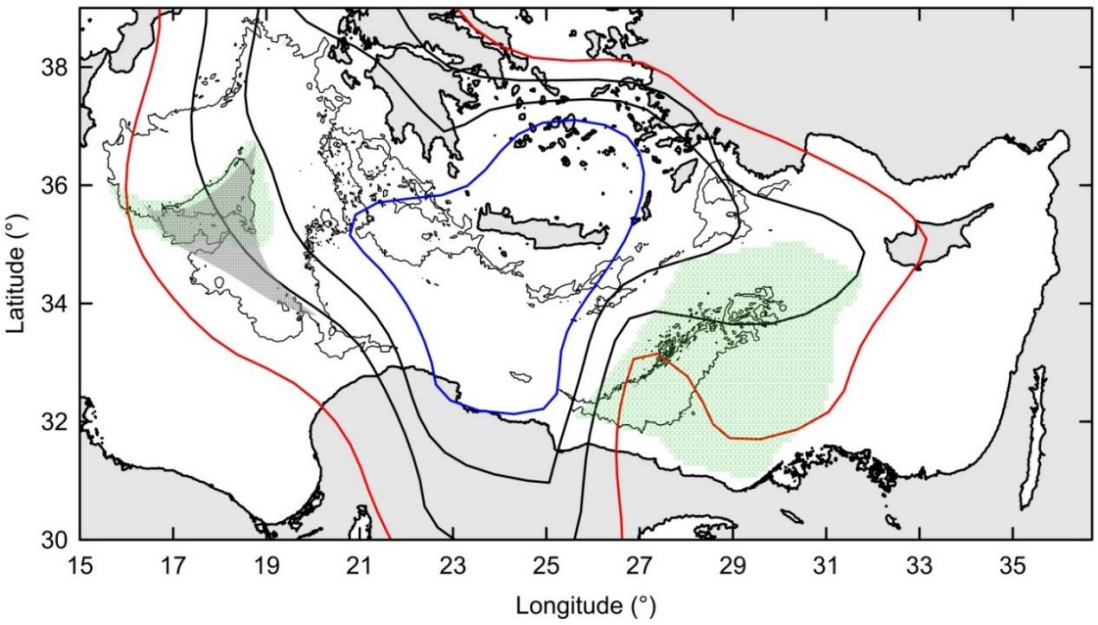

Fig. 65 Lithospheric thickness, estimated from Priestley et al.'s (2019) model of surface wave tomography (after McKenzie, 2020). The lithospheric thickness model is available from http://ds.iris.edu/ds/produ cts/emccam2016. Red and blue curves indicate isolines of 100 and 160 km, respectively. The limits of the oceanic lithosphere (light green hatch) by Seton et al. (2020) are also indicated. Grey area marks the presence of oceanic lithosphere below the seafloor in the Ionian Basin (undeformed portion) as determined by seismic studies (Dannowski et al., 2019).

As suggested by Nagihara et al. (1996) for the Gulf of Mexico, small scale convection might be inapplicable to narrow basins such as the Eastern Mediterranean Sea. The Eastern Mediterranean Sea might be pulled down by underlying asthenospheric circulation. Another explanation for the lack of small-scale convection might simply

lay in the fact that the Eastern Mediterranean Sea is narrow and surrounded by continental lithosphere on both sides. In this context, the small-scale boundary layer convection that maintains the temperature at the base of the oceanic lithosphere may not be initiated and the semi-infinite half-space cooling law may apply to much larger ages.

Using the same observed WLD and heat flow database of the plate cooling model, Hasterok (2013) implemented the half-space cooling model. The simple approximation for surface heat flow q(t) (in mW m^{-2}) and WLD (in m) are given by:

$$q(t) = 521\ t^{-1/2} \quad (8.5)$$

$$WLD(t) = 2514 + 331\ t^{1/2} \quad (8.6)$$

respectively, where t is the lithosphere age in Ma.

Figures 66 and 67 show WLD and heat flow versus age as predicted by the half-space cooling models. There is a deviation in both models with higher values than the half-space model. WLD results in both basins about 1.5 km greater than the reference one. Heat flow in both basins is about 6-8 mW/m^2 larger than the reference one, but they are closer to the half-space rather than the plate cooling model which exhibits differences of 12-18 mW m^{-2}.

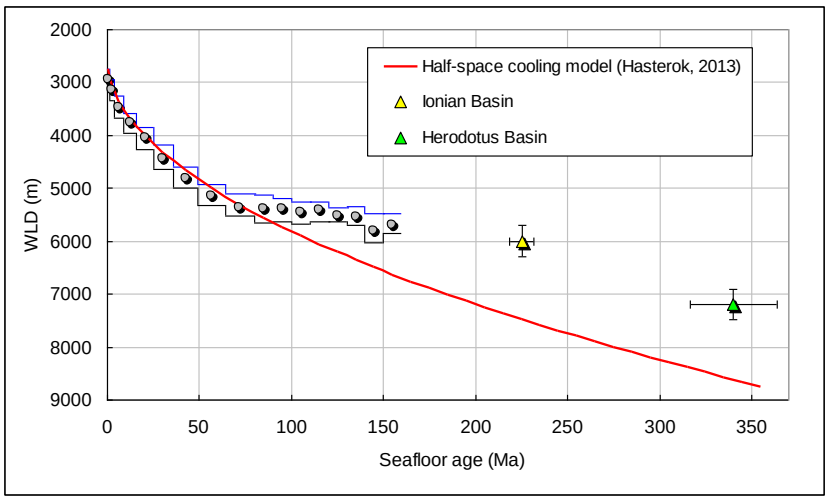

Fig. 66 Average WLD of the Ionian (yellow triangle) and Herodotus (green triangle) basins after sediment and crustal corrections versus seafloor age (see Table 20) and best-fitting half-space model (red curve) by Hasterok (2013). Thin blue and black lines are the upper and lower quartile values while grey full circles are WLD median values after Crosby and McKenzie (2009).

The age of the oceanic lithosphere by spreading anomalies within the Ionian and Herodotus basins was reported in two recent papers (see Speranza et al., 2012; Granot, 2016). Recently, Le Pichon et al. (2019) reviewed these results which are in part discordant and are not conclusive.

Speranza et al. (2012) interpreted the magnetic anomalies of the Ionian Sea based on a compilation of different sources. They proposed an age of 220–230 Ma with a northeast/southwest direction of spreading. However, their argument is indirect as it is based on the absence of a well-defined pattern of magnetic anomalies that led them to attribute this absence to a long interval of reversed magnetization occurring during the Middle Triassic.

In this regard, Le Pichon et al. (2019) determined the age of the lithosphere on basis of structural considerations, using the half-space model only for WLD and based on the geology of the margins. They concluded that the Ionian and Sirte basins are oceanic basins that completed their extensional phase during the Aptian, about 120 Ma.

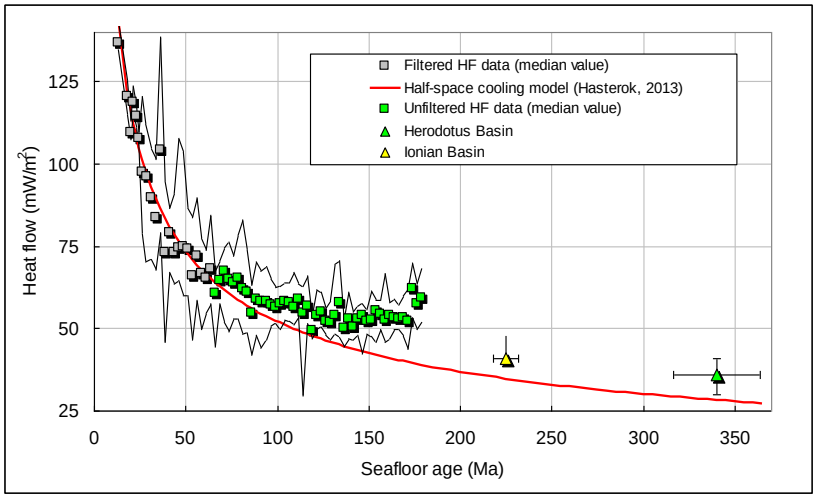

Fig. 67 Half-space model (red curve) and median heat flow dataset include globally unfiltered (circles), globally filtered (squares) data binned by seafloor age, used by Hasterok (2013). Black lines indicate interquartile ranges. Full triangles indicate median heat flow values in the oceanic area in the Ionian (yellow) and Herodotus (green) basins.

Figures 66 and 67 show that the half-space model in the Ionian basin gives puzzling results. A WLD of about 6000 m is reached at an age of about 115 Ma, whereas the surface heat flow of about 40 mW m^{-2} is compatible for an age of 160 Ma. According to Hasterok (2013), there are several reasons for the heat flow to be a better constraint on plate cooling models than bathymetry:

(1) Heat flow is not affected by flexure;

(2) Heat flow is relatively unaffected – at the very least to a lesser degree than bathymetry – by thermal rejuvenation at the base of the lithosphere due to the relatively localized heating in space and time and the long-time constant for diffusion (roughly equivalent to the seafloor age at the time of reheating);

(3) Lithosphere strength prevents full thermal contraction (Pollack, 1980; Korenaga, 2007). Bathymetry filters attempt to remove the former two complications, but results differ depending upon the choice of filter. The complications due to incomplete thermal contraction have a time dependence that violates the assumptions of simple cooling models (Korenaga, 2007).

8. CONCLUDING REMARKS

Bathymetric, sedimentological and geophysical data of the Eastern Mediterranean Sea (EMS) were collected and analysed in an integrated approach. The seafloor water-loaded depth (WLD) analysis and the terrestrial heat flow were used as main tools to characterise the nature and age of the Eastern Mediterranean Sea lithosphere. The estimated WLD and geothermal flow were compared to continental-stretching and oceanic cooling plate models. This approach also provided information about mantle dynamics.

To transform bathymetry into seafloor water-loaded depth, it was necessary to remove the sediment layer to eliminate the subsidence of the basement surface caused by the deposition of the sedimentary layer (sediment correction). Excluding the high value of WLD in the trench zones of the Hellenic Arc, the abyssal and bathyal plains of the Ionian and Herodotus basins generally show the highest WLD. The comparison between WLD and the seafloor depth predicted by lithosphere stretching and cooling models indicates that the Levantine Basin is likely to be a result of an old continental stretching event, whereas WLD in the Ionian and Herodotus basins is compatible with an old oceanic lithosphere.

The uncertainty on WLD calculations depends on the errors associated with bathymetric data and the thickness of the sediment cover. Regarding the bathymetry, a comparison between the dataset used in this study and other openly available seafloor files, shows that the average differences in bathymetry are ~ 50 m and thus of minor importance. The sediment correction is instead more relevant. However, it is likely that the uncertainty on the sediment correction, C_s, is ~ 200-250 m. Thus, errors on estimated WLD do not appear critical.

Even if the uncertainty on the sediment correction is accounted for, my WLD estimates in the Ionian and Herodotus basins exceed those predicted by the plate model of cooling of oceanic lithosphere, thus suggesting a residual topography anomaly. These results are in good agreement with those obtained by Winterbourne et al. (2014). These variations are closely matched by long-wavelength gravity anomalies suggesting that the Eastern Mediterranean Sea is far from being isostatically compensated and that the region contains some of the largest long-wavelength gravity anomalies on Earth.

The heat flow values are poorly variable throughout the entire Eastern Mediterranean Sea. Average values of 39, 35 and 40 mW m^{-2} characterize the Levantine, the Herodotus and the Ionian basins, respectively. These values are substantially lower than the average global heat flow of the oceans. Significant deviations of individual heat flow values from the regional mean are believed to be due to localized

environmental disturbances rather than to thermal disturbances in the crust or upper mantle, and therefore do not reflect the regional thermal state.

The reference plate cooling model by Hasterok (2013) that I used shows a significant improvement in misfit to observed heat flow and WLD particularly on older seafloor, compared to the well-known plate models GDH1 (Stein and Stein, 1992) and PS77 (Parsons and Sclater, 1977). This best-fitting plate model yields substantially a different prediction of the estimated plate thickness (90 km), particularly thinner than that estimated by PS77 (125 km). The average heat flow of the Ionian and Herodotus basins is smaller by 12-17 mW m^{-2} than the reference value predicted by the model. The low heat flow in the Ionian and the Herodotus basins might indicate that the lithosphere is much colder than the oldest oceanic plates. Such a thermal pattern has similarities to the Gulf of Mexico, in which anomalously low heat flow values were observed as well. Consequently, the combination of the large negative residual bathymetry and low heat flow suggests that the lithosphere under the Ionian and Herodotus basins may be anomalously cold.

Several local studies of seismic wave propagation showed an extensive region of thick lithosphere (more than 100 km) beneath the Eastern Mediterranean Sea. Therefore, possible hypotheses for the anomalous WLD and terrestrial heat flow might imply either these regions have escaped reheating by small-scale convection or that this convective mechanism does not hold for all ocean lithospheres. A lithosphere-asthenosphere boundary as deep as 115-150 km is consistent with a steady-state conductive lithosphere geotherm, constrained with the terrestrial heat flow in the Ionian Basin. Thus, the low terrestrial heat flow is compatible with an old, thick oceanic lithosphere that has reached thermal equilibrium.

One explanation for the lack of small-scale convection might simply lay in the fact that the Eastern Mediterranean Sea is narrow and surrounded by continental lithosphere on both sides. In this context, the small-scale boundary layer convection that maintains the temperature at the base of the oceanic lithosphere may not be initiated and the semi-infinite half-space cooling law might be applied. However, the half-space model shows ambiguous results. In both the Herodotus and Ionian basins, the observed WLD is smaller by about 1.5 km than the subsidence predicted by the half-space (positive residual bathymetry). This does not appear consistent with free air gravity data indicating a regional negative anomaly. The observed heat flow is instead closer to the half-space for it is larger by only 6-8 mW m^{-2}, whereas it differs by 12-17 mW m^{-2} with the plate cooling model.

In summary, despite the available data and pieces of evidence for the EMS are few and scattered, the comparison of the estimated WLD with the seafloor depth predicted by a uniform stretching model argues for a continental lithosphere in the Levantine Basin. Since stretching likely occurred about 90 Ma ago, this basin could have reached thermal equilibrium, and thus the surface heat flow does not show any enhancement caused by extension.

The large WLD and low heat flow in the Herodotus and Ionian basins argue for an oceanic lithosphere. However, both the adopted reference models for the oceanic heat flow and seafloor depth (the plate model and the half-space cooling) are not satisfactory in accounting for WLD and heat flow in the Ionian and Herodotus basins. The residual bathymetry estimated with the plate model is consistent with free-air gravity data, whereas the heat flow data seem in better agreement with the half-space model. In any case, the negative residual bathymetry inferred from the plate model and the negative, long-wavelength gravity anomaly corroborates (i) the presence of a colder and thick lithosphere in the Ionian and Herodotus basins and the lack of small-scale boundary layer convection that are invoked for maintaining a constant temperature at the base of the oceanic lithosphere, and (ii) the consequent downwelling of mantle material as a result of a negatively buoyant lithosphere. Both dynamic processes are consistent with the anomalously low heat flow observed in the whole EMS.

References

Agard, P., L. Jolivet, B. Vrielynck, E. Burov, Monié, P., 2007. Plate acceleration: The obduction trigger. Earth Planet. Sci. Lett., 258, 428–441, doi:10.1016/j.epsl.2007.04.002.

Agard, P., Omrani, J., Jolivet, L., Whitechurch, H., Vrielynck, B., Spakman, W., 2011. Zagros orogeny: A subduction-dominated process. Geological Magazine, 148(5-6), 692–725. https://doi.org/10.1017/S001675681100046X

Airy, G.B., 1855. On the computations of the effect of the attraction of the mountain masses as disturbing the apparent astronomical latitude of stations in geodetic surveys, Phil. Trans. R. Soc. London, 145, 101-104.

Aksu, A. E., Hall, J. and Yaltirak, C., 2005. 'Miocene to Recent tectonic evolution of the eastern Mediterranean: New pieces of the old Mediterranean puzzle,' Marine Geology, 221(1–4), pp. 1–13. doi: 10.1016/j.margeo.2005.03.014.

Aksu, A. Caber, M. and Albayrak, T., 2009. Measurement of the Destination Evaluation Supporting Factors and their Effects on Behavioral Intention of Visitors: Antalya Region of Turkey. Tourism Analysis. 14. 115-125. 10.3727/108354209788970199.

Aksu, A.E., Hall, J., Calon, T., Barnes, M.C., Güneş, P, Cranshaw, J.C., 2017. Messinian evaporites across the Anaximander Mountains, Sırrı Erinç Plateau and the Rhodes and Finike basins, eastern Mediterranean Sea. Marine Geology. 395, 48-64. doi: 10.1016/j.margeo.2017.09.013.

Amante, C., Eakins, B.W., 2009. ETOPO1 1 Arc-Minute Global Relief Model: Procedures, Data Sources and Analysis. NOAA Technical Memorandum NESDIS NGDC-24, 19 pp.

Andrieux J., Fontbote J.-M. and Mattauer M., 1971. -Sur un modele explicatif de l'Arc de Gibraltar. -Earth and Planetary Science Letters,12, 191–198.

Arsenikos, S., Frizon De Lamotte, D., Chamot-Rooke, N., Mohn, G., Bonneau, M. C. and Blanpied, C., 2013. 'Mechanism and timing of tectonic inversion in Cyrenaica (Libya): Integration in the geodynamics of the East Mediterranean,' Tectonophysics. Elsevier B.V., 608(December), pp. 319–329. doi: 10.1016/j.tecto.2013.09.025.

Auzende, J. M., Bonnin, J., and Olivet, J. L., 1973. The origin of the western Mediterranean basin: Jour. Geol. Soc. London, v. 129, p. 607–620.

Bar, O., 2009. The shaping of the continental margin of central Israel since the Late Eocene – tectonics, morphology and stratigraphy, Ph.D. thesis, Ben-Gurion Univ., Be'er-Sheva, Israel.

Bar, O., Gvirtzman, Z., Feinstein, S., Zilberman, E., 2013. Accelerated subsidence and sedimentation in the Levant Basin during the late tertiary and concurrent uplift of the Arabian platform: tectonic versus counteracting sedimentary loading effects. Tectonics 32:334–350. http://dx.doi.org/10.1002/tect.20026

Barrier, E., and Vrielynck, B., 2008. MEBE Atlas of the Paleotectonic maps of the Middle East. Commission for the Geological Map of the World, Paris, France.

Basilone, L., Gasparo Morticelli, M. and Lena, G., 2010. Mesozoic tectonics and volcanism of Tethyan rifted continental margins in western Sicily. Sedimentary Geology. 226. 54-70. 10.1016/j.sedgeo.2010.02.009.

Bein, A. and Gvirtzman, G., 1977. A Mesozoic fossil edge of the Arabian Plate along the Levant coastline and its bearing on the evolution of the Eastern Mediterranean. In: Biju-Duval, B. & Montadert, L. (eds) International Symposium on the Structural History of the Mediterranean Basin, Split (Yugoslavia). Technip, Paris, 95–110.

Ben Avraham, Z., Ginzburg, A., Makris, J., Eppelbaum, L., 2002. Crustal structure of the Levant Basin, Eastern Mediterranean. Tectonophysics, 346 (1–2), 23–43. doi: 10.1016/S0040-1951(01)00226-8.

Beydoun, Z. R., 1981. Some open questions relating to the petroleum prospects of Lebanon. Journal of Petroleum Geology, 3, 303–314. doi: 10.1111/j.1747-5457.1981.tb00932.x.

Beydoun, Z. R., 1991. Middle East hydrocarbon reserves enhancement, 1975-1990; significant developments and implications for potential future large increases. Journal of Petroleum Geology, 14(1), ii-iv. doi:http://dx.doi.org/10.1306/BF9AB6DC-0EB6-11D7-8643000102C1865D.

Biju-Duval, B., Letouzey, J., and Montadert, L., 1978. Structure and evolution of the Mediterranean Basins. In Initial Reports of the Deep Sea Drilling Project, (Vol. 42), 951–984. Washington, D.C.: U.S. Government Printing Office. https://doi.org/10.2973/dsdp.proc.42-1.150.1978

Bohnhoff, M., Makris, J., ,Papanikolaou, D. and Stavrakakis, G., 2001. Crustal investigation of the Hellenic subduction zone using wide aperture seismic data. Tectonophysics. 343. 239-262. 10.1016/S0040-1951(01)00264-5.

Bohnhoff M.,Harjes H.-P.,Meier T., 2005.Deformation and stress regimes in the Hellenic subduction zone from focal Mechanisms, J. Seismol.,9,341–366.

Bouillin, J. P.,1986. Le "bassin maghrebin"; une ancienne limite entre l'Europe et l'Afrique a l'ouest des Alpes. Bulletin de la Société géologique de France, 2(4), 547–558.

Brew, G., Barazangi, M., Al-Maleh, A.K., Sawaf, T., 2001. Tectonic and geologic evolution of Syria. GeoArabia 6, 573–615.

Bruinsma, S., Förste, C., Abrykosov, O., Lemoine, J.-M., Marty, J.-C., Mulet, S., Rio, M.-H., Bonvalot, S., 2014. ESA's satellite-only gravity field model via the direct approach based on all GOCE data. - Geophysical Research Letters, 41, 21, p. 7508-7514

Calcagnile, G., and Panza, G.F., 1981. The main characteristics of the lithosphere-asthenosphere system in Italy and surrounding regions, Pure Appl. Geophys. 119, 865-879.

Camerlenghi, A., Cita, M.B., Della Vedova, B., Fusi, N., Mirabile, L., and Pellis, G., 1995. Geophysical evidence of mud diapirism on the Mediterranean Ridge accretionary complex: Marine Geophysical Researches, v. 17, p. 115–141, doi: 10.1007/BF01203423.

Capponi, M., Glavich, E. and Sampietro, D., 2020. Map of Plio-Quaternary Sediment Depths in the Mediterranean Sea. Bollettino di Geofisica Teorica e Applicata, 61(4), 421-432.

Carlson, R., Herrick, C.N., 1990. Densities and porosities in the oceanic crust and their variations with depth and age. Journal of Geophysical Research Atmospheres, 95(B6), 9153-9170. doi: 10.1029/JB095iB06p09153

Catalano, R., Di Stefano, P., and Kozur, H., 1991. Permian circumpacific deep-water faunas from the western Tethys (Sicily, Italy)—New evidence for the position of the Permian Tethys. Palaeogeography, Palaeoclimatology, Palaeoecology, 87(1–4), 75–108. https://doi.org/10.1016/0031-0182(91)90131-A

Catalano, R., Doglioni, C., and Merlini, S., 2001. On the Mesozoic Ionian Basin. Geophysical Journal International, 144, 49–64. https://doi.org/10.1046/j.0956-540X.2000.01287.x

Cernobori, L., Nicolich, R., Petronio, L., and Romanelli, M., 1996. Crustal image of the Ionian basin and its Calabrian margins. Tectonophysics, 264, 175–189. https://doi.org/10.1016/S0040-1951(96)00125-4

Chamot-Rooke, N., Rangin, C., Le Pichon, X., DOTMED Working Group, 2005. Asynthesis of deep marine data in the Eastern Mediterranean. Soc. Géol. Fr. Mém. 177 (n.s., 64 p).

Chiozzi, P., Barkaoui, A., Rimi, A.. Verdoya, M., Zarhloule, Y., 2017. A review of surface heat-flow data of the northern Middle Atlas (Morocco). Journal of Geodynamics. 112. 10.1016/j.jog.2017.10.003.

Chiozzi, P., Verdoya M., El Jbeily E., 2021. Thermal structure of the Palaezoic oceanic lithosphere in the Herodotus Basin, Eastern Mediterranean Sea. Joint Scientific Assembly IAGA-IASPEI 21-27 August 2021

Christensen, U., 1982. Phase boundaries in finite amplitude mantle convection. Geophysical Journal of the Royal Astronomical Society. Volume 68, Issue 2. doi: 10.1111/j.1365-246X.1982.tb04911.x

Christensen, N. I., and Mooney, W. D., 1995. Seismic velocity structure and composition of the continental crust: A global view, J. Geophys. Res., 100(B6), 9761–9788, doi:10.1029/95JB00259.

Christova, C. and Nikolova, S., 1993. The Aegean region: deep structures and seismological properties. Geophys. J. Int. 115.

Cita, M.B., and Camerlenghi A., 1992. The Mediterranean Ridge as an accretionary prism in collisional setting. Memorie della Societa' Geologica Italiana, 45:463-480.

Cita, M.B., Ivanov, M.K. and Woodside, J.M., 1995. The Mediterranean Ridge diapiric belt. Marine Geology, 1-4: 1-6.

Clube, T. M. and Robertson, A. H. F., 1986. 'Troodos Palaeorotation Microplate,' Geophysics, 8, pp. 375–437.

Crosby, A.G., McKenzie, D., Sclater, J.G., 2006. The relationship between depth, age and gravity in the oceans. Geophys J Int 166, 553-573. doi: 10.1111/j.1365-246X.2006.03015.x.

Crosby, A.G., McKenzie, D., 2009. An analysis of young ocean depth, gravity and global residual topography. Geophys J Int 178, 1198-1219. doi: 10.1111/j.1365-246X.2009.04224.x.

Dannowski, Anke Kopp, Heidrun Klingelhoefer, Frauke Klaeschen, Dirk Gutscher, M.-A Krabbenhoeft, Anne Dellong, David Rovere, Marzia Graindorge, David Papenberg, Cord and Klaucke, Ingo., 2019. Ionian Abyssal Plain: A window into the Tethys oceanic lithosphere. Solid Earth. 10. 447-462. 10.5194/se-10-447-2019.

Davies, J. H. and Davies, D. R., 2010. Earth's surface heat flux. Solid Earth, 1, 5-24, https://doi.org/10.5194/se-1-5-2010, 2010.

Della Vedova, B., Pellis, G., and Pinna, E., 1989. Studio geofisico dell'area di transizione tra il Mar Pelagico e la Piana Abissale dello Jonio. Atti dell'8° Convegno del Gruppo Nazionale di Geofisica della Terra Solida, Roma, 1, 543–558.

Della Vedova, B., Pellis, G., Lawver, Lawrence A; Brancolini, G., 1992. Component parts of the World Heat Flow Data Collection. PANGAEA, https://doi.org/10.1594/PANGAEA.804230

Dellong, D., Klingelhoefer, F., Kopp, H., Graindorge, D., Margheriti, L., Moretti, M., 2018. Crustal structure of the Ionian Basin and Eastern Sicily Margin: Results from a wide-angle seismic survey. Journal of Geophysical Research: Solid Earth, 123(3), 2090–2114. https:// doi.org/10.1002/2017JB015312

Dercourt, J., Zonenshain, L.P., Ricou, L.E., Kazmin, V.G., Le Pichon, X., Knipper, A.L., Grandjacquet, C., Sbortshikov, I.M., Geyssant, J., Lepvrier, C., Pechersky, D., Boulin, J., Sibuet, J.C., Savostin, L.A., Sorokhtin, O., Westphal, M., Bazhenov, M., Lauer, J.P., Biju-Duval, B., 1986. Geological evolution of the Tethys belt from the Atlantic to the Pamirs since the LIAS. Tectonophysics. 123. 241-315. 10.1016/0040-1951(86)90199-X.

Dercourt J.,Ricou L. E.&Vrielynck B.(eds),1993.Atlas. Tethys Paleoenvironmental Maps. Gauthier-Villars, Paris.

Dercourt, J., Gaetani, M., Vrielynck, B., Barrier, E., Biju Duval, B., Brunet, M.F., Cadet, J.P., Crasquin, S., Sandulescu (eds), 2000. Atlas Peri-Tethys, Palaeogeographical maps, 24 maps and explanatory notes: IXX. CCGM/CGMW, Paris, 269 pp.

de Voogd, B., Truffert, C., Chamot-Rooke, N., Huchon, P., Lallemant, S., Le Pichon, X., 1992. Two-ship seismic soundings in the basins of the Eastern Mediterranean Sea (Pasiphae cruise). Geophys. J. Int. 109, 536-552. doi: 10.1111/j.1365-246X.1992.tb00116.x.

Dewey, J. F., Pitman, W., Ryan, W. B. F. and Bonnin, J., 1973. 'Plate Tectonics and the Evolution of the Alpine System Plate Tectonics and the Evolution of the Alpine System', Geological Society of America Bulletin, 84(October), pp. 3137–3180. doi: 10.1130/0016-7606(1973)84<3137.

Dubertret, L., 1955. Carte géologique du Liban au 1/200000 avec notice explicative. Ministère des Travaux Publiques, Beirut, République Libanaise, 74 pp.

El Jbeily E.,Verdoya M.,Chiozzi P.,Ivaldi R., and Ghaith A., 2019. "Geothermal flow and water-load seafloor depth of the Eastern Mediterranean Sea", AIP Conference Proceedings 2123, 020018 https://doi.org/10.1063/1.5116945

El-Sharkawy, A.,Meier, T.,Lebedev, S.,Behrmann, J. H.,Hamada, M.,Cristiano, L., 2020.The slab puzzle of the Alpine-Mediterranean region: Insights from a new, high-resolution, shear wave velocity model of the upper mantle.Geochemistry, Geophysics, Geosystems,21, e2020GC008993.https://doi.org/10.1029/2020GC008993

Emeis, K. C., Robertson, A. H. F. and Richter, C., 1996a. 'HOLE 966A', Proceedings of the Ocean Drilling Program - Scientific Results, 160(March 1995), pp. 155–213.

Emeis, K. C., Robertson, A. H. F. and Richter, C., 1996b. 'Site 965', Proceedings of the Ocean Drilling Program, Initial Reports, 160(4), pp. 125–153.

Emeis, K. C., Robertson, A. H. F. and Richter, C., 1996c. 'Site 967', Proceedings of the Ocean Drilling Program, Initial Reports, 160(April 1995), pp. 215–287.

Emeis, K. C., Robertson, A. H. F. and Richter, C., 1996d. 'Site 968', Proceedings of the Ocean Drilling Program, Initial Reports, 160, pp. 289–333.

Erickson, A. J., 1970. The Measurements and Interpretation of Heat flow in the Mediterranean and Black Sea, Ph.D. Thesis (M.I.T., Cambridge, Massachusetts,).

Erickson, A. J., Simmons, G., Ryan, William B. F., 1977. Component parts of the World Heat Flow Data Collection. PANGAEA, https://doi.org/10.1594/PANGAEA.806987

Erickson, A.J., Von Herzen, R.P., 1978. Down-hole Temperature Measurements, Deep Sea Drilling Project. Leg 42A. In Initial Reports of the Deep Sea Drilling Project, 42, Part I (eds. HSU, K.J., MONTADERT, L. et al.) (Washington U.S. Government Printing Office) pp. 857–871.

Faccenna, C., Funiciello, F., Giardini, D., Lucente, P., 2001a. Episodic back-arc extension during restricted mantle convection in the Central Mediterranean. Earth Planet. Sci. Lett. 187, 105–116.

Favre, P., Stampfli, G.M., 1992. From rifting to passive margin: the examples of the Red Sea, Central Atlantic and Alpine Tethys. Tectonophysics 215:69–97. http://doi.org/10.1016/0040-1951(92)90075-H.

Feld, C., Mechie, J., Hübscher, C., Hall, J., Stelios, N., Gurbuz, C., Bauer, K., Louden, K., Weber, M., 2017. Crustal structure of the Eratosthenes Seamount, Cyprus and S. Turkey from an amphibian wide-angle seismic profile. Tectonophysics, 700-701, 32-59.

Finetti, I., F. Giorgetti, H. Haessler, H. T. P. Hoang, D. Slejko, and Wittlinger G., 1976. Time-space epicenter and hypocenter distribution and focal mechanism of 1976 Friuli earthquakes, Boll. Geofis. Teor. Appl., 19, 637-655, 1976.

Finetti, I,. 1982. Structure, Stratigraphy and evolution of central Mediterranean. Bollettino di Geofisica Teorica ed Applicata, 24(96), 247–312. https://doi.org/10.1007/s10539-010-9244-0

Freund, R., Z., G. and Zak, I., 1970. 'The shear along the Dead Sea rift,' Philosophical Transactions of the Royal Society London, 107(267), pp. 107–130.

Freund, R., Goldberg M., Weissbrod T., Druckman Y., and Derin B., 1975. The Triassic-Jurassic structure of Israel and its relation to the origin of the eastern Mediterranean, Isr. Geol. Surv. Bull., 65, 26.

Frizon de Lamotte, D., Raulin, C., Mouchot, N., Wrobel-Daveau J.C., Blanpied C., Ringenbach, J.C., 2011. The southernmost margin of the Tethys realm during the Mesozoic and Cenozoic: Initial geometry and timing of the inversion processes. Tectonics, 30, TC3002, doi:10.1029/2010TC002691, 2011.

Fuchs, C., Kuhn, J., Bobrowski, N., and Platt, U., 2021. Quantitative imaging of volcanic SO2 plumes using Fabry–Pérot interferometer correlation spectroscopy, Atmos. Meas. Tech., 14, 295–307, https://doi.org/10.5194/amt-14-295-2021

Gallais, F., Gutscher, M. A., Graindorge, D., Chamot-Rooke, N. and Klaeschen, D., 2011. 'A Miocene tectonic inversion in the Ionian Sea (central Mediterranean): Evidence from multichannel seismic data', Journal of Geophysical Research: Solid Earth, 116(12), pp. 1–16. doi: 10.1029/2011JB008505.

Gallais, F., Gutscher, M. A., Klaeschen, D., and Graindorge, D., 2012. Two-stage growth of the Calabrian accretionary wedge in the Ionian Sea (Central Mediterranean): Constraints from depth-migrated multichannel seismic data. Marine Geology, 326-328, 28–45. https://doi.org/10.1016/j.margeo.2012.08.006

Gardosh, M., Druckman, Y., Buchbinder, B., Calvo, R., 2008. The Oligo-Miocene deepwater system of the Levant Basin. Geological Survey of Israel Rep., GSI/33/2008 (73 p).

Gardosh, M. A., Garfunkel, Z., Druckman, Y. and Buchbinder, E., 2010. Evolution of the Levant Margin and Western Arabia Platform since the Mesozoic (eds C. Homberg and M. Bachmann). Geol. Soc. Spec. Publ., 341, 9–36.

Garfunkel, Z., 1998. Constraints on the origin and history of the Eastern Mediterranean Basin; collision-related processes in the Mediterranean region. Tectonophysics 298, 5–35.

Garfunkel, Z., 2004. Origin of the Eastern Mediterranean basin: A reevaluation. Tectonophysics, 391(1-4 SPEC.ISS.), pp. 11–34.

George, R., Rogers, N., Kelley, S., 1998. Earliest magmatism in Ethiopia: evidence for two mantle plumes in one flood basalts province. Geology 26, 923–926.

Giermann, G., 1969. 'The Eastern Mediterranean Ridge'', Rapp. Commn. int. Explor. Scient. Mer Méditerranée 19, 605–607.

Godfrey, N. J., B. C. Beaudoin, S. L. Klemperer, and the Mendocino Working Group USA, 1997. Ophiolitic basement to the Great Valley forearc basin, California, from seismic and gravity data: Implications for crustal growth at the North American continental margin, Geol. Soc. Am. Bull. 109, 1536-1562.

Guiraud, R., Bosworth, W., 1997. Senonian basin inversion and rejuvenation of rifting in Africa and Arabia; synthesis and implications to plate-scale tectonics. Tectonophysics 282 (1–4), 39–82.

Gvirtzman, Z., Zilberman E., and Folkman Y., 2008. Reactivation of the Levant passive margin during the late Tertiary and formation of the Jaffa Basin offshore central Israel, J. Geol. Soc. Lon., 165, 563–578, doi:10.1144/0016-76492006-200.

Hall, J.K., Calon, T.J., Aksu A.E., Meade, S.R., 2005. Structural evolution of the Latakia Ridge and Cyprus Basin at the front of the Cyprus Arc, Eastern Mediterranean Sea. Mar Geol, 221, 261–297. doi: 10.1016/j.margeo.2008.02.007

Hamilton, E., 1959. Thickness and consolidation of deep-sea sediments. *GSA Bulletin* 1959;; 70 (11): 1399–1424. doi: https://doi.org/10.1130/0016-7606(1959)70[1399:TACODS]2.0.CO;2

Hamilton, E., 1976, Variations of density and porosity with depth in deep-sea sediments, J. Sed. Petrol. 46, 280–300.

Hamilton, E., 1978 "Sound velocity–density relations in sea-floor sediments and rocks", The Journal of the Acoustical Society of America 63, 366-377 https://doi.org/10.1121/1.381747

Hasterok, D. Chapman, D. and Davis, E.E., 2011. Oceanic heat flow: Implications for global heat loss. Earth and Planetary Science Letters - EARTH PLANET SCI LETT. 311, 386-395. doi: 10.1016/j.epsl.2011.09.044.

Hasterok, D., 2013. A heat flow based cooling model for tectonic plates. Earth and Planetary Science Letters. 361, 34–43. doi: 10.1016/j.epsl.2012.10.036.

Haq, B. U., 2014. 'Cretaceous eustasy revisited,' Global and Planetary Change. Elsevier B.V., 113, pp. 44–58. doi: 10.1016/j.gloplacha.2013.12.007.

Hawie, N., Deschamps, R., Nader, F.H., Gorini, C., Müller, C., Desmares, D., Hoteit, A., Granjeon, D., Montadert, L., Baudin, F., 2013. Sedimentological and stratigraphic evolution of northern Lebanon since the late Cretaceous: implications for the Levant margin and basin. Arab. J. Geosci. http://dx.doi.org/10.1007/s12517-013-0914-5.

Heine, C., Müller, D., 2008. The IntraCONtinental basins (ICONS) atlas – Applications in eastern Australia. 275-290.

Hemming, S., 2007. Paleoceanography, physical and chemical proxies Terrigenous Sediments. 10.1016/B0-44-452747-8/00303-3.

Hempton, M., 1987. Constraints on Arabian plate motion and extensional history of the Red Sea. Tectonics, 6, 687- 705.

Henriquet, M.,Dominguez, S.,Barreca, G.,Malavieille, J.,Cadio, C., &Monaco, C.,2019.Deep origin of the dome-shaped Hyblean Plateau, southeastern Sicily: A new tectono-magmatic model.Tectonics,38,4488–4515.https://doi.org/10.1029/2019TC005548

Hensen, F.R.S., 1951. Observations on the geology of the petroleum occurrences of the Middle East. In: 3rd World Petroleum Congress, 118–140.

Hieke, W., Hirschleber, H. B., and Dehghani, G. A., 1998. The crust of the Ionian Abyssal Plain—Old oceanic ? Rapports de la Commission Internationale pour l'exploration scientifique de la mer Méditerranée, 35, 72–73.

Hieke, W., Cita M. B.,, Forcella F., and Müller C., 2006. Geology of the Victor Hensen Seahill (Ionian Sea, eastern Mediterranean): Insights from the study of cored sediment sequences, Boll. Soc. Geol. Ital., 125, 245–257.

Hieke, W., Camerlenghi, A., Cita, M.B., Dehghani, G.,A., Fusi, N., Hirschleber, H.B., Mirabile, L., Müller, C., Polonia, A., 2009. Bannock Basin, Sirte Abyssal Plain and Conrad Spur: structural relationships between Mediterranean Ridge and its western foreland and implications on the character of the accretionary complex (eastern Mediterranean). *Mar. Geophys. Res*., 30,161–192.

Hirschleber, H.B., Hartmann, J.M., and Hieke, W., 1994. The Mediterranean Ridge accretionary complex and its forelands – seismic reflection studies in the Ionian Sea. Cruise Report of the Meteor, 491-509.

Hoggard, M.J., Winterbourne, J., Czarnota, K., White, N., 2017. Oceanic residual depth measurements, the plate cooling model, and global dynamic topography. Journal of Geophysical Research: Solid Earth/Volume 122, Issue 3. 2328- 2373. doi: 10.1002/2016JB013457

Howell, A., Jackson, J., Copley, A., McKenzie, D., Nissen, E., 2017. Subduction and vertical coastal motions in the eastern Mediterranean, *Geophysical Journal International*, Volume 211, Issue 1, October 2017, Pages 593–620, https://doi.org/10.1093/gji/ggx307

Hsü, K. J., W. B. F. Ryan, and M. B. Cita, 1973, Late Miocene desiccation of the Mediterranean, Nature, 242, 240–244.

Hsü, K., and Montadert, L., 1978, Initial Reports of the Deep Sea Drilling Project, v. 42, Part I, 951-984, Washington D.C., U.S. Government Printing Office.

Hughen, K., Southon, A., John R., Lehmann, S., Bertrand, J., Chanda, J H., Turnbull, J., 2006.: Age determination of ODP Site 165-1002. PANGAEA, https://doi.org/10.1594/PANGAEA.742881, Supplement to:

Inati, L. Lithosphere dynamics and architecture of the Levant basin margins : integrated geophysical approach. Geophysics [physics.geo-ph]. Université Pierre et Marie Curie - Paris VI; Université Saint-Joseph (Beyrouth). Ecole supérieure d'ingénieurs de Beyrouth, 2017. English. ffNNT : 2017PA066314ff. fftel-01719268f

Inati, L., Zeyen, H., Nader, F.H., Adelinet, M., Sursock, A., Rahhal. M.E., Roure, F., 2016. Lithospheric architecture of the Levant Basin (Eastern Mediterranean region): A 2D modeling approach. Tectonophysics, 693, 143-156.

Işler, F.I. Aksu, A.E. Hall, Jeremy Calon, T and Yasar, D., 2005. Neogene development of the Antalya Basin, Eastern Mediterranean: An active forearc basin adjacent to an arc junction. Marine Geology. 221. 299-330. 10.1016/j.margeo.2005.03.006.

Jaupart, C. and Mareschal, J.-C., 2007. Heat flow and thermal structure of the lithosphere, in: Treatise on Geophysics, Vol. 6, edited by: Schubert, G., 217–252, Oxford, Elsevier Ltd.

Jemsek, J. P., 1988. Heat Flow and Tectonics of the Ligurian Sea Basin and Margin.

Jolivet, L., Faccenna, C., Agard, P., Frizon de Lamotte, D., Menant, A., Sternai, P. and Guillocheau, F., 2015. 'Neo-Tethys geodynamics and mantle convection: from extension to compression in Africa and a conceptual model for obduction,' Canadian Journal of Earth Sciences. pp. 1-41. doi: 10.1139/cjes-2015-0118.

Jonathan, T., Turcotte, D. L. and Schubert, G., 2002.*Geodynamics*, 2nd ed.: xv + 456 pp. Cambridge, New York, Melbourne: Cambridge University Press. ISBN 0521 66186 2; 0 521 66624 4 (pb). *Geol. Mag.*139, 2002,.*Geological Magazine* 2002; 139 (6): 719. doi:https://doi.org/10.1017/S0016756802217239

Jones, E.J.W., 1999, Marine Geophysics. New York: John Wiley.

Kastens, K.A., Mascle, J., Auroux, C. et al., 1987, Proceedings of the Ocean Drilling Program, Part A – Initial Reports Tyrrhenian Sea, Ocean Drilling Program Texas A&M University 107, 1–1013.

Kastens, K.A., Breen, N. and Cita, M.B., 1992. Progressive deformation of an evaporite-bearing accretionary complex: SeaMARC I, Seabeam, and piston-core observations from the Mediterranean Ridge. Mar. Geophys. Res., 14, 249–298.

Kempler, D., and Garfunkel, Z., 1994. Structures and kinematics in the northeastern Mediterranean: A study of an irregular plate boundary. Tectonophysics, 234, 19–32.

Kempler, D. Mart, Y.,i Herut, B., and McCoy, F., 1996. Diapiric features in the southeastern Mediterranean Sea: possible indication of extension in a zone of incipient continental collision. Marine Geology - MAR GEOLOGY. 134. 237-248. 10.1016/0025-3227(96)00032-1.

Kempler, D., 1998. 'Eratosthenes Seamount: The Possible Spearhead of Incipient Continental Collision in the Eastern Mediterranean.' Proceedings of the Ocean Drilling Program, Scientific Results, 160, pp.709–721

Korenaga, J., 2007. Thermal cracking and the deep hydration of oceanic lithosphere: A key to the generation of plate tectonics?J. Geophys. Res.,112, B05408, doi:10.1029/2006JB004502.

Krasheninnikov, V.A., Udintsev, G.B., Mouraviov, V., and Hall, J.K., 1994. Geological structure of the Eratosthenes Seamount. In Krasheninnikov, V.A., and Hall, J.K. (Eds.), Geological Structure of the Northeastern Mediterranean (Cruise 5 of the Research Vessel Akademik Nokolaj Stra-khov): Jerusalem (Historical Productions-Hall Ltd.), 113−130

Laske, Gabi Masters, Guy Ma, Zhitu Pasyanos, Mike., 2013. Update on CRUST1.0 - A 1-degree global model of Earth's crust. Abstract EGU2013-2658 presented at 2013 Geophys. Res. Abstracts 15. 15. 2658-.

Le Meur, D., 1997. Etude géophysique de la structure profonde et de la tectonique active de la partie occidentale de Ride Méditerranéenne, 225pp., PhD thesis, Univ. Paris XI, Paris.

Le Nindre, Y.M., Vaslet, D., Manivit, J., 1990. Histoire géologique de la bordure occidentale de la plate-forme arabe; volume 3. Documents - B.R.G.M., 193, 290 pp.

Le Pichon, X. and Angelier, J., 1979. 'The Hellenic arc and trench system: A key to the neotectonic evolution of the eastern Mediterranean area,' Tectonophysics, 60(1–2), pp. 1–42. doi: 10.1016/0040-1951(79)90131-8.

Le Pichon, X., Sibuet, J.C., 1981. Passive margins: a model of formation. J. Geophys. Res. 86, 3708–3720.

Le Pichon, X., 1982. Land-locked oceanic basins and continental collision: the eastern Mediterranean as a case example. In: Mountain Building Processes, ed. K Hsü, London Academic, 1, 29–46.

Le Pichon, X., Chamot-Rooke, N., Lallemant, S., Noomen, R., and Veis, G., 1995, Geodetic determination of the kinematics of central Greece with respect to Europe: Implications for eastern Mediterranean tectonics: Journal of Geophysical Research, v. 100, p. 12,675–12,690, doi: 10.1029/95JB00317.

Le Pichon, X. and Kreemer, C., 2010. 'The Miocene-to-Present Kinematic Evolution of the Eastern Mediterranean and Middle East and Its Implications for Dynamics,' Annual Review of Earth and Planetary Sciences, 38(1), pp. 323–351. doi: 10.1146/annurev-earth-040809-152419.

Le Pichon, X., Mehmet Celal Sengor, A., and Imren C., 2019. A new approach the opening of the Eastern Mediterranean Sea and the origin of the Hellenic Subduction Zone Part 1: The Eastern Mediterranean Sea. Canadian Journal of Earth Sciences, 56(8), DOI: 10.1139/cjes-2018-0128

Ludwig, J. W., Nafe, J. E. and Drake, C. L., 1970. Seismic refraction, in The Sea, vol. 4, 53-84, ed. Maxwell, A. E., Wiley, New York.

Makris, J., Z. Ben Abraham., A. Behle., A. Ginzburg, P. Giese, L. Steinmetz, R. B. Whitmarsh, Eleftheriou, S., 1983. Seismic refraction profiles between Cyprus and Israel and their interpretation:

Makris, J., Nicolich, R., & Weigel, W., 1986. A seismic study in the Western Ionian Sea. Annales Geophysicae, 4(6), 665–678.

Makris, J., & Yegorova, T., 2006. A 3-D density–velocity model between the Cretan Sea and Libya. Tectonophysics. 417. 201-220. 10.1016/j.tecto.2005.11.003.

Mascle, J.,1999. Images may show start of European-African Plate collision,Eos Trans. AGU, 80(37), 421, 425, 428.

Mazzullo, J. and Graham, A. G., 1988. "Handbook for Shipboard Sedimentologists."

McCallum, J. E., Scrutton, R. A., Robertson, A. H. F. and Ferrari, W., 1993. 'Seismostratigraphy and Neogene-Recent depositional history of the south-central continental margin of Cyprus,' Marine and Petroleum Geology, 10(5), pp. 426–438. doi: 10.1016/0264-8172(93)90045-T.

McClusky, S., Balassanian, S., Barka, A., Demir, C., Ergintav, S., Georgiev, I., Gurkan, O., Hamburger, M., Hurst, K., Kahle, H., Kastens, K., Kekelidze, G., King, R., Kotzev, V., Lenk, O., Mahmoud, S., Mishin, A., Nadariya, M., Ouzounis, A., Paradissis, D., Peter, Y., Prilepin, M., Reilinger, R., Sanli, I., Seeger, H., Tealeb, A., ToksöZ, M. N., Veis, G., 2000. Global positioning system constraints on plate kinematics and dynamics in the eastern Mediterranean and Caucasus. Journal of Geophysical Research 105 (B3), 5695–5720, doi:10.1029/1999JB900351.

McKenzie, D. P., 1967. Some remarks on heat flow and gravity anomalies, J. Geophys. Res., 72(24), 6261–6273, doi:10.1029/JZ072i024p06261.

McKenzie, D.P., 1970. Plate tectonics of the Mediterranean region. Nature, 226(5242): 239-243.

McKenzie, D., 1978. Some remarks on the development of the sedimentary basins. Earth Planet. Sci. Lett. 40: 25-32. http://dx.doi.org/10.1016/0012-821X(78)90071-7.

McKenzie, D., 1984. The generation and compaction of partially molten rock, Journal of Petrology, 1984, vol. 25 (pg. 713 - 765).

Mckenzie, D., Bickle, M.J., 1988. The volume and composition of melt generated by extension of the lithosphere. J. Petrol. 29, 625–679. http://dx.doi.org/10.1093/ petrology/29.3.625.

McKenzie, D., 2020. The structure of the lithosphere and upper mantle beneath the Eastern Mediterranean and Middle East. Med. Geosc. Rev. 2, 311–326 . https://doi.org/10.1007/s42990-020-00038-1

Minelli, L., & Faccenna, C., 2010. Evolution of the Calabrian accretionary wedge (central Mediterranean). Tectonics, 29, TC4004. https://doi.org/10.1029/2009TC002562

Montadert, L., Nicolaides, S., Semb, P.H., Lie, O., 2014. Petroleum systems offshore Cyprus. In: Marlow, L., Kendall, C., Yose, L. (Eds.), Petroleum Systems of the Tethyan Region. AAPG Memoir Vol. 106, pp. 301–334.

Mueller, S. & Kahle, H.., 1993. Crust-mantle evolution, structure and dynamics of the Mediterranean-Alpine region. 10.1029/GD023p0249.

Nader, F.H., 2011. The petroleum prospectivity of Lebanon: an overview. J. Pet. Geol. 34 (2), 135–156.

Nader, F.H., 2014. The Geology of Lebanon. Scientific Press, 108 pp. ISBN 978-0-9575310-3-1.

Nafe, J. E;. & Drake, C. L., 1957. Variation with depth in shallow and deep water marine sediments of porosity, density and the velocities of compressional and shear waves, Geophysics, 22, 523-552.

Nafe, J. E. and Drake, C. L., 1963. "Physical Properties of Marine Sediments," In: M. N. Hill, Ed., The Sea, pp. 794-813.

Netzeband, G. L., K. Gohl, C. P. Hübscher, Z. Ben-Avraham, G. A. Dehghani, D. Gajewski, Liersch, P., 2006. The Levantine Basin - crustal structure and origin: Tectonophysics, 418, 167-188.

Nur, A., Ben-Avraham, Z., 1978. The eastern Mediterranean and the Levant: tectonics of continental collision. Tectonophysics 46, 297–312.

Papadimitriou N., Gorini C., Nader F.H., Deschamps R., Symeou V., Lecomte J.C., 2018. Tectono-stratigraphic evolution of the western margin of the Levant Basin (offshore Cyprus), Marine and Petroleum Geology, Volume 91, 2018, Pages 683-705, ISSN 0264-8172.

Papadimitriou N., 2017. Geodynamics and synchronous filling of a rift type-basin evolved through compression tectonics (The western margin of the Levant Basin). Earth Sciences. Université Pierre et Marie Curie - Paris VI, 2017. English.

Papazachos, B. & Papaioannou, C., 1999. Lithospheric boundaries and plate motions in the Cyprus area. Tectonophysics. 308. 193-204. 10.1016/S0040-1951(99)00075-X.

Parsons, B., Sclater, J.G., 1977. An analysis of the variation of ocean floor bathymetry and heat flow with age. J Geophys Res, 82, 803-827.

Pasquale, V., Verdoya, M., Chiozzi, P., 1994. Types of crust beneath the Ligurian Sea. Terra Nova, 6, 255–266.

Pasquale V., Verdoya M., Chiozzi P., 2005. Thermal Structure of the Ionian Slab Pure appl. geophys. 162 967–986

Pasquale, V., Chiozzi, P. & Verdoya, M., 2006. Sedimentation rates and subsidence in the Southern Tyrrhenian Basin, Marine geophys. Res., 27, 155–165.

Pasquale V., Chiozzi P., Verdoya M., 2007. Isostasy and paleotemperatures in the Southern Tyrrhenian Basin, Mediterranean Sea Mar Geophys Res (2007) 28:139–151.

Pasquale V., Chiozzi P., Verdoya M., 2012. Geothermics Heat Flow in the Lithosphere. Springer Briefs in Earth Sciences. doi 10.1007/978-3-319-02511-7

Pollack, H.N., 1980. The heat flow from the earth: a review. In Mechanisms of Continental Drift and Plate Tectonics, ed. P. A. Davies, S. K. Runcorn, pp. 183-92. London: Academic. 367 pp.

Pollack, H. N.,Hurter, S. J., andJohnson, J. R., 1993.Heat flow from the Earth's interior: Analysis of the global data set,*Rev. Geophys.*,31(3), 267–280. doi:10.1029/93RG01249

Polonia, A., Torelli, L., Mussoni, P., Gasperini, L., Artoni, A., & Klaeschen, D., 2011. The Calabrian Arc subduction complex in the Ionian Sea: Regional architecture, active deformation, and seismic hazard. Tectonics, 30, TC5018. https://doi.org/10.1029/2010TC002821

Pribnow, D.F.C., Kinoshita, M., Stein, C.A., 2000. Thermal Data Collection and Heat Flow Recalculations for ODP Legs 101-180, Institute for Joint Geoscientific Research, GGA, Hannover, Germany, 0120432.

Priestley, K., and McKenzie D., 2006., The thermal structure of the lithosphere from shear wave velocities, Earth Planet. Sci. Lett., 244, 285– 301.

Priestley, K., Ho, T., and Mitra, S., 2019. The Crustal Structure of the Himalaya: A Synthesis.*Geol. Soc. Spec. Publ.* 483, 483–516. doi:10.1144/sp483-2018-127

Rangin, Claude; Silver, Eli A; Harding, Barry W; Storms, Michael A; Shipboard Scientific Party, 2005. Close-up images of ODP Hole 124-769A. PANGAEA, https://doi.org/10.1594/PANGAEA.796490

Raulin, C., Frizon de Lamotte, D., Bouaziz, S., Khomsi, S., Mouchot, N., Ruiz, G., & Guillocheau, F., 2011. Late Triassic–early Jurassic block tilting along E–W faults, in southern Tunisia: New interpretation of the Tebaga of Medenine. Journal of African Earth Sciences, 61(1), 94–104. https://doi.org/10.1016/j.jafrearsci.2011.05.007

Reilinger, R., McClusky, S., Vernant, P., Lawrence, S., Ergintav, S., Cakmak, R., Ozener, H., Kadirov, F., Guliev, I., Stepanyan, R., Nadariya, M., Hahubia, G., Mahmoud, S., Sakr, K., ArRajehi, A., Paradissis, D., Al- Aydrus, A., Prilepin, M., Guseva, T., Evren, E., Dmitrotsa, A., Filikov, S. V., Gomez, F., Al-Ghazzi, R. and Karam, G., 2006. GPS constraints on continental deformation in the Africa-Arabia-Eurasia continental collision zone and implications for the dynamics of plate interactions. Journal of Geophysical Research: Solid Earth, 111(5), pp. 1–26. doi: 10.1029/2005JB004051.

Ricou, L.E., 1994. Tethys reconstructed: plates continental fragments and their boundaries since 260 Ma from Central America to South-Eastern Asia. Geodin. Acta 7, 169–218.

Ritsema, A.R.., 1970. On the origin of the western Mediterranean Sea basins. Tectonophysics. 10. 609-623. 10.1016/0040-1951(70)90049-1.

Ritsema, J., Deuss, A., van Heijst, H. J., Woodhouse, J. H., 2011. S40RTS: a degree-40 shear-velocity model for the mantle from new Rayleigh wave dispersion, teleseismic traveltime and normal-mode splitting function measurements, *Geophysical Journal International*, Volume 184, Issue 3, March 2011, Pages 1223–1236, https://doi.org/10.1111/j.1365-246X.2010.04884.x

Roberts, G., Peace, D., 2007. Hydrocarbon plays and prospectivity of the Levantine Basin, offshore Lebanon and Syria from modern seismic data. GeoArabia 12 (3), 99–124.

Robertson, A. H. F., Dixon, J.E., 1984. Aspects of the geological evolution of the Eastern Mediterranean. In J. E. Dixon and A. H. F. Robertson, eds. The geologic evolution of the Eastern Mediterranean. The Geol. Soc. London, Special Publication, v. 17, 1–74.

Robertson, A. H. F., 1994. 'Probing continental collision in the Mediterranean Sea,' Eos, Transactions American Geophysical Union, 75(21), pp. 233–239. doi: 10.1029/94EO00909.

Roberstson, A.H.F., 1998. Tectonic significance of the Eratosthenes Seamount: a continental fragment in the process of collision with subduction zone in the eastern Mediterranean (Ocean Drilling Program Leg 160). Tectonophysics, 298, 63–82.

Robertson, A. H. F., 2007. 'Overview of tectonic settings related to the rifting and opening of Mesozoic ocean basins in the Eastern Tethys: Oman, Himalayas and Eastern Mediterranean regions,' Geological Society, London, Special Publications, 282(1), pp. 325–388. doi: 10.1144/SP282.15.

Robertson, A. H. F., Parlak, O., Rizaoglu, T., Unlugenc, U., Inan, N., Tasli, K. and Ustaomer, T., 2007. 'Tectonic evolution of the South Tethyan ocean: evidence from the Eastern Taurus Mountains (Elazig region, SE Turkey)', Geological Society, London, Special Publications, 272(1), pp. 231–270. doi: 10.1144/GSL.SP.2007.272.01.14.

Robertson, A. H. F, Karamata, S. and Saric, K., 2009. 'Overview of ophiolites and related units in the Late Palaeozoic-Early Cenozoic magmatic and tectonic development of Tethys in the northern part of the Balkan region,' Lithos, 108(1–4), pp. 1–36. doi: 10.1016/j.lithos.2008.09.007.

Robertson, A. H. F., Parlak, O. and Ustaomer, T., 2012. 'Overview of the Palaeozoic-Neogene evolution of Neotethys in the Eastern Mediterranean region (southern Turkey, Cyprus, Syria),' Petroleum Geoscience, 18(4), pp. 381–404. doi: 10.1144/petgeo2011-091.

Rosenbaum, G., Lister, G. S., & Duboz, C., 2004. The Mesozoic and Cenozoic motion of Adria (central Mediterranean): A review of constraints and limitations. Geodinamica Acta, 17(2), 125–139. https://doi.org/10.3166/ga.17.125-139

Roure, F., Casero, P., & Addoum, B., 2012. Alpine inversion of the North African margin and delamination of its continental lithosphere. Tectonics, 31, TC30006. https://doi.org/10.1029/2011TC002989

Roure, F. M., Casero, P. and Addoum, B., 2013. 'Mesozoic and Cenozoic Basins Formation and Deformation Along the North African Margin,' 30276.

Royden,L., 1986. A Simple Method for Analyzing Subsidence and Heat Flow in Extensional Basins, in Burrus, J. (ed.), *Thermal Modeling in Sedimentary Basins*, Editions Technip, Paris, p. 49-73.

Rybakov, M., Segev, A., 2004. Top of the crystalline basement in the Levant. Geochem. Geophys. Geosyst. 5 (9). http://dx.doi.org/10.1029/2004GC000690

Sage, L., Letouzey, J., 1990. Convergence of the African and Eurasian Plate in the Eastern Mediterranean. Petroleum and Tectonics in Mobile Belts, Paris, pp. 49–68.

Sagy, Y., 2016. Tectono-Sedimentary Processes in the deep Levant Basin.

Sawyer, D., 1985. Total tectonic subsidence: A parameter for distinguishing crust type at the U. S. Atlantic Continental Margin. Journal of Geophysical Research. 90. 7751-7770. doi: 10.1029/JB090iB09p07751.

Schaeffer, A. J., Lebedev, S., 2013. Global shear speed structure of the upper mantle and transition zone, *Geophysical Journal International*, Volume 194, Issue 1, July 2013, Pages 417–449, https://doi.org/10.1093/gji/ggt095

Schattner, U. and Ben-Avraham, Z., 2007. 'Transform margin of the northern Levant, eastern Mediterranean: From formation to reactivation,' Tectonics, 26(5), pp. 1–17. doi: 10.1029/2007TC002112.

Schattner, U., 2010. What triggered the early-to-mid Pleistocene tectonic transition across the entire eastern Mediterranean?, Earth Planet. Sci. Lett., 2010,vol.289 3–4 (pg. 539 – 548)

Schieber J., 1978. Black shales. In: Sedimentology. Encyclopedia of Earth Science. Springer, Berlin, Heidelberg . https://doi.org/10.1007/3-540-31079-7_30

Schütz, F., Förster, H.J., Förster, A., 2014. Thermal conditions of the central Sinai Microplate inferred from new surface heat-flow values and continuous borehole temperature logging in central and southern Israel Journal of Geodynamics 76 8–24

Sclater, J. G., and Christie, P. A. F.,1980. Continental stretching: An explanation of the Post-Mid-Cretaceous subsidence of the central North Sea Basin, J. Geophys. Res., 85(B7), 3711– 3739, doi:10.1029/JB085iB07p03711.

Segev, A., Rybakov, M., 2010. Effects of Cretaceous plume and convergence, and Early Tertiary tectonomagmatic quiescence on the central and southern Levant continental margin. Journal of the Geological Society, 167, 731-749, doi:10.1144/0016-76492009-118.

Segev, A., Sass, E., & Schattner, U., 2018. Age and structure of the Levant Basin, Eastern Mediterranean. Earth-Science Reviews, 182, 233–250. https://doi.org/10.1016/j.earscirev.2018.05.011

Seton, M., Müller, R. D., Zahirovic, S., Williams, S., Wright, N. M., Cannon, J., 2020. A global data set of present-day oceanic crustal age and seafloor spreading parameters. Geochemistry, Geophysics, Geosystems, 21, e2020GC009214. https://doi.org/10.1029/2020GC009214

Shalev, E., Lyakhovsky V., Weinstein Y., Ben-Avraham Z., 2013. The thermal structure of Israel and the Dead Sea Fault, Tectonophysics, Volume 602, 2013, Pages 69-77, ISSN 0040-1951,https://doi.org/10.1016/j.tecto.2012.09.011
(https://www.sciencedirect.com/science/article/pii/S0040195112005690)

Smith, W.H.F., Sandwell, D.T, 1997. Global seafloor topography from satellite altimetry and ship depth soundings. Science, 277, 1956-1962

Speranza, F.,Minelli, L.,Pignatelli, A., and Chiappini, M.,2012., The Ionian Sea: The oldest in situ ocean fragment of the world?, J. Geophys. Res., 117, B12101, doi:10.1029/2012JB009475.

Spudich, P., and Orcutt, J., 1980. Petrology and porosity of an oceanic crustal site: Results from waveform modeling of seismic refraction data, J. Geophys. Res., 85(B3), 1409– 1433, doi:10.1029/JB085iB03p01409.

Stampfli, G., Marcoux, J. Baud, A., 1991.Tethyan margins in space and time. Palaeogeogr. Palaeoclimatol. Palaeoecol. 87, 373_409

Stampfli, G. M., Mosar, J., Favre, P., Pillevuit, A., & Vannay, J., 2001. Permo-mesozoic evolution of the western Tethys realm; the Teo-Tethys east Mediterranean Basin connection. Mémoires du Museum National d'Histoire Naturelle, 186, 51-108.

Stampfli, G. M., and Borel, G. D., 2002. 'A plate tectonic model for the Paleozoic and Mesozoic constrained by dynamic plate boundaries and restored synthetic oceanic isochrons,' Earth and Planetary Science Letters, 196(1–2), pp. 17–33. doi: 10.1016/S0012-821X(01)00588-X.

Stanton, S., 2017. Structural History of the North African Margin: Insights into the Prediction of Offshore Plays.

Steckler, M.S. and Watts, A.B., 1978, Subsidence of the Atlantic-type continental margin off New York, Earth Planet. Sci. Lett. 41, 1–13

Steckler, U., Brink, S., 1986. Lithospheric strength variations as a control on new plate boundaries: examples from the northern Red Sea region. Earth Planet. Sci. Lett. 79, 120–132.

Stein, C.A. Stein, S., 1992. A model for the global variation in oceanic depth and heat flow with lithospheric age. Nature, 359, 123-129. doi:10.1038/359123a0

Steinberg, J., Gvirtzman, Z., Folkman, Y., Garfunkel, Z., 2011. Origin and nature of the rapid late tertiary filling of the Levant Basin. Geology 39 (4):355–358. http://dx.doi.org/10. 1130/G31615.1

Tassy, A., Crouzy, E., Gorini, C., Rubino, J. L., Bouroullec, J. L. and Sapin, F., 2015a. 'Egyptian Tethyan margin in the Mesozoic: Evolution of a mixed carbonate-siliciclastic shelf edge (from Western Desert to Sinai)', Marine and Petroleum Geology, 68, pp. 565–581. doi: 10.1016/j.marpetgeo.2015.10.011.

Terzaghi, K., and Peck R. B., 1948. Soil Mechanics in Engineering Practice, 566 pp., John Wiley, New York,.

Tezcan, A. K., Turgay, M. I., 1991. Component parts of the World Heat Flow Data Collection. PANGAEA, https://doi.org/10.1594/PANGAEA.807627

Tugend, J., Chamot-Rooke, N., Arsenikos, S., Blanpied, C., & Frizon de Lamotte, D., 2019. Geology of the Ionian Basin and margins: A key to the East Mediterranean geodynamics. Tectonics, 38. https://doi.org/10.1029/ 2018TC005472

Verdoya, M., Chiozzi, P., 2018. Heat-flow anomaly and residual topography in the Mascarene hotspot swell (Indian Ocean). Int J Earth Sci (Geol Rundsch), 107, 35-51. doi: 107. 10.1007/s00531-017-1459-8.

Verdoya, M., Chiozzi, P., Gola, G., 2021. Unravelling the terrestrial heat flow of a young orogen: The example of the northern Apennines. Geothermics, 101993.

Von Herzen, R., Uyeda, S., 1963. Heat flow through the eastern Pacific Ocean floor. J Geophys Res 68:4219–4250

Von Huene, R., Corvala´n, J., Flueh, E. R., Hinz, K., Korstgard, J., Ranero, C. R., and Weinrebe, W., Tectonic control of the subducting Juan Fernandez Ridge on the Andean margin near Valparaiso, Chile, Tectonics, 16, 474 – 488, 1997.

Walley, C. D., 2001. The Lebanon passive margin and the evolution of the Levantine Neotethys. In P. A. Ziegler, W. Cavazza, A. H. F. Robertson, and S. Crasquin-Soleau, eds., Peri-Tethys Memoir 6: Peri- Tethyan Rift / Wrench Basins and Passive Margins. Mémoires du Muséum National d'Histoire Naturelle, Paris,86, 407-439.

Watanabe, T., Langseth, M. G. and Anderson, R. N., 1977. Heat flow in back-arc basins of the western Pacific, in Island Arcs Deep Sea Trenches, and back-Arc Basins, edited by M. Talwani and W. Pitman III, pp. 137– 162, AGU, Washington, D.C.

Welford, K. & Hall, J., & Rahimi, A., & Reiche, S., & Huebscher, C., & Louden, K., 2015. Crustal structure from the Hecataeus Rise to the Levantine Basin, eastern Mediterranean, from seismic refraction and gravity modelling. Geophysical Journal International. 203. 2055-2069. 10.1093/gji/ggv422.

White, R. S., McKenzie, D., and O'Nions, R. K., 1992, Oceanic crustal thickness from seismic measurements and rare earth element inversions: Journal of Geophysical Research, v. 97, p. 19683–19715

Wildi, W., 1983. La chaîne tello-rifaine (Algérie, Maroc, Tunisie): Structure, stratigraphie et évolution du Trias au Miocène. Revue de Géographie Physique et de Géologie Dynamique, 24(3), 201–297.

Winterbourne, J. R., Crosby, A. G., and White N. J., 2009., Depth, age and dynamic topography of oceanic lithosphere beneath heavily sedimented Atlantic margins, Earth Planet. Sci. Lett., 287, 137–151.

Winterbourne, J., White, N., Crosby, A., 2014, Accurate measurements of residual topography from the oceanic realm, Tectonics,33, 982–1015, doi:10.1002/2013TC003372.

Wyllie, R. J., Gregory, M & R., Gardner, A & W., L., 1956. Elastic Wave Velocities in Heterogeneous and Porous Media. Geophysics. 21. 41-70. 10.1190/1.1438217.

Zeyen, H., Volker, F., Wehrle, V., Fuchs, K., Sobolev, S.V., Altherr, R., 1997. Styles of continental rifting: crust-mantle detachment and mantle plumes. Tectonophysics 278, 329–352

Zitter, T. A. C., Woodside, J. M. and Mascle, J., 2000. 'Neotectonic accommodation between Hellenic and Cyprus Arcs,' (October), pp. 1–4.